A chemical approach to
Heusler compounds and nanoparticles

Dissertation

Zur Erlangung des Grades

"Doktor der Naturwissenschaften"

im Promotionsfach Chemie

am Fachbereich Chemie, Pharmazie und Geowissenschaften

der Johannes Gutenberg-Universität Mainz

vorgelegt von

Changhai Wang

geboren in Shenyang (China)

Mainz, 2011

List of publications

Journals

2009

[1] Lubna Basit, **Changhai Wang**, Catherine A. Jenkins, Benjamin Balke, Vadim Ksenofontov, Gerhard H. Fecher, Claudia Felser, Enrico Mugnaioli, Ute Kolb, Sergej A. Nepijko, Gerd Schönhense, and Michael Klimenkov, *J. Phys. D: Appl. Phys.* **42**, 084018 (2009).

[2] C. J. Liu, **C. H. Wang**, C. L. Wang, Y. Hwu, C. Y. Lin, and G. Margaritondo, *J. Synchrotron Radiation* **16**, 395 (2009).

[3] **Chang-Hai Wang**, Chi-Jen Liu, Cheng-Liang Wang, Chia-Chi Chien, Yeu-Kuang Hwu, Ru-Shi Liu, Chung-Shi Yang, Jung-Ho Je, Hong-Ming Lin, and Giorgio Margaritondo, *Appl. Phys. A.* **97**, 295 (2009).

2010

[4] C. -C. Chien, **C. -H. Wang**, C. -L. Wang, E. -R. Li, K. H. Lee, Y. Hwu, C. -Y. Lin, S. -J. Chang, C. -S. Yang, C. Petibois, and G. Margaritondo, *Anal. Bioanal. Chem.* **397**, 2109 (2010).

[5] Chi-Jen Liu, **Chang-Hai Wang**, Shin-Tai Chen, Hsiang-Hsin Chen, Wei-Hua Leng, Chia-Chi Chien, Cheng-Liang Wang, Ivan M. Kempson, Yeu-Kuang Hwu, Tsung-Ching Lai, Michael Hsiao, Chung-Shi Yang, Yu-Jen Chen and Giorgio Margaritondo, *Phys. Med. Biol.* **55**, 931 (2010).

[6] **C. H. Wang**, Y. Z. Guo, F. Casper, B. Balke, G. H. Fecher, C. Felser, and Y. Hwu, *Appl. Phys. Lett.* **97**, 103106 (2010).

[7] **Changhai Wang**, Lubna Basit, Yuriy Khalavka, Yanzhi Guo, Frederick Casper, Teuta Gasi, Vadim Ksenofontov, Benjamin Balke, Gerhard H. Fecher, Carsten Sönnichsen, Yeu-Kuang Hwu, Jey-Jau Lee, and Claudia Felser, *Chem. Mater.* **22**, 6575 (2010).

2011

[8] **Chang-Hai Wang,** Chi-Jen Liu, Chia-Chi Chien, Hsin-Tai Chen, Tzu-En Hua, Wei-Hua Leng, Hsiang-Hsin Chen, Ivan M. Kempson, Yeu-Kuang Hwu, Michael Hsiao, Tsung-Ching Lai, Ji-Ling Wang, Chung-Shi Yang, Hong-Ming Lin, Yu-Jen Chen, and Giorgio Margaritondo, *Mater. Chem. Phys.* **126**, 352 (2011).

[9] **Changhai Wang**, Yuriy Khalavka, Frederick Casper, Teuta Gasi, Vadim Ksenofontov, Benjamin Balke, Gerhard H. Fecher, Claudia Felser, Carsten Sönnichsen, Yeu-Kuang Hwu, and Jey-Jau Lee, "**Effects of composition and silica supports on the structure and particle size of Co_2FeGa Heusler nanoparticles,**" submitted to *J. Mater. Chem.* (2011).

[10] **Changhai Wang**, Frederick Casper, Teuta Gasi, Vadim Ksenofontov, Benjamin Balke, Gerhard H. Fecher, Claudia Felser, Yuriy Khalavka, Carsten Sönnichsen, Yeu-Kuang Hwu, and Jey-Jau Lee, "**Structural and magnetic properties of Fe$_2$CoGa Heusler nanoparticles with excess Fe**," submitted to *Appl. Phys. Lett.* (2011).

[11] **Changhai Wang**, Tanja Graf, Frederick Casper, Benjamin Balke, Gerhard H. Fecher, and Claudia Felser, "**Heusler nanocrystals for spintronics, magnetic shape memory alloys and thermoelectrics**," (critical review) submitted to *J. Vac. Sci. Technol. B.* (2011).

Conference Talks

[1] *Shining Chemistry: Gold nanoparticles under synchrotron X-rays*
Changhai Wang, Chi-Jen Liu, Tzu-En Hua, Chia-Chi Chien, Shin-Tai Chen, Wei-Hua Leng, and Yeu-Kuang Hwu.
DPG Spring meeting, 26 March 2009, Dresden, Germany.

[2] *Co$_2$FeGa nanoparticles at the interface of Physics, Chemistry, and Materials Science*
Changhai Wang, Frederick Casper, Benjamin Balke, Gerhard H. Fecher, and Claudia Felser.
DPG Spring meeting, 17 March 2011, Dresden, Germany.

Contents

1. Introduction

The Heusler compounds, discovered by German engineer Friz Heusler in 1903 [1], refer to ternary intermetallic compounds having the formula X_2YZ and a $L2_1$ crystal structure. Usually X and Y are transition metals and Z is a main group element. The ferromagnetism in Heusler compounds originates from the $L2_1$ crystal structure. Not all Heusler compounds are ferromagnetic and some are antiferromagnetic (e.g. Pd_2MnIn and Cu_2MnSb). Kübler et al. [2] first described the unusual density of states (DOS) of Co_2MnAl and Co_2MnSn and predicted spectacular electron transport behavior in these compounds. The concept of half metallic ferromagnets (HMF) was first proposed by de Groot [3] for the half-Heusler compound NiMnSb. The HMFs exhibit 100% spin polarization at the Fermi energy since there is a finite density of states at the Fermi level in one spin direction and a gap in the other spin direction. Most of Co_2YZ Heusler compounds with perfectly $L2_1$ ordered structures are predicted as HMFs showing a high spin polarization of the conduction electrons in tunneling magnetic junctions (TMJ). This exceptional property makes the HMFs ideal candidates for spin injection devices in spin electronics [4].

Heusler compounds are multifunctional magnetic materials and have been extensively studied due to their potential technical importance. The discovery of the giant magnetoresistance (GMR) effect [5,6] gives birth to a new research field, namely the spintronics. Spintronics works by manipulating the spin of electrons instead of the charge of electrons. The advantages of spintronic devices include nonvolatility, increased data processing speed, large storage density, and lower energy consumption. The half metallic ferromagnetism found in many Heusler compounds enables them promising materials for spintronic devices. A strong technological link between Heusler compounds and spintronics has been forged. Commercial products based on spintronics have been increasingly appeared such as magnetic hard disks, magnetic random access memories, and magnetic sensors. Besides the promising role played by Heusler compounds in spintronics, they also find wide application fields including magnetic shape memory alloys (MSMA) [7,8], thermoelectrics [9,10], solar cells [11], and the latest topological insulators [12–14].

Recently, significant efforts have been made in searching of new candidates for half-metallic ferromagnetism and spintronics. Several practical aspects, however, are to be thoroughly considered before the power of half-metallic ferromagnetism and spintronics can be fully exploited. Table 1.1 shows the experimentally derived tunneling magentoresistance (TMR) ratio and spin polarization (SP) of selected TMJ devices. Even though many compounds have been theoretically predicted 100% spin polarized at Fermi level, much decreased values were obtained. This phenomenon points to the effects of several important factors including structural disorder, phase purity, and surface effects. Theoretical and experimental investigations have revealed that a decrease in spin polarization is closely related to certain types of structural disorder [19–21]. According to Bunker [22], structural disorder of materials can be classified to three categories: (1) thermal disorder due to thermal disturbance; (2) static structural disorder within given sites, and (3) site disorder, i.e. swapping of atoms among different atom positions. The SP properties of Heusler compounds depend significantly upon the type and degree of site disorders.

Table 1.1 TMR ratios and SP of selected TMJ devices using HMF Heusler compounds as electrodes at low temperature and room temperature (in parentheses).

Work	TMJ structure	TMR ratio (%)	SP (%)
[15]	$Co_2MnSi–AlO_x–Co_2MnSi$	570 (67)	0.83 – 0.89
[16]	$Co_2MnSi–MgO–Co_{0.5}Fe_{0.5}$	192(90)	0.75
[17]	$Co_2FeAl_{0.5}Si_{0.5}–MgO–Co_2FeAl_{0.5}Si_{0.5}$	390(220)	0.81
[18]	$Co_2Mn_{1.29}Si–MgO–Co_2Mn_{1.29}Si$	1135 (236)	——
[18]	$Co_2Mn_{1.4}Ge_{0.38}–MgO–Co_2Mn_{1.4}Ge_{0.38}$	650 (220)	——

The Slater–Pauling rule [23,24] is a simple way to study the correlations of the valence electron concentration and magnetic moments for Heusler compounds. For Heusler compounds composed of different atoms, the generalized Slater–Pauling rule [25,26] applies: the magnetic moment per unit cell (M) is expressed as

$$M = N_V - 24 \tag{1}$$

Here N_V denotes the accumulated number of valence electrons in the unit cell containing four atoms. The number 24 arises from the number of completely occupied minority bands in full Heusler compounds. It should be noted that the measured magnetic moments need to be extrapolated to the value at 0 K to compare to the values estimated from the Slater–Pauling rule. The Co_2YZ Heusler compounds follow the Slater–Pauling rule and the total spin magnetic moment scales linearly with the number of valence electrons. The magnetic moments of Co_2YZ Heusler compounds increase with increasing number of valence electrons. For type I and II half-metals, the magnetic moment per unit cell becomes strictly integer.

Heusler compounds crystallize in the $L2_1$ structure (see Figure 1 as an example for Co_2FeGa). The related space group is $Fm\bar{3}m$ (Space group No. 225). Co occupies the Wyckoff site 8c (1/4, 1/4, 1/4), Fe is on 4a (0, 0, 0) and Ga on 4b (1/2, 1/2, 1/2). The unit cell contains eight cubes with one Co atom in each center while Fe and Ga atoms occupy the corners of the cubes. Therefore, each atom is face centered and the lattice constitutes four interpenetrating fcc sublattices.
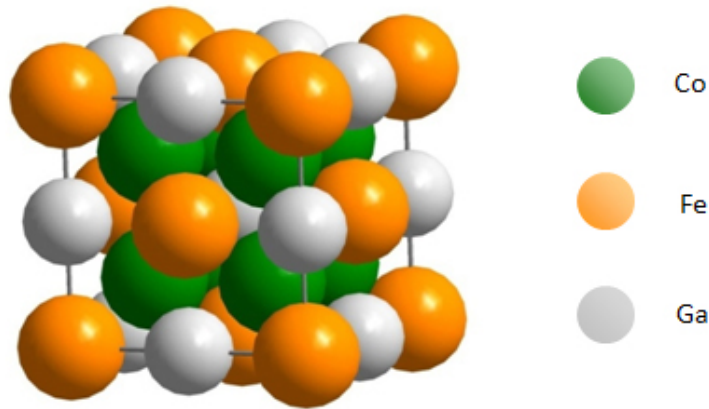
Figure 1.1 A crystallographic description of Co_2FeGa Heusler compounds with the $L2_1$ ordered structure.

Depending on the site exchangeability, various types of site disorder have been identified. Complete disorder in Co_2FeGa occurs when all sites are equivalent resulting in the $A2$-type disorder with space group of $Im\bar{3}m$ (Space group No. 229) and is also known as tungsten-type structure. If only the Fe and the Ga atoms are exchangeable, the 4a and 4b positions become equivalent. This leads to a $B2$-type disorder with the prototype compound of CsCl. The symmetry is changed and the resulting space group is $Pm\bar{3}m$ (Space group No. 221). The random distribution of Fe and Co atoms results in the BiF_3-type disorder (Space

group No. 225, $Fm\bar{3}m$, DO_3). For $B32a$ disorder (Space group No. 227, $Fd\bar{3}m$), attributed to NaTl-type structure, the Co atoms which occupy one fcc sublattice are mixed with the Fe atoms whereas the Co atoms on the other sublattice are mixed with the Ga atoms. The Co atoms are placed at the Wyckoff position 8a (0, 0, 0) and the Fe and Ga atoms are randomly distributed at position 8b (1/2, 1/2, 1/2). The X disorder (space group No. 216, $F\bar{4}3m$) with CuHg$_2$Ti as the prototype normally occurs in X$_2$YZ compounds if the atomic number of the Y element is larger than X atom. The X atoms do not build a simple cubic lattice but occupy the 4a (0, 0, 0) and 4c (1/4, 1/4, 1/4) Wyckoff positions. The Fe and Ga atoms are located at 4b (1/2, 1/2, 1/2) and 4d (3/4, 3/4, 3/4) positions, respectively. The crystal structure of Co$_2$FeGa compounds with different order types are summarized in Table 1.2.

Table 1.2 Crystal structure of Co$_2$FeGa compounds with different order types.

Order (SB)	Structure (ICSD)	Space group	Wyckoff position		
			Co	Fe	Ga
$A2$	W	$Im\bar{3}m$ (229)	2a	2a	2a
$B2$	CsCl	$Pm\bar{3}m$ (221)	1a	1a	1a
$L2_1$	Cu$_2$MnAl	$Fm\bar{3}m$ (225)	8c	4a	4b
DO_3	BiF$_3$	$Fm\bar{3}m$ (225)	8c/4b	8c	4a
$B32a$	NaTl	$Fd\bar{3}m$ (227)	8a	8b	8b
X	CuHg$_2$Ti	$F\bar{4}3m$ (216)	4a/4c	4b	4d

Under favorable conditions, the types of disorder can be differentiated by comparing the appearance and relative intensities of the (111) and (200) superlattice signatures. The (111) and (200) reflections signify the ordering at Y–Z and X–Y sites, respectively. Figure 1.2 shows the calculated powder diffraction patterns of Co$_2$FeGa compounds with a variety of order types. Table 1.3 describes the relative reflection intensities of the (111) and (200) reflections.

By this way, $A2$, $B2$, and $L2_1$ ordered structures can be distinguished. It should be noted that some types of disorder cannot be detected easily by conventional diffraction methods. For examples, the $L2_1$ and DO_3 structures of Co$_2$FeGa might be difficult to distinguish. Therefore, anomalous X-ray diffraction (AXRD) has been introduced to verify the $L2_1$ ordered structure of Heusler compounds [27]. In order to distinguish among different order types, a combination of diffraction and spectroscopic methods is preferable. In this light, extended X-ray absorption fine structure (EXAFS) spectroscopy has been utilized to provide complementary information on the long range order of bulk Heusler compounds. Ravel et al. [28] examined the antisite disorder in Co$_2$MnSi by EXAFS and compared its sensitivity to neutron diffraction. The capability of using EXAFS analysis to differentiate the crystal structure of Co-Fe based full Heusler alloys has been demonstrated by Balke et al. [29–31]. Other methods valuable to distinguish among different structure types include Mössbauer spectroscopy [32], nuclear magnetic resonance (NMR) [32], and neutron diffraction (ND) [27].
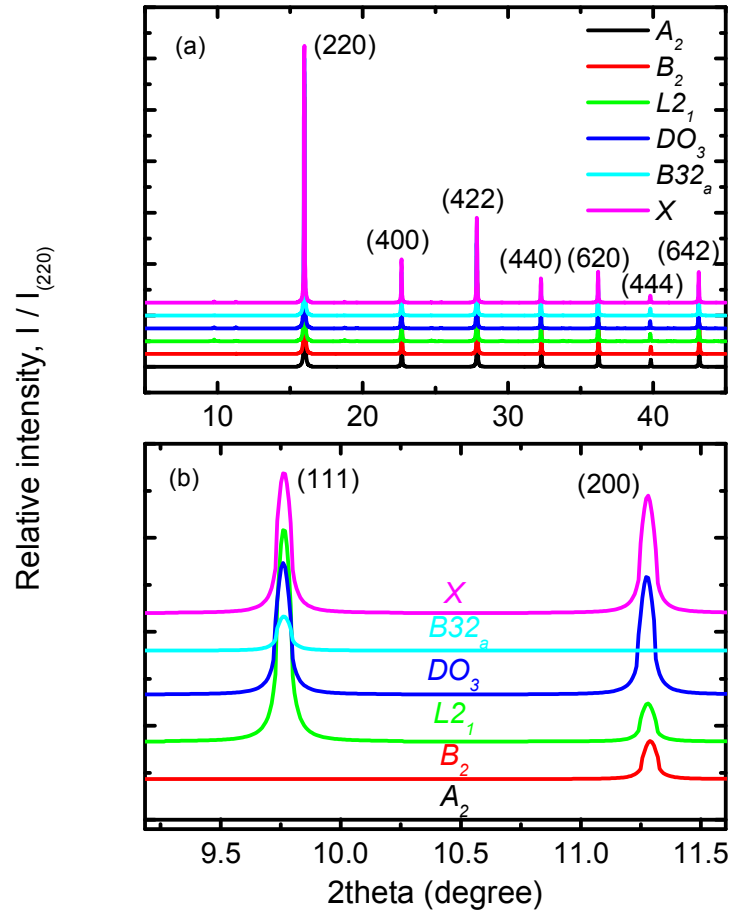
Figure 1.2 Calculated X-ray diffraction patterns of Co₂FeGa in different order types: (a) Full range spectra; (b) Zoom-in of the (111) and (200) reflections. X-ray photon energy: 22 keV.

Table 1.3 Relative intensities of the reflections for Co_2FeGa compounds of different order types. X-ray energy: 22 keV.

Structure (SB)	Relative intensity								
	(111)	(200)	(220)	(311)	(222)	(331)	(420)	(511)	(531)
$A2$	—	—	100	—	—	—	—	—	—
$B2$	—	0.12	100	—	0.05	—	0.09	—	—
$L2_1$	0.68	0.12	100	0.50	0.05	0.25	0.09	0.15	0.18
DO_3	0.42	0.37	100	0.32	0.15	0.16	0.24	0.10	0.12
$B32a$	0.11	—	100	0.09	—	0.05	—	0.03	0.04
X	0.45	0.37	100	0.34	0.15	0.17	0.24	0.10	0.13

The concept of "nano" is inherently embedded in spintronics because the GMR effect which has given birth to spintronics was firstly discovered in multilayer structures with thickness reduced to the nanoscale. "Nanotechnology was an original prerequisite for the discovery of GMR, now magnetoelectronics is in its turn a driving force for new applications of nanotechnology" [33]. Recently, Heusler compounds of reduced dimensionality and decreased length scales have been studied both theoretically [34,35] and experimentally [36, 37]. Investigations in Heusler nanoparticles have been propelled envisaging the importance of dimension and interfaces in affecting the structure and spin-related properties of spintronic devices. For example, Hirohata et al. [37] reported Si segregation and coexistence of amorphous phase in nano-grained Co_2MnSi thin films. In this work, Heusler nanoparticles refer to isolated or supported nanoparticles with a composition and structure of full Heusler compounds and with a particle size smaller than 100 nm.

For Heusler nanoparticles, an added degree of freedom is the particle size. From the viewpoint of applied physics, some questions are still open:

(1) How size affects the structure (long range and short range order) and magnetic properties of Heusler nanoparticles;

(2) What is the critical size of superparamagnetic Heusler nanoparticles;

(3) Whether the HMF behavior vanishes for Heusler nanoparticles;

Understanding the behavior of Heusler nanoparticles paves the way to technical innovations in spintronic devices to meet the increasing requirements of miniature, high performance and energy-saving.

The synthesis, structure, and properties of Heusler nanoparticles became a new research field with a multidisciplinary nature involving physics, chemistry and materials science [38–41]. Before this work, however, Heusler nanoparticles specially for spintronic applications has not been investigated. Among the numerous full Heusler compounds, Co based ones (Co_2YZ) constitute one of the most promising candidates for spintronic applications due to their high spin polarization, high magnetization, and high Curie temperature [42,43]. Most Co_2YZ are predicted to be HMFs and Co_2FeZ (Z = Al, Si) are presently used in spintronic devices [44–46]. The synthesis and characterization of Co_2YZ Heusler nanoparticles are the major objective of this work.

In terms of achieving stable HMF behavior, quaternary Heusler Heusler compounds such as $Co_2FeAl_{1-x}Si_x$ and $Co_2Mn_{1-x}Fe_xSi$ might be appealing since appropriate electron doping stabilizes the gap in the minority states and results in stable HMF characteristics [47, 48]. For chemists and materials scientists, however, a successful synthesis of impurity-free quaternary Heusler nanoparticles is extremely challenging. For a successful chemical synthesis of Heusler nanoparticles, important factors such as atomic radius, electronegativity, phase stability, and size control must be taken into accounts. In this work, a chemical approach is developed to prepare Co-Fe based ternary Heusler nanoparticles.

In addition, demanding structural characterizations are also required for Heusler nanoparticles to clarify the order type and degree of disorder. For Heusler nanoparticles, structural disorder and surface effects become more significant due to large surface-to-bulk ratio. Furthermore, there might be additional difficulties in the structural characterizations of Heusler nanoparticles by conventional X-ray diffraction. For example, the particle size-induced broadening or even disappearance of the characteristic (111) and (200) reflections renders difficulty in identifying the structure of Heusler nanoparticles. To unambiguously determine the order – disorder of Heusler nanoparticles is not a trivial task. Less information on the short range order of Heusler nanoparticles is available in the

literature. Furthermore, the dependences of the long and short range order and magnetic properties of Heusler nanoparticles on particle size are to be explored.

The thesis is organized as follows. *Chapter 1* summarizes the background and motivation of the current work. *Chapter 2* presents a concise description on the experimental details including sample preparation and characterization methods. *Chapter 3* deals with the chemical synthesis and characterizations of Co_2FeGa Heusler nanoparticles. Emphases are placed on the effects of precursor composition and template materials. Size correlated structure and magnetic properties of Co_2FeGa nanoparticles are described in *Chapter 4*. In *Chapter 5* a discussion of the long and short range order and magnetic properties of Fe-rich Fe_2CoGa nanoparticles is presented. The strategies to control particle size and synthetic transferability to other Co_2YZ nanoparticles are discussed in *Chapter 6*. Other chemical approaches for Heusler nanoparticles have also been attempted. Those data and related discussions are also presented in *Chapter 6*. In *Chapter 7*, the work on the chemical synthesis of metallic nanoparticles based on synchrotron X-ray irradiations are described. Successful examples include gold, silver, and binary alloys. Its feasibility to ternary Heusler compounds is also discussed. A summary of current work and perspectives for further studies are presented in *Chapter 8*.

2.   Experimental details

In this chapter, a short description on the synthesis and characterization of silica supported, carbon coated Co_2FeGa (Co_2FeGa-SiO_2@C) nanoparticles is presented. To test the synthetic transferability, similar approaches for Co_2FeGa nanoparticles are adapted for the preparation of other Co-based Heusler nanoparticles. For those cases, only the precursor salts are changed while the processing parameters are identical to those for Co_2FeGa nanoparticles. More detailed descriptions on the synthetic parameters can be found in the related chapters.

2.1   Chemicals and nanoparticle synthesis.

The precursors were $Fe(NO_3)_3.9H_2O$ (99.99%), $CoCl_26H_2O$ (>99%) and $Ga(NO_3)_3.xH_2O$ (99.9%, x = 8 according to the literature [49]). All chemicals were purchased from Sigma-Aldrich and used as received. The silica supports were commercially available fume silica (average particle size of 20 nm, surface area of 390 ± 40 m^2/g). In a typical preparation, 0.40 mmol $Fe(NO_3)_3.9H_2O$, 1.08 mmol $CoCl_2.6H_2O$, and 0.32 mmol $Ga(NO_3)_3.xH_2O$ were dispersed in 50 ml methanol and treated with a mild sonication for 5 min. 1g fume silica was added to the precursor solution and the suspension was sonicated for another 1 h. Methanol was removed using a rotary evaporator. The obtained solid was then dried at 80 °C for 2 h to achieve complete dryness. The solid was gently ground to powder and typically 200 mg was used for annealing (850 °C for 5 h) under H_2 atmosphere with a flow rate of 50 ml/min. To prevent oxidation and to stabilize the formed Co_2FeGa nanoparticles, the H_2 flow was switched to a methane flow (100 ml/min) at the end of annealing and maintained for 5 min at 850 °C. The samples were naturally cooled to room temperature and collected for analysis.

The effect of precursor composition on the phase of Co_2FeGa nanoparticles was investigated in the range of 1.08 ~ 1.23 mmol for Co, 0.40 ~ 0.50 mmol for Fe, and 0.32 ~ 0.57 mmol for Ga. Co_2FeGa nanoparticles of various compositions were prepared.

To investigate the effect of silica supports on the size of Co_2FeGa nanoparticles, two additional silica materials were used: commercial silica gels (average pore size 6 nm) and synthesized silica spheres (460 nm ± 25 nm in diameter). The silica spheres were synthesized by the Stöber method as reported in the literature [50]. Sample processing parameters used in synthesizing Co_2FeGa nanoparticles using various silica supports were the same as those for the 20 nm silica spheres. For Co_2FeGa nanoparticles prepared using 460 nm silica particles, the annealing time was 24 h and no carbon coating was performed.

To examine the size effect, Co_2FeGa nanoparticles of various sizes were prepared by varying the amount (0.5 g, 1.0 g, 1.5 g, 2.0 g) of 20 nm silica spheres loaded to the precursor solutions. Other processing conditions are identical with the above descriptions. Polycrystalline bulk Co_2FeGa samples were prepared by arc melting of stoichiometric amounts of high purity elements in an argon atmosphere at a pressure of 10^{-4} mbar. The bulk Co_2FeGa compound was annealed at 850 °C in an evacuated quartz tube for one week [29].

2.2   Structural characterizations

The crystal structure of Co_2FeGa nanoparticles was investigated by X-ray powder diffraction using Mo K_α as excitation source and synchrotron radiation based powder X-ray diffraction (XRD) at the beamlines of 01C2 of the National Synchrotron Radiation Research Center (NSRRC, Hsinchu, Taiwan) and 12B2 of Spring 8 (Hyogo, Japan). The X-ray photon energies were 22 keV and 7.12 keV, respectively. Anomalous XRD (AXRD) measurements were performed at the beamline 12B2 of Spring 8 by tuning the photon energies to 7050 eV (off resonant), 7112 eV (Fe K-edge), and 7709 eV (Co K-edge).

X-ray absorption measurements were performed at the beamline 17C1 of the National Synchrotron Radiation Research Center (NSRRC, Hsinchu, Taiwan). The spectra of the samples were collected in the transmission mode. The optical thickness of the powdered samples were adjusted by varying the number of tape layers or using aluminum frames with pre-determined thicknesses such that suitable absorption edge jumps ($\Delta\mu x$) were achieved for Fe (0.3 ~ 0.75) and Co (0.8 ~ 1.1). Standard data analysis procedures were followed [51–55]. The EXAFS spectra $\chi(k)$ were extracted using the AUTOBK program. The ATOMS program was used to prepare the structural input for FEFF6. The final data analysis was performed using the IFEFFIT program package. The EXAFS fits were carried out in the k range of 2.5 ~ 12 Å^{-1} with a k^3-weighting and a Hanning window.

The compositions of the samples were obtained by comparing the edge jumps in the X-ray absorption spectra. This is a nondestructive chemical analysis method and is suitable for carbon coated nanoparticles. General procedures reported in the literature [56] are followed but with some modifications. The raw spectra data for deriving the stoichiometry of the nanoparticles (sample M05) is examplarily shown in Figure 2.1. The XAFS spectra were collected in the transmission mode covering the K-edges of Fe, Co, and Ga (6912 ~ 11364 eV). The data corresponding to different absorbers are then saved in individual files. The data files are input in Athena for energy calibration and normalization and are then output as μ(E) plots. The pre-edge regions (-200 eV to -25 eV) of the plots are linearly fitted and the linear fits are extrapolated to the whole range. The post-edge regions are fitted by quadratic fits from 100 eV after the edge to the whole spectra. The quadratic fits are extrapolated to the pre-edge regions around 10 eV below the edges. The difference between the pre-edge and post-edge fits extrapolated to the edge energy is the edge height. To compensate the variation of edge jump due to difference in atomic number, the obtained jump values are multiplied by the corresponding correction factors (defined as the mole for $\Delta\mu x$ = 1.0) (see Table 2.1) to retrieve the molar ratios of the elements and the compositions of the samples.
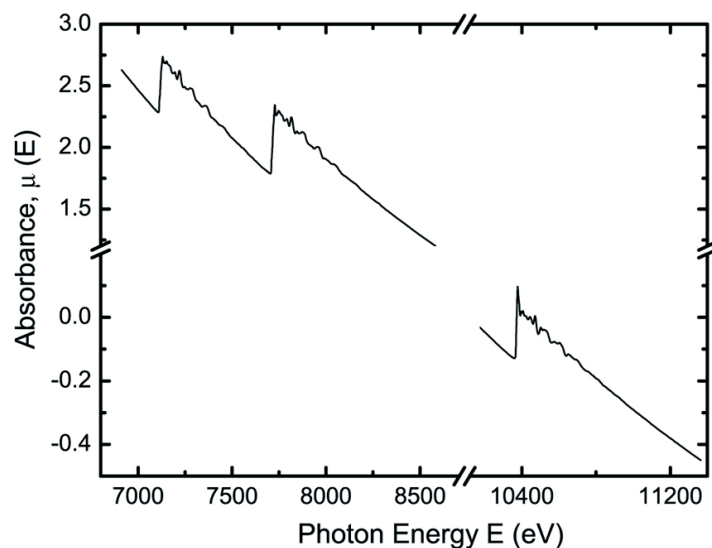

Figure 2.1 A raw XAFS spectrum of sample M05 for stoichiometry determination.

Table 2.1 Absorption correction factors obtained by calculating the amount of elements to reach a $\Delta\mu x$ of 1.0 at the K-edges.

Element	μ below the edge (cm^{-1})	μ above the edge (cm^{-1})	$\Delta\mu$ (cm^{-1})	Thickness for $\Delta\mu x = 1.0$ (μm)	Mass for $\Delta\mu x = 1.0$ (mg/cm^2)	Mole for $\Delta\mu x = 1.0$ (mol/cm^2)	Correction factor
Fe	410.13	3204.32	2794.20	3.58	2.81	5.03	5.03
Co	415.83	3360.66	2944.83	3.40	3.02	5.12	5.12
Ga	180.00	1207.07	1027.08	9.74	5.75	8.25	8.25

In this work, Co_2FeGa-SiO_2@C nanocomposite particles, instead of free-standing Co_2FeGa nanoparticles, were utilized for structural characterizations. From the viewpoint of structural analysis, provided that no new phase such as silicides and carbides form in Co_2FeGa-SiO_2@C nanoparticles, the structure of Co_2FeGa phase should be independent of whether they are free-standing or being embedded into matrices or coated with carbon layers. This is the case for the element-specific short range order characterizations such as EXAFS. In XRD, the diffraction signals from amorphous SiO_2 and graphite layers are superimposed to those reflections from Co_2FeGa phases.

A transmission electron microscope (TEM) Philips EM420 was used for the investigation of particle size, morphology, and size distribution of Co_2FeGa nanoparticles. High resolution TEM (HRTEM), scanning TEM (STEM) and EDX measurements were performed using a FEI Tecnai F30 TEM, equipped with a field emission gun. For TEM sample preparation, individually dispersed Co_2FeGa nanoparticles were obtained by dissolving silica using 10% aq. HF solution for 1 h. The suspended nanoparticles were collected by centrifugation (16,000 rpm, 20 min), washed with de-ionized water for three times and re-dispersed in ethanol. Several drops of the solutions were loaded on carbon coated copper grids and transferred to the microscope after complete dryness. The average particle size was evaluated by counting more than 200 individual particles. For Co_2FeGa nanoparticles prepared using 460 nm silica spheres, individual particles were dispersed in $CHCl_3$. The average particle size was evaluated by counting more than 100 individual particles. The surface morphology of the metal-loaded silica spheres was examined by a scanning electron microscope (SEM) Nova^{TM} nanoSEM 430.

The X-ray microscopic measurements were performed at the beamlines of 01A1 of the National Synchrotron Radiation Research Center (NSRRC, Hsinchu, Taiwan) and 32-ID of the Advanced Photon Source (APS, Argonne, US). The microscope system is a full-field X-ray transmission microscope (nanoXCT®, Xradia Inc.) [57]. The setups of the X-ray microscopes at the beamline 01A1 (NSRRC) and ID32 (APS) are schematically shown in Figure 2.2. At the beamline 01A1, non-monochromated X-rays with an energy range of 4 ~ 30 keV are used and the microscope system is without any X-ray focusing device. For the nanoXCT at the beamline ID32, it uses a set of capillary condensers to match the zone plate lens objectives. The condensers are elliptically shaped glass capillaries. The inner diameter of 0.9 mm was chosen to maximize the vertical acceptance of the APS undulator beam at 65 m from the source. The estimated monochromatic X-ray flux focused by the condenser (after a Si (111) double crystal monochromator) was 2×10^{11} photons per second at 8 keV. The high brightness of the APS and the optimized condensers design yielded an excellent imaging throughput of 50 ms/frame with ~ 1×10^4 CCD counts per pixel. The microscope system can also operate in a Zernike phase contrast imaging mode with a Au Zernike phase ring placed at the back focal plane of the (Fresnel zone plates) FZP objectives. This phase imaging mode increases the contrast for fine features of samples in the hard X-ray region [58,59].
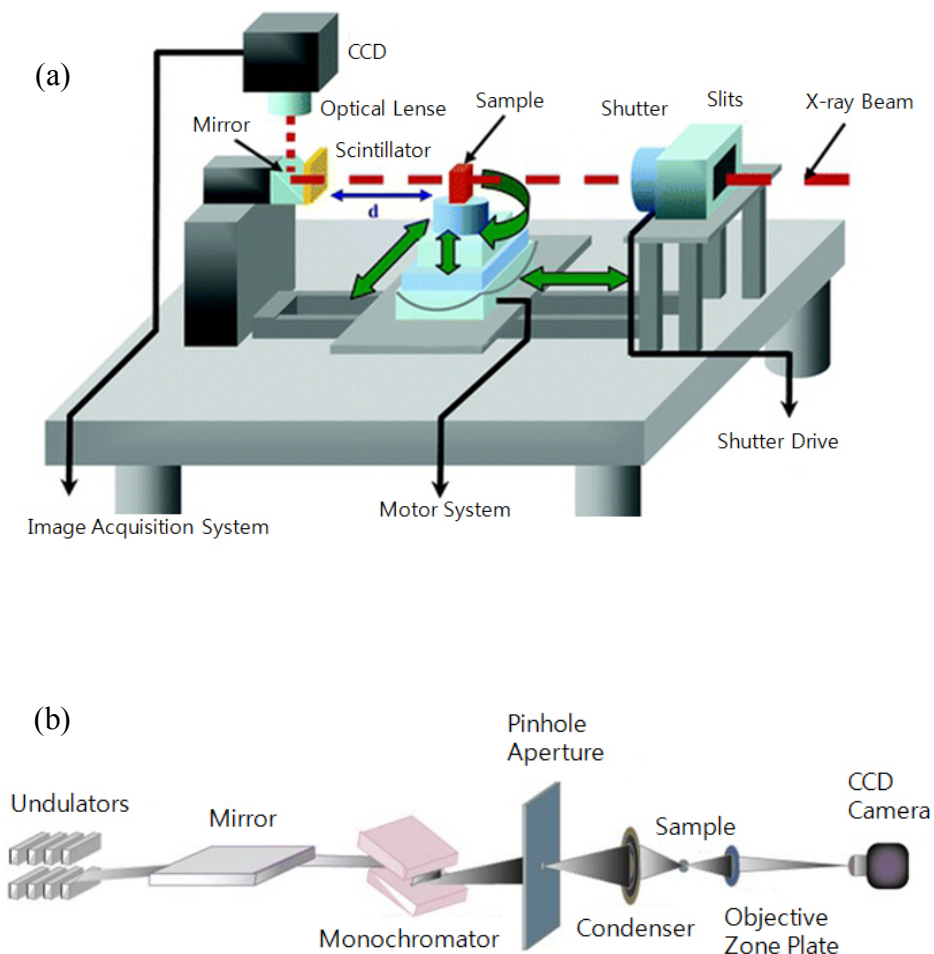
Figure 2.2 Schematic descriptions of synchrotron based full-field transmission X-ray microscope systems at the beamlines 01A1 (a) and ID32 (b).

2.3 Magnetic characterizations

The magnetic properties of the nanoparticles were measured by a superconducting quantum interference device (SQUID, Quantum Design MPMS-XL-5). It is noted that, nanocomposite particles, instead of free-standing nanoparticles, were utilized for structural and magnetic characterizations. To extract the magnetic response of the nanoparticles, the mass fractions (α) of Co_2FeGa nanoparticles in the nanocomposite samples were measured by atomic absorption spectroscopy (AAS) and were used for magnetization calculations. The AAS measurements were conducted on the elements of Fe and Co and the measurement errors were estimated by averaging the two sets of data. Table 2.2 shows the mass fractions of Co_2FeGa nanoparticles in the investigated samples. For magnetic moment calculation, the obtained emu values are converted to μ_B/f.u. by the following correlation:

$$M = m_e * 1.07828 * 10^{20} / (w * \alpha * 0.001 * 6.02 * 10^{23} / m_w) \qquad (2)$$

Here, M   – magnetic moment (μ_B/f. u.);
m$_e$ – experimental magnetization (emu);
w   – weight of the sample (mg);
α – mass fraction of Heusler nanoparticles in samples listed in Table 2.2;
m$_w$ – molar mass of the stoichiometric Heuser compounds (g/mol).

Table 2.2 Mass fractions (α) of the Heusler nanoparticles (NP) in the examined samples.

Sample	Chemical formula	Carbon coating	α
a	Co_2FeGa	100 ml/min for 5 min	0.196 ± 0.050
b	Co_2FeGa	100 ml/min for 5 min	0.125 ± 0.015
c	Co_2FeGa	100 ml/min for 5 min	0.072 ± 0.030
b	Co_2FeGa	No carbon coating	0.125 ± 0.020
b	Co_2FeGa	250 ml/min for 5 min	0.092 ± 0.030
M03	Co_2FeGa	250 ml/min for 5 min	0.120 ± 0.020
M01	Co_2FeGa	250 ml/min for 5 min	0.120 ± 0.015
M04	Co_2FeGa	250 ml/min for 5 min	0.120 ± 0.015
M05	Co_2FeGa	250 ml/min for 5 min	0.140 ± 0.017
M08	Fe_2CoGa	250 ml/min for 5 min	0.115 ± 0.025

To investigate the magneto-structure correlations of Co_2FeGa nanoparticles, [57]Fe Mössbauer spectra were measured using a conventional, constant-acceleration spectrometer at room temperature. For excitation, a [57]Co source was used to deliver γ radiation with a photon energy of 14.4 keV. The Mössbauer data were analysed using the program RECOIL [60]. Temperature dependent Mössbauer measurements were carried out on selected sample in a temperature range of 80 ~ 275 K. Isomer shifts were presented with respect to the bcc Fe foil.

3 Chemical synthesis of Co₂FeGa nanoparticles

This chapter reports the chemical synthesis of silica supported, carbon coated Co₂FeGa nanoparticles. A series of Co₂FeGa nanoparticles of various compositions are prepared and the composition dependent phase structures are investigated by synchrotron radiation X-ray diffraction (XRD), extended X-ray absorption fine structure (EXAFS), and Mössbauer spectroscopy. The influences of silica supports on the size of Co₂FeGa nanoparticles are examined by microscopic characterizations including transmission electron microscopy (TEM), scanning electron microscopy (SEM), and transmission X-ray microscopy (TXM). Furthermore, the formation mechanism of Co₂FeGa nanoparticles is also discussed.

3.1 Introduction

3.1.1 Bulk Co₂FeGa Heusler compounds

Bulk Co₂FeGa intermetallic compounds show high phase stability with an order–disorder transition temperature of 1094 K [61–63]. The Curie temperature of Co₂FeGa was measured as 1093 K by Umetsu et al. using differential scanning calorimetry (DSC) and vibrating sample magnetometer (VSM). It is noted that the order–disorder transition temperature coincides the Curie temperature of Co₂FeGa. The $L2_1$ ordered Co₂FeGa also possess high magnetic moment of 5.17 μ_B at 4.2 K [64].

According to band structure calculations, Co₂FeGa is a type III half-metal, which exhibits a band gap in the minority states but the Fermi level is outside the gap [42]. As summarized by Coey et al. [65], the type III half-metals, also known as "transport half-metals", have localized majority states and delocalized minority states. The DOS at the Fermi level does not vanish for either spin direction and only one type of charge carrier contributes significantly to electric conduction.

Zhang et al. [66] measured the spin polarization ratio of the polycrystalline Co₂FeGa by point contact Andreev reflection (PCAR) technique and reported a SP of 59% at 4.2 K. Although Co₂FeGa is not a type I half-metallic ferromagnet, its SP is higher than those of Ni and Fe (~ 40%) which are widely used in spintronics. Furthermore, high $L2_1$ phase stability, large magnetic moment, and high Curie temperature make Co₂FeGa a promising candidate for spintronic applications.

3.1.2 Co₂FeGa Heusler nanoparticles

For the synthesis of Heusler nanoparticles, physical [38], chemical [39] and mechanical [40–41,67] methods have been reported. 30 nm Fe₃Si Heusler nanoparticles have been fabricated by a modified sputtering method and the XRD analysis indicated the formation of DO_3 ordered Fe₃Si phase [38]. Dahal et al. developed a colloidal approach for synthesizing 4 ~ 7 nm Fe₃Si nanoparticles by reacting the pre-formed iron nanoparticles with silicon tetrachloride at 220 ~ 250 °C [39]. Strictly Fe₃Si nanoparticles are not Heusler nanoparticles due to the DO_3 ordered structure and are not favorable for achieving a high degree of spin polarization. Wang et al. prepared 10 nm Ni₂MnGa Heusler nanoparticles by ball milling and it was found that Ni₂MnGa nanoparticles exhibit similar crystal structure and magnetic properties as their bulk counterpart [40]. In a most recent report, Seo et al. described the formation of Fe₃Si nanowires by a diffusion-driven crystal conversion process based on pre-formed FeSi nanowires [68].

For Co₂FeZ (Z = Al, Si, Ga, Ge) Heusler compounds, Si containing Heusler nanoparticles are not easy to chemically synthesize for their difficulty to reduce. Bulk Co₂FeAl compounds, on the other hand, tend to adopt a $B2$ disordered structure. Co-Mn

based Heusler compounds are also suitable materials for spintronic devices due to their robust HMF behavior [69]. However, the strong tendency of Mn to oxidize might render difficulty in obtaining pure phase.

Recently, the chemical syntheses of binary alloy nanoparticles such as Fe–Co and Fe–Pt in the presence of silica supports have been reported [70,71]. In the present work, this approach was extended to ternary Co$_2$FeGa nanoparticles considering the similarities in electronegativity and atomic radii of Fe, Co, and Ga. The Pauling electronegativity of Fe, Co, and Ga are 1.83, 1.88, and 1.81, respectively. This similarity in electronegativity might be advantages than those with Ge (2.01), Al (1.61), and Si (1.90). Co$_2$FeGa seems to be a good candidate for the chemical synthesis of ternary Heusler nanoparticles for spintronics. In this work, the chemical synthesis and characterizations of the silica supported Co$_2$FeGa nanoparticles are presented [72–74]. This might account for the incipient effort to chemically prepare ternary Heusler nanoparticles.

From the perspective of materials chemistry, chemical preparation of ternary Heusler nanoparticles is challenging. Besides achieving nominal stoichiometry, ordered Heusler phase is also required. In terms of spintronic applications, *L2$_1$* or *B2* ordered phase is preferable to achieve a high degree of spin polarization [75,76]. In a ternary alloy system, structural disorder due to lattice mismatch, immiscibility, and phase separation are frequently encountered. A successful chemical preparation of Co$_2$FeGa nanoparticles with controlled composition, desired phase structure, and particle size is a prerequisite to understand the physical behavior of Heusler compounds at the nanoscale. Even with the progress, the effects of important processing parameters such as precursor composition and silica supports on the stoichiometry, particle size, and crystal structure of Heusler Co$_2$FeGa nanoparticles have not been investigated. A suitable precursor recipe is crucial to achieve stoichiometric composition and to obtain desired phase in Co$_2$FeGa nanoparticles. In addition, similar with other template assisted approaches, the dimension and morphology of the silica supports are expected to play an important role in defining the size and morphology of the formed nanoparticles. Silica supports consisting of silica nanospheres have been used to synthesize alloy nanoparticles [70−71,77]. Au-Ag alloy nanoparticles were prepared by Liu et al. [77] using a variety of silica supports of similar particle/pore size. They found that the particle size of the formed nanoparticles was almost identical regardless the morphology of the silica supports. It would be beneficial to provide some insights on the formation of Co$_2$FeGa nanoparticles within silica matrices. Specifically the present work investigates whether the size of silica spheres affects the size of the obtained Co$_2$FeGa nanoparticles.

3.2   Chemical synthesis

Precursor composition, silica configuration, and annealing are important processing parameters in controlling the structure and size of Co$_2$FeGa nanoparticles. In this work, the effects of the precursor composition and size/morphology of the silica supports were systematically investigated. The annealing temperature (850 °C) was selected as slightly above the reported *B2/L2$_1$* transition temperature (825 °C) [61].

To investigate the effect of precursor composition, a series of Co$_2$FeGa nanoparticles of various compositions were prepared. The investigated precursor compositions are in a range of 1.08 ~ 1.23 mmol for Co, 0.40 ~ 0.50 mmol for Fe, and 0.32 ~ 0.57 mmol for Ga. Firstly, the influences of the amounts of individual metal salts were examined by fixing the amounts of the other two salts. Structural analysis indicates, however, the coexistence of impurity phases and the ordered Co$_2$FeGa phase in all samples. To improve phase purity, Co$_2$FeGa nanoparticles with various Co/Fe ratios in a range of 2.44 ~ 1.17 were prepared. Table 3.1 describes the conditions and the amounts of precursor salts used for these samples. In the synthesis, 20 nm silica spheres were used as supports and the amount of added fume silica was fixed at 1 g. Other processing conditions are identical with the descriptions in *Chapter 2*.

Table 3.1 Precursor composition of Co₂FeGa nanoparticles.

ID	Co [mmol]	Fe [mmol]	Ga [mmol]	Co/Fe (precursor)	Co/Fe (final)
M03	1.16	0.38	0.32	3.05	2.44
M01	1.08	0.47	0.32	2.30	1.89
M04	1.01	0.54	0.32	1.87	1.59
M05	0.84	0.63	0.32	1.33	1.17

To investigate the effect of the size and morphology of the silica supports on the size of Co₂FeGa nanoparticles, two additional silica materials were used: commercial silica gels (average pore size 6 nm) and synthesized silica spheres (460 nm ± 25 nm in diameter). Table 3.2 describes the conditions and the amounts of precursor salts used for these samples. Furthermore, to examine the precursor concentration effect, sample S02 was prepared using a four-fold diluted precursor concentration of that for S01. Samples S03 and S04 were prepared using different annealing times to check the influences of the annealing parameters. In the synthesis of samples S01 ~ S05, the amount of silica supports was fixed at 1 g. Other processing conditions are identical with the descriptions in *Chapter 2*. In addition, the annealing time for sample S05 is 24 h and this sample was free of carbon layers.

Table 3.2 Precursor composition and silica configuration for Co₂FeGa nanoparticles prepared under various conditions.

ID	Co [mmol]	Fe [mmol]	Ga [mmol]	Silica supports	Annealing	Carbon coating
S01	1.08	0.47	0.32	sphere, 20 nm	850° C for 5 h	yes
S02	0.27	0.12	0.08	porous gel, 6 nm (pore)	850 °C for 5 h	yes
S03	1.01	0.54	0.32	porous gel, 6 nm (pore)	850 °C for 5 min	yes
S04	1.01	0.54	0.32	porous gel, 6 nm (pore)	850 °C for 5 h	yes
S05	1.01	0.54	0.32	sphere, 460 nm	850 °C for 24 h	No

3.3 Effect of precursor composition

3.3.1 Long range order structure

The XRD patterns of Co₂FeGa nanoparticles of various compositions are shown in Figure 3.1. The composition and the derived crystal structure of Co₂FeGa nanoparticles are described in Table 3.3. All samples exhibit (220), (400), (422), (440), (620), (444), and (642) reflections for Co₂FeGa compounds. The results indicate the formation of Co₂FeGa phase even though the exact structure type is to be determined due to the absence of superlattice signatures such as the (111) and (200) reflections. Three phases are observed in samples M03, M01, and M04: Co₂FeGa, impurities, and graphite. The main Co₂FeGa phase is found to coexist with certain amounts of impurities. The peak positions of the observed impurity phases are listed in Table 3.4 and 3.5 together with those for the fcc Fe and fcc Co references.

Even though bcc iron and hcp cobalt are more common in nature, the observed impurity phases exhibit a fcc-like structure and might consist of fcc Fe and fcc Co phase. The presence of fcc Co impurities in Fe-Co nanoparticles prepared by a similar approach has been reported [70]. As shown in Figure 3.2, the amounts of the fcc impurity phases, as judged by the fraction of the integrated peak areas of the (111) reflections of the impurities to the Co$_2$FeGa (220) reflections, decrease monotonously in the order of M03, M01, M04 and eventually vanish for M05. This might correspond to the variations of the phase purity of the main phase from ~ 65% of M03 to single phase (100%) of M05. It is noted that the fcc impurity phase is absent in sample M05. The position of the principal reflections shifts to lower angles indicating accompanied variation in the lattice constant. As listed in Table 3.3, the calculated lattice parameter increases in the order of M03, M01, M04, and M05. All calculated lattice constants are close to the reported values for bulk Co$_2$FeGa [61,64].
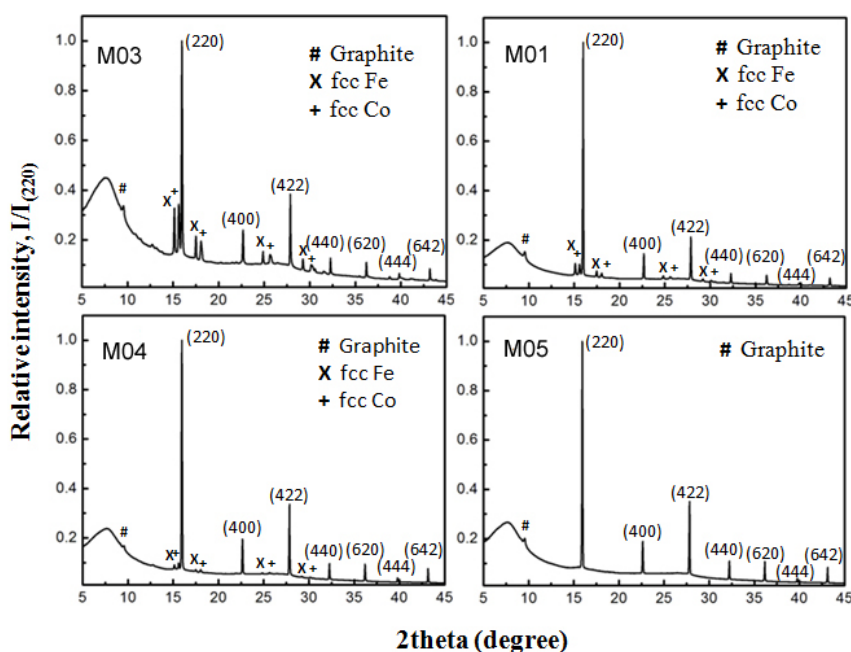
Figure 3.1 XRD patterns of Co$_2$FeGa nanoparticles of various compositions. The indices of the Bragg reflections of the main phase (*L2$_1$* ordered Co$_2$FeGa) are displayed. X-ray photon energy: 22 keV.

Table 3.3 Composition and crystal structure of Co$_2$FeGa nanoparticles.

ID	Composition	a [Å]	Structure
M03	Co$_{0.57}$Fe$_{0.24}$Ga$_{0.19}$	5.7364(1)	Co$_2$FeGa (*DO$_3$*), fcc Fe, fcc Co
M01	Co$_{0.53}$Fe$_{0.29}$Ga$_{0.18}$	5.7344(5)	Co$_2$FeGa (*DO$_3$*), fcc Fe, fcc Co
M04	Co$_{49}$Fe$_{0.32}$Ga$_{0.19}$	5.7393(1)	Co$_2$FeGa (*DO$_3$*), fcc Fe, fcc Co
M05	Co$_{0.42}$Fe$_{0.37}$Ga$_{0.21}$	5.7448(2)	Co$_2$FeGa (*L2$_1$*)

Table 3.4 Bragg reflection position of the fcc Fe-like impurity phases for the samples. X-ray energy: 22 keV.

ID	Reflection (degree)			
	(111)	**(200)**	**(220)**	**(311)**
fcc Fe*	15.38	17.78	25.25	29.70
M03	15.14	17.51	24.86	29.24
M01	15.12	17.48	24.83	29.20
M04	15.13	17.50	24.86	29.24
M05	—	—	—	—

* ICSD # 631730

Table 3.5 Bragg reflection position of the fcc Co-like impurity phases for the samples. X-ray energy: 22 keV.

ID	Reflection (degree)			
	(111)	**(200)**	**(220)**	**(311)**
fcc Co*	15.84	18.31	26.01	30.59
M03	15.64	18.06	25.65	30.17
M01	15.58	18.02	25.60	30.11
M04	15.61	18.03	25.65	30.16
M05	15.47	—	—	—

* ICSD # 622435
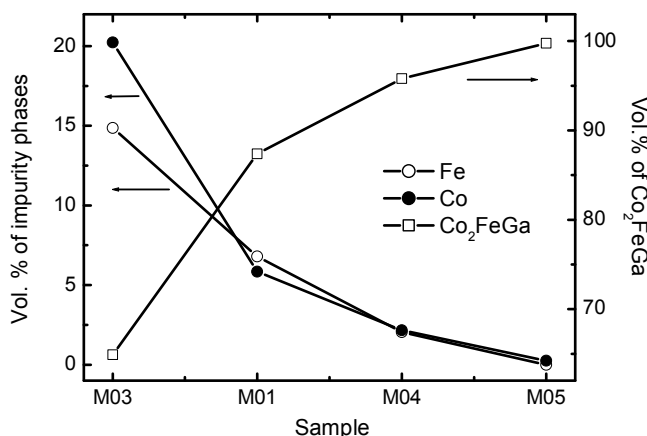
Figure 3.2 The phase composition of samples M03, M01, M04 and M05. The volumetric fractions of the impurity phases (fcc Fe and fcc Co) and the main phase are shown. The ratios of the impurity phases are estimated by comparing the ratios of the integrated areas of the (111) reflections of the impurities and the main phase (220) reflections.

The presence of the above principal reflections for Co$_2$FeGa is insufficient to conclude the *L2$_1$* ordered Co$_2$FeGa. As discussed in *Chapter 1*, several types of ordered structures might occur in Co$_2$FeGa compounds. One way to distinguish between various order types is to monitor the relative intensities of the fingerprint (111) and (200) reflections [78]. According to Table 1.3, the intensity of the (111) reflection is approximately six times of that of the (200) reflection in the *L2$_1$* ordered Co$_2$FeGa compounds. As shown in Figure 3.1, both (111) and (200) reflections are not observed. This might be due to the high X-ray energy, low

intensity of the reflections, and the close approximation and even overlapping of the graphite (0002) and Co$_2$FeGa (111) reflections. Therefore, additional XRD measurements using a X-ray photon energy of 7.12 keV were performed. Figure 3.3 shows the XRD patterns of the samples in a 2theta range of 29.5 ~ 36.5°. Both (111) and (200) reflections are observed in all samples. This confirms the existence of Co$_2$FeGa phase of either $L2_1$ or DO_3 structure.

As summarized in Table 1.3, the major differences between the $L2_1$ or DO_3 structure are the relative intensities of several couples of reflections including (111)/(200), (311)/(222), and (331)/(420). Unfortunately, the latter two reflection couples cannot be resolved. Therefore, the relative intensities of the (111) and (200) reflections are compared for each sample. Due to small intensities and broad reflection profile of the (111) and (200) reflections, their relative intensities ($I_{(111)}/I_{(200)}$) are estimated by examining the relevant integrated area ratios ($A_{(111)}/A_{(200)}$) of the reflections. The ratio for M05 (4.89) is close to the theoretically predicted value for the $L2_1$ ordered structure (5.88). In comparison, the ratios of M01, M03, and M04 are close to the theoretically predicted value for the DO_3 type structure (1.14). It is found that typical $A_{(111)}/A_{(220)}$ ratios are in a range of 0.01 ~ 0.012. These values are comparable to the theoretical values for $L2_1$ ordered Co$_2$FeGa. It is noted that Co$_2$FeGa phase are obtained under nonstoichiometric conditions with excess Co or Fe. No reflection belonging to either metallic carbides or silicates is observed. The Bragg reflections at around 9.55° observed in all samples are assigned to graphite (0002) originating from carbon coating.
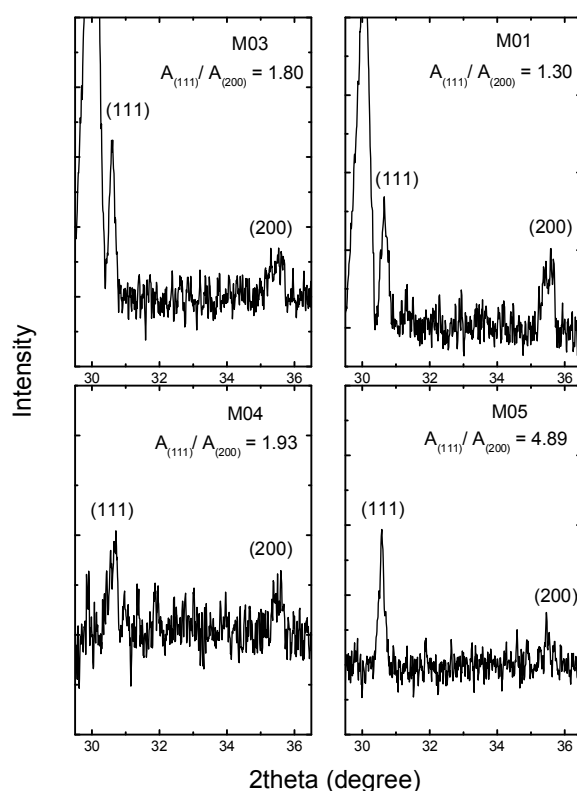
Figure 3.3 Zoom-in XRD patterns in a 2theta range of 29.5 ~ 36.5° of M03, M01, M04, and M05. The corresponding integration area ratios between the (111) and (200) reflections are also given. The reflections with maximums at around 30° for M01 and M03 are attributed to the impurity phases. X-ray photon enoergy: 7.12 keV.

3.3.2   X-ray absorption fine structure

The valence state of the metallic components of the nanoparticles was investigated by X-ray absorption near edge spectroscopy (XANES). At both Fe and Co K-edges, the absorption edge positions are similar to those of the metallic foils with variations less than 1 eV. Therefore, the formation of iron or cobalt oxides is excluded. At Ga K-edge, the absorption edges of all samples are 10370 eV, which is higher than that for metal Ga (10367 eV) but is lower than that for monovalent Ga^+ (10371.5 eV), and Ga_2O_3 reference (10375 eV). As shown in Figure 3.4, the oscillation frequency and magnitude of sample M05 exhibit large discrepancies compared to Ga_2O_3 reference. This indicates that most Ga species in the samples might exhibit a zero valence state within experimental error. Nevertheless, a small amount of gallium oxide cannot be completely excluded.
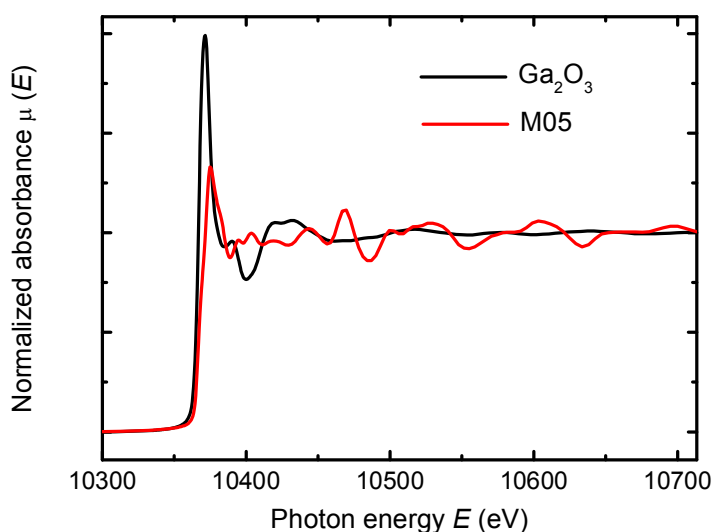
Figure 3.4 Normalized XANES spectra of sample M05 and Ga_2O_3 reference.

The above XRD analyses provide evidence that the obtained Co_2FeGa nanoparticles have either a *L2₁* (M05) or *DO₃* (M03, M01, and M04) structure. Due to the nonstoichiometric feature of the samples, however, there exists the possibility of coexistence of other impurity phase (e.g. bcc Fe) and other structures such as *A2* or *B2* disorder that are not clearly resolved by X-ray diffraction. Extended X-ray absorption fine structure (EXAFS) spectroscopy measurements were carried out. The EXAFS fits were carried out at the Fe, Co, and Ga edges in the *k* range of 2.5 ~ 12 Å⁻¹ with a k^3-weighting in order to achieve a similar resolution for comparison. The calculated theoretical models include Co_2FeGa compounds of different structures (*L2₁*, *A2*, *B2*, and *DO₃*), fcc Fe, fcc Co, bcc Fe, and hcp Co. In the EXAFS fits, only the paths that significantly contribute to the EXAFS signals are adopted. At the K-edges of Fe and Ga, these comprise of four single scattering (SS) paths and one collinear multiple scattering (MS) path along the body diagonal of the primitive cubic cell in the R-range of 1.0 ~ 5.0 Å. In the case of Co K-edge, only five SS paths were adopted in the data analysis.

Firstly, EXAFS fits were carried out on all samples using a *L2$_1$* Co$_2$FeGa model using the experimental lattice constants listed in Table 3.3. Figure 3.5 shows the plots of the magnitude and the imaginary part of the Fourier transforms of EXAFS spectra of the nanoparticles at Co K-edge. In the R-range of 1.0 ~ 5.0 Å, samples M04 and M05 exhibit high degree of structure matching with low *R*-factor values of 0.004 ~ 0.007. The fitted values of *E$_0$* and *ΔR* are physically reasonable. This indicates the presence of Co$_2$FeGa phases with a *L2$_1$* structure in these samples. Samples M03 and M01 are also fitted to the *L2$_1$* Co$_2$FeGa model even though the *R*-factors are higher than those for samples M04 and M05. It is consistent with the XRD-revealed coexistence of substantial amount (> 5%) of fcc Co impurities, which exhibit large structural discrepancies with the main Co$_2$FeGa phase in the samples. The above results indicate that the Co$_2$FeGa phases in all samples might have a *L2$_1$* structure. EXAFS fits are also carried out on the first coordination shells. The first shell of the *L2$_1$* ordered Co$_2$FeGa is a mixed one consisting of four Fe atoms and four Ga atoms with equal bond distance from the Co absorbers. In a perfect *L2$_1$* ordered Co$_2$FeGa phase, the inter-atomic distances of Co–Fe and Co–Ga should be equal. By performing first shell fits of the samples, the corresponding bond lengths are obtained. The Co–Fe and Co–Ga bonds of samples M04 and M05 are found to be 2.45 Å and 2.47 Å, respectively. The uncertainty of inter-atomic distance in EXAFS analysis is approximately 0.01 ~ 0.02 Å. This verifies the high degree of *L2$_1$* ordering present in these samples. In comparison, larger bond length differences of 0.03 Å and 0.07 Å are found for samples M01 and M03. It is noted that the fits using either fcc Co or hcp Co are not satisfactory.

At Fe K-edge, as shown in Figure 3.6, the fits in the R-range of 1.0 ~ 5.0 Å are reasonably good for all samples. From the fits in the first coordination shells, a better structural matching is found in samples M01, M04 and M05. The relatively poor fitting quality in M03 might be related to the excess fcc Fe as revealed by XRD. The fitting quality is not satisfactory for the fits using fcc Fe as the structural model. The fits assuming a bcc Fe structure, however, are of reasonable qualities for all samples. This might be explained in terms of two aspects. First, this might point to bcc Fe impurities, which are not resolved by XRD. This is possible especially for sample M04 and M05 which are with excess Fe but with less or free of observable impurity phases. On the other hand, EXAFS technique might be incapable to differentiate Fe, Co and Ga scatters under certain conditions. Fe, Co, and Ga are at the same row in the periodic table and the maximum difference in nuclear charge of the elements is ~ 5. The bcc lattices constitute the blocking units of a *L2$_1$* structure. Therefore, the evidence for a *L2$_1$* structure derived from EXAFS at Fe K-edge is insufficient to conclude a *L2$_1$* structure of Co$_2$FeGa. Additional EXAFS probes on other absorbers are required.
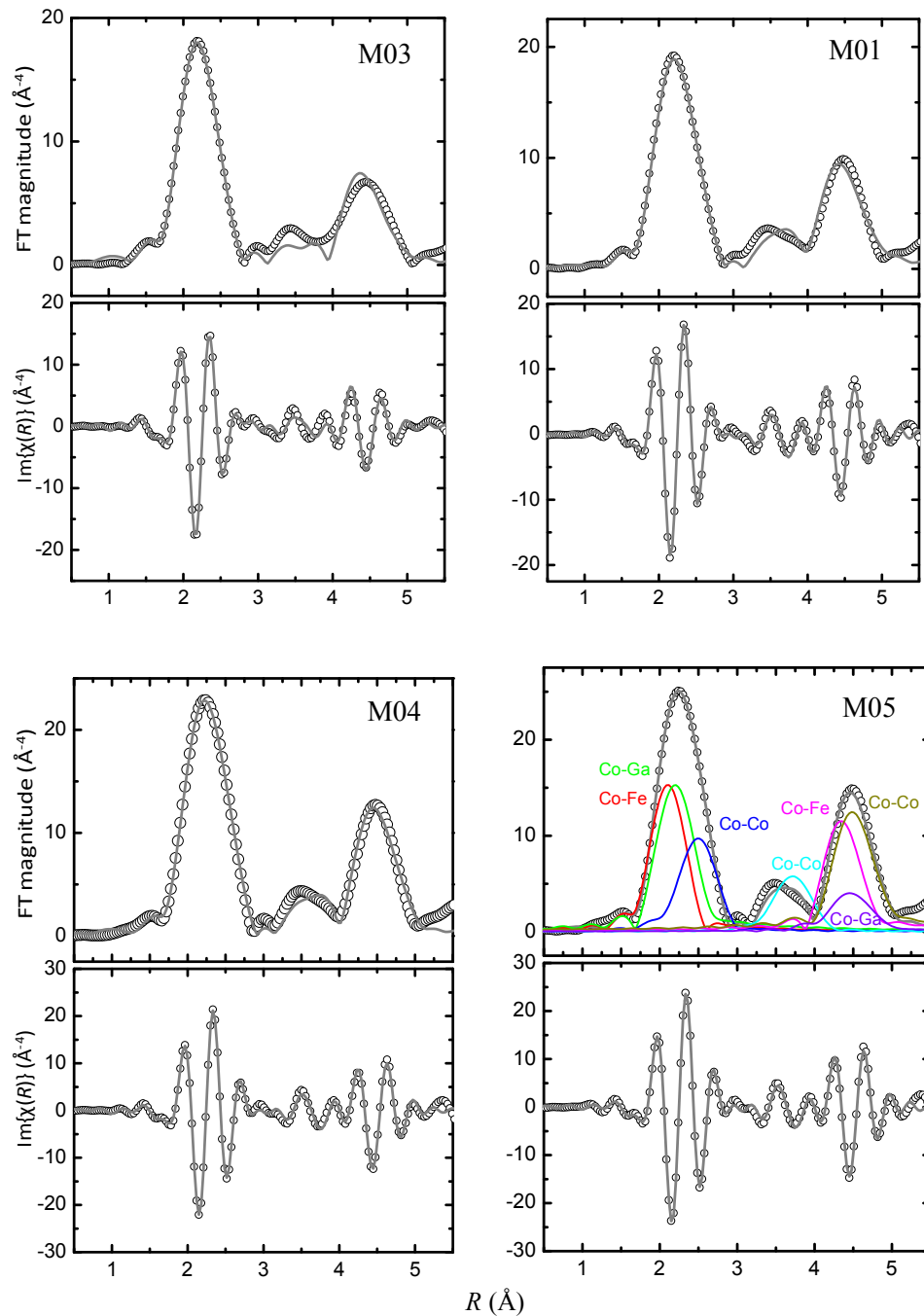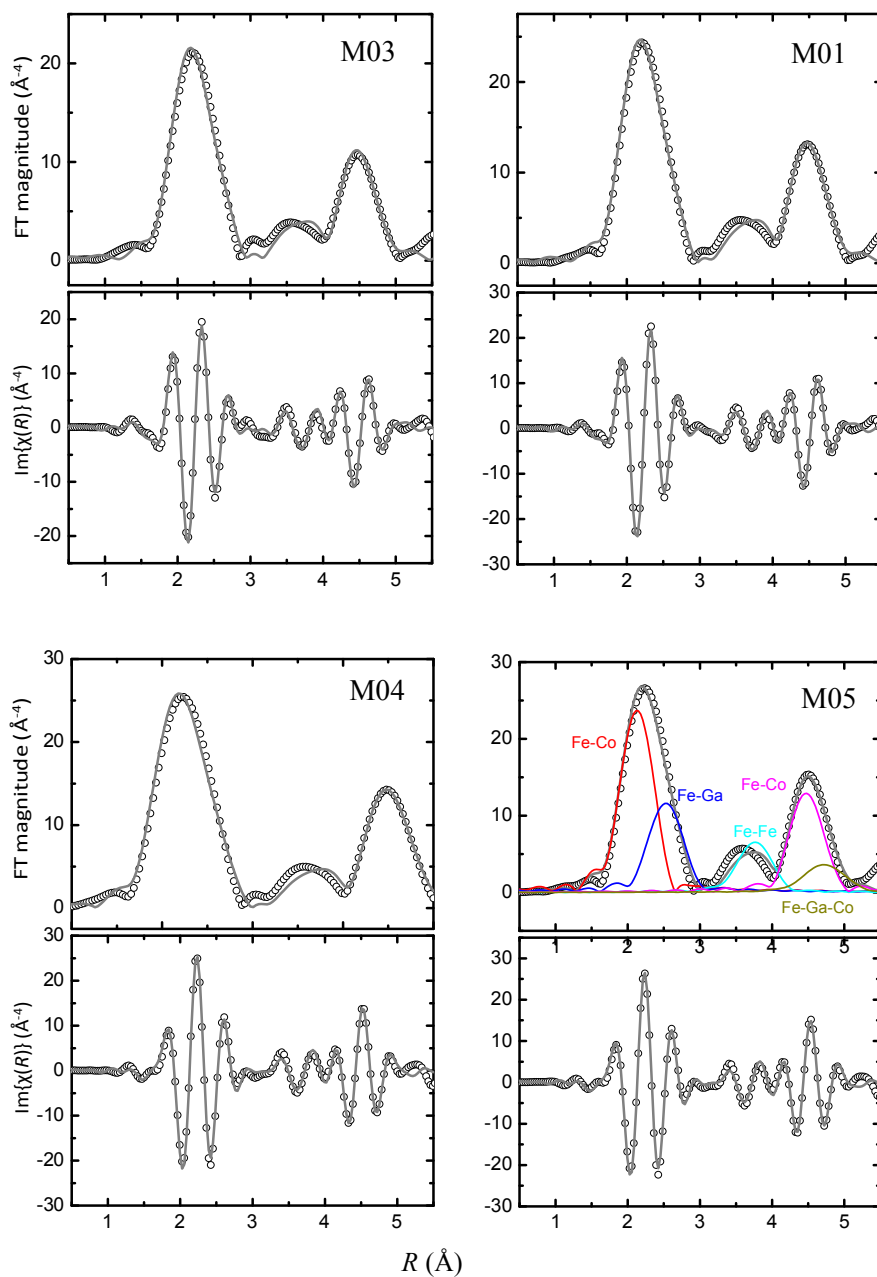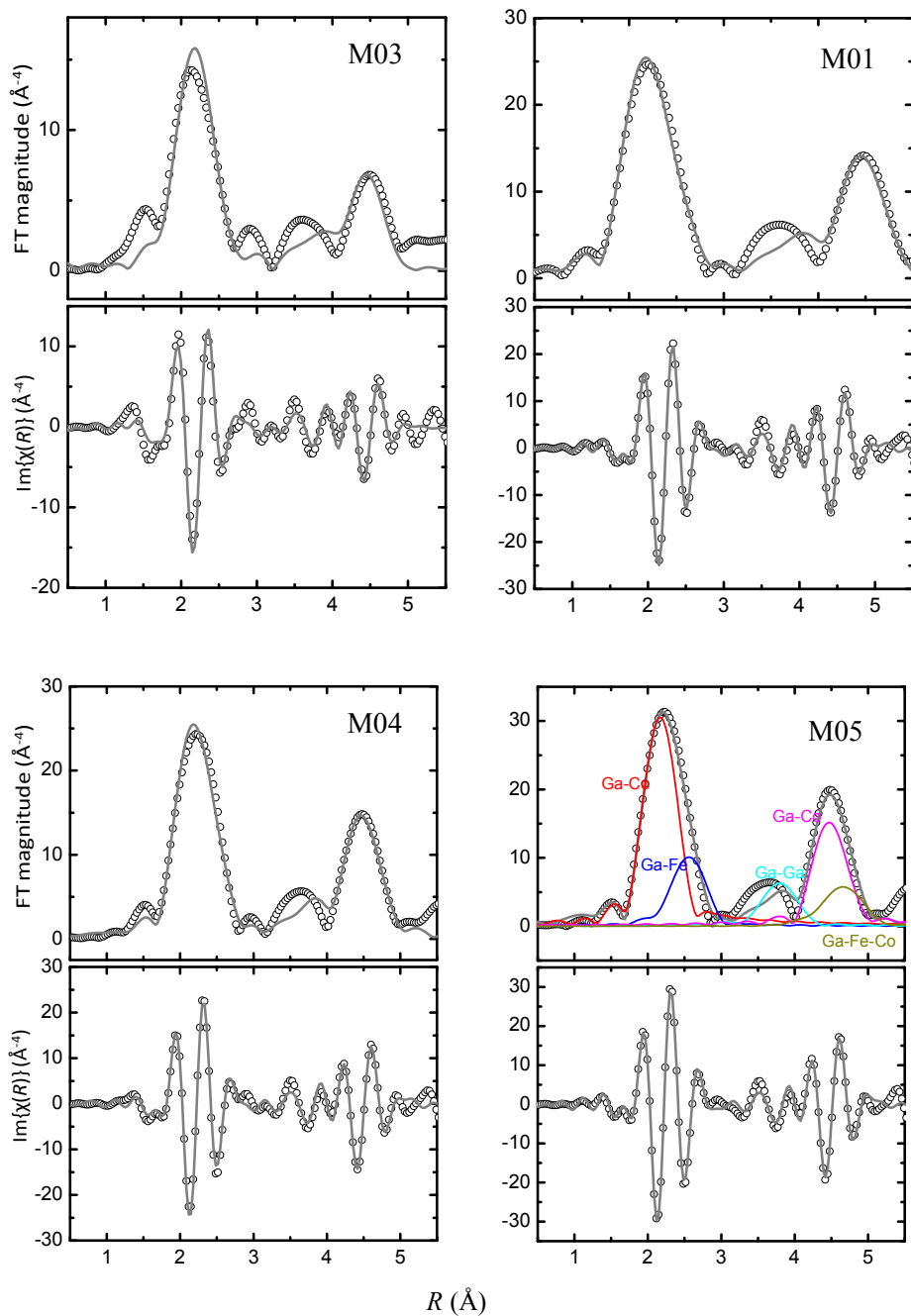
Figure 3.5 Magnitudes and imaginary components of Fourier transforms of EXAFS spectra of the nanoparticles at Co K-edge. The fits using a $L2_1$ Co₂FeGa model are shown as solid lines. The paths are displayed considering the results of the fits for sample M05 (i.e. having been modified by appropriate values of S_0^2, σ^2, and other parameters). The shown spectra are not corrected for the phase shifts.

Figure 3.6 Magnitudes and imaginary components of Fourier transforms of EXAFS spectra of the nanoparticles at Fe K-edge. The fits using a $L2_1$ Co₂FeGa model are shown as solid lines. The paths are displayed considering the results of the fits for sample M05 (i.e. having been modified by appropriate values of S_0^2, σ^2, and other parameters). The shown spectra are not corrected for the phase shifts.

EXAFS fits at Ga K-edge were carried out to provide additional evidence of the formation of $L2_1$ Co$_2$FeGa phase in the samples. As shown in Figure 3.7, from the point of view of Ga absorbers, the short range order structure of sample M03 cannot be described by the $L2_1$ Co$_2$FeGa model. This might be related to excess Co and Fe in this sample. Part of excess Fe and Co atoms might occupy the nominal Ga sites. As a result, the fitted Ga–Ga bond length varies significantly from the nominal value of 4.056 Å. For samples M01, M04 and M05, the R$_F$ values for the EXAFS fits are in a range of 0.017 ~ 0.025 indicating overall good fitting qualities. The improvement in Ga EXAFS fitting quality correlates well to the amount of the impurity phases. Among all samples, the optimal fits are achieved in sample M05 that are free of fcc impurities even still with excess Fe. The above observations are closely associated with the nonstoichiometric feature of the samples. The EXAFS fitting quality at Ga edge, however, is not as good as for the fits at the Fe and Co edges for all samples. It seems that EXAFS probes at Ga edge are more sensitive to stoichiometry of the samples than those at Co and Fe edges.

EXAFS fits are also carried out for all samples assuming a variety of structure models ($A2$, $B2$, and DO_3) of Co$_2$FeGa. At the K-edges of Co, Fe, and Ga, better fitting qualities are obtained for a DO_3 structure rather than a $A2$ or $B2$ model. Compared to the $L2_1$ ordered Co$_2$FeGa, the Co and Fe sites are interchangeable in a DO_3 structure. The similarities in the backscattering amplitude and phase shift of Fe and Co [79], however, make it difficult to differentiate between the $L2_1$ and DO_3 structures. The major objective of EXAFS analysis in this work is to reveal the composition dependent short range order and provide evidence on the structure of Co$_2$FeGa phase in the samples. The impurity phases, however, makes it difficult to quantitatively evaluate the antisite disorder in Co$_2$FeGa.

Figure 3.7 Magnitudes and imaginary components of Fourier transforms of EXAFS spectra of the nanoparticles at Ga K-edge. The fits using a *L2₁* Co₂FeGa model are shown as solid lines. The paths are displayed considering the results of the fits for sample M05 (i.e. having been modified by appropriate values of S_0^2, σ^2, and other parameters). The shown spectra are not corrected for the phase shifts.

3.3.3 Magnetic properties

[57]Fe Mössbauer spectroscopy is sensitive to the site occupation of Fe atoms and is capable to distinguish between the *L2₁* and *DO₃* structure of Heusler compounds. Figure 3.8 shows the [57]Fe Mössbauer spectrum of sample M05. The fitted Mössbauer parameters for the sample M05 are given in Table 3.6. The Mössbauer spectrum was fitted using one paramagnetic doublet and two magnetic sextets. The two sextets in the Mössbauer spectrum indicate two different local environments surrounding Fe atoms. The bulk Co₂FeGa is characteristic of a single sextet with H_{hff} of 310 kOe and IS of 0.05 ± 0.03 mm/s [80]. Therefore, the hyperfine magnetic field of the first sextet (314 kOe) is close to the reported H_{hff} value for bulk Co₂FeGa phase confirming the formation of ordered Co₂FeGa phase. The second sextet has a hyperfine magnetic field close to 324 kOe (typical for bcc Fe). It might be attributed to the bcc Fe due to excess Fe in the sample. It is noted that bcc Fe impurities are not resolved by XRD measurements due to the complete overlap of Bragg reflections for bcc Fe and Co₂FeGa. If the samples are ordered in *DO₃* structure or a substantial amount of *DO₃* disorder coexists with the *L2₁* structure, Fe atoms occupying the 4c or 4d site exhibit an additional sextet with a hyperfine magnetic field of 220 kOe [80]. The absence of this sextet definitely excludes the occurrence of *DO₃* disorder in this sample. The doublet is assigned to the nanoparticles with the particle size smaller than the critical superparamagnetic size limit of Co₂FeGa.
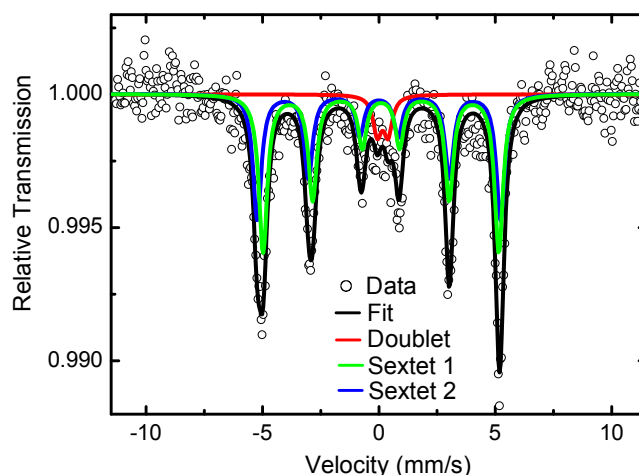
Figure 3.8 Mössbauer spectrum of M05 at room temperature. Superparamagnetic doublets and static magnetic sextets are shown by red, blue, and green lines.

Table 3.6 Fitted Mössbauer parameters (isomer shift δ, quadrupole splitting Δ, and hyperfine field H_{hf}) of sample M05.

ID	δ (mms⁻¹)	Δ (mms⁻¹)	H_{hf} (kOe)	Area (%)
M05	0.16	0.46	—	6.3
	0.08	0	314.0	52.3
	0	0	324.0	41.3

Figure 3.9 shows the magnetization curves at 5 K and 300 K for sample M05. The nanoparticles are magnetically soft with the saturation magnet moments are 4.14 μ_B and 4.23 μ_B at 5 K and 300 K, respectively. The measured saturation magnetizations of sample M05 are significantly lower than the reported value for bulk Co$_2$FeGa [64] and the value predicted by the Slater–Pauling rule. This might be attributed to the bcc Fe impurities as revealed by the Mössbauer spectroscopy discussed above. The presence of bcc Fe impurities in this sample make it difficult to directly compare the experimental data to that derived from a structural model of perfectly ordered Co$_2$FeGa phase since the mass fraction of Co$_2$FeGa phase in the sample has been overestimated.
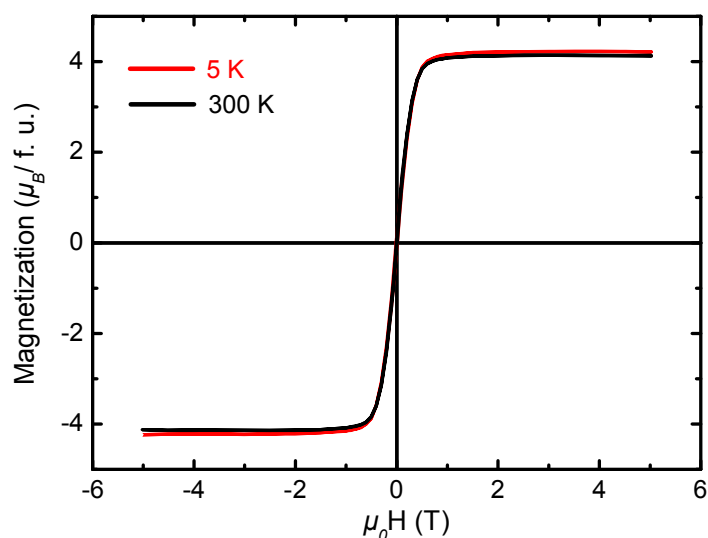
Figure 3.9 Magnetization curves of sample M05 at 5 K and 300 K.

3.4   Effect of SiO$_2$ supports

3.4.1   Transmission electron microscopy

The transmission electron microscope (TEM) micrographs in Figures 3.10 ~ 3.12 show the morphologies of a variety of silica supports and Co$_2$FeGa particles obtained using the corresponding silica supports. For sample S04, as revealed in Figure 3.10 (a), the average pore size is around 6 nm. Co$_2$FeGa nanoparticles with a broad particle size pattern (5 ~ 50 nm) are formed as shown in Figure 3.10 (b) and (c). The particle size of sample S01 deriving from the 20 nm silica spheres is 17.8 nm ± 9.3 nm (see Figure 3.11 (a) ~ (c)), which is comparable to the size of the corresponding silica particles. As shown in Figure 3.11 (a), the synthesized silica spheres are uniformly dispersed with an average particle size of 460 nm ± 25 nm. The size of the sample S05 using the 460 nm silica spheres is in the range of 200 nm ~ 600 nm (see Figure 3.12 (b) ~ (c)).
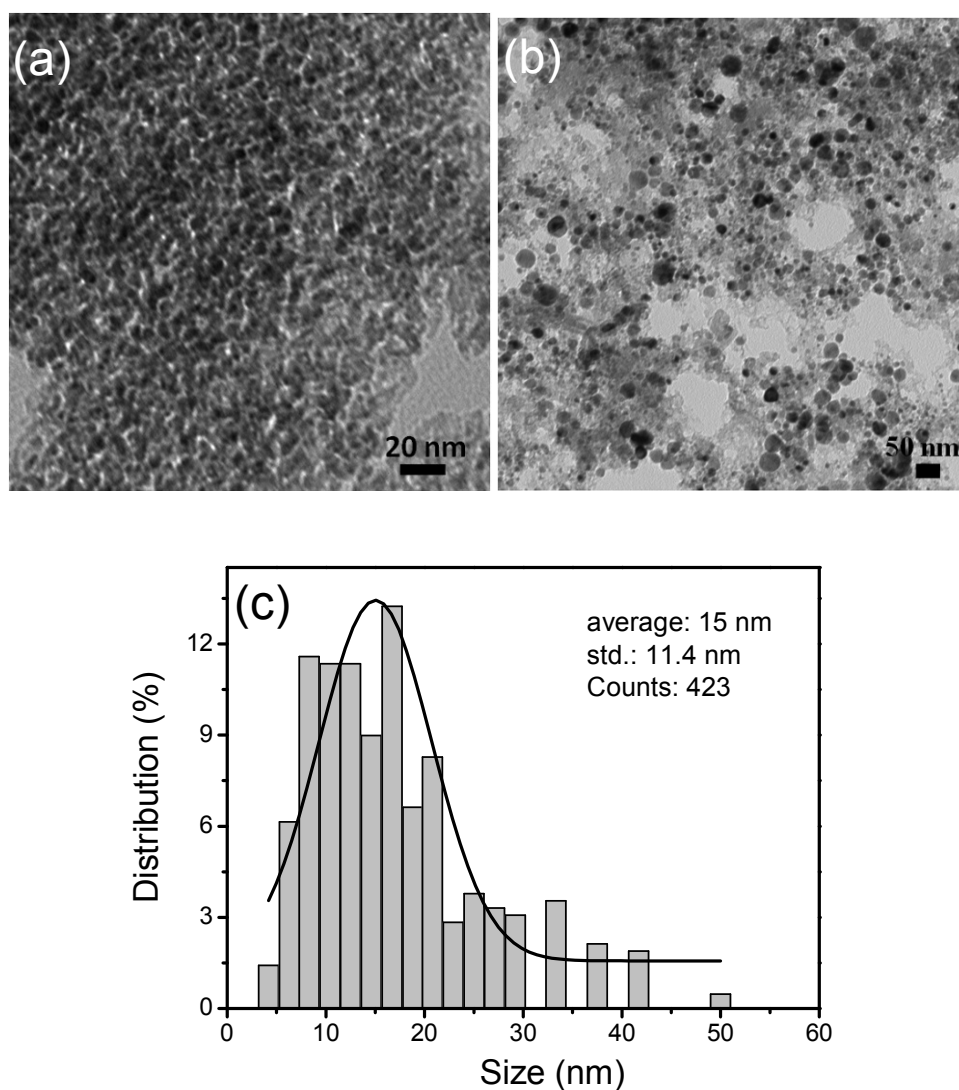
Figure 3.10 TEM micrographs of silica gel (a) with an average pore size of 6 nm and sample S04 (b) using the gel supports. The size distribution of the nanoparticles is shown in (c). The histogram is fitted with a Gaussian curve.
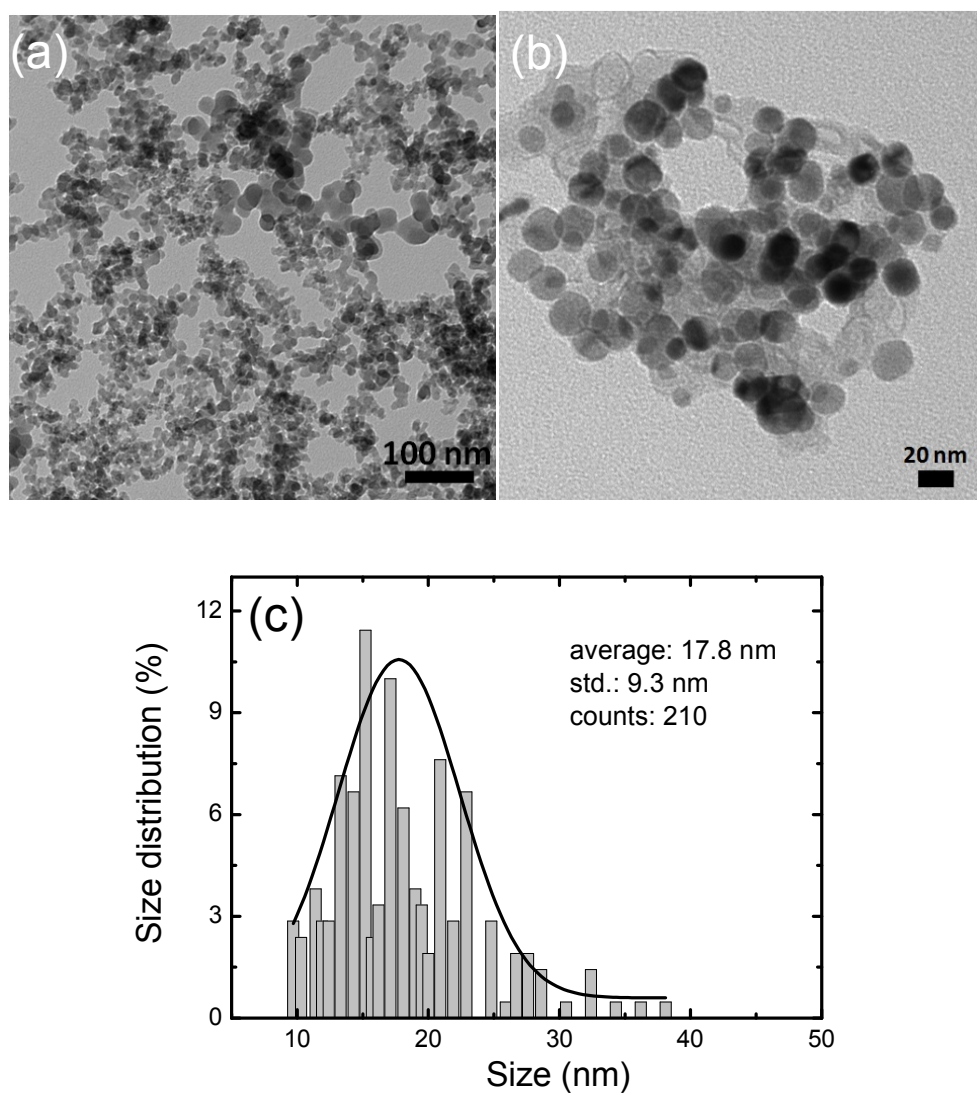
Figure 3.11 TEM micrographs of fume silica (a) with an average particle size of 20 nm and sample S01 (b) using the fume silica. The size distribution of the nanoparticles is shown in (c). The histogram is fitted with a Gaussian curve.
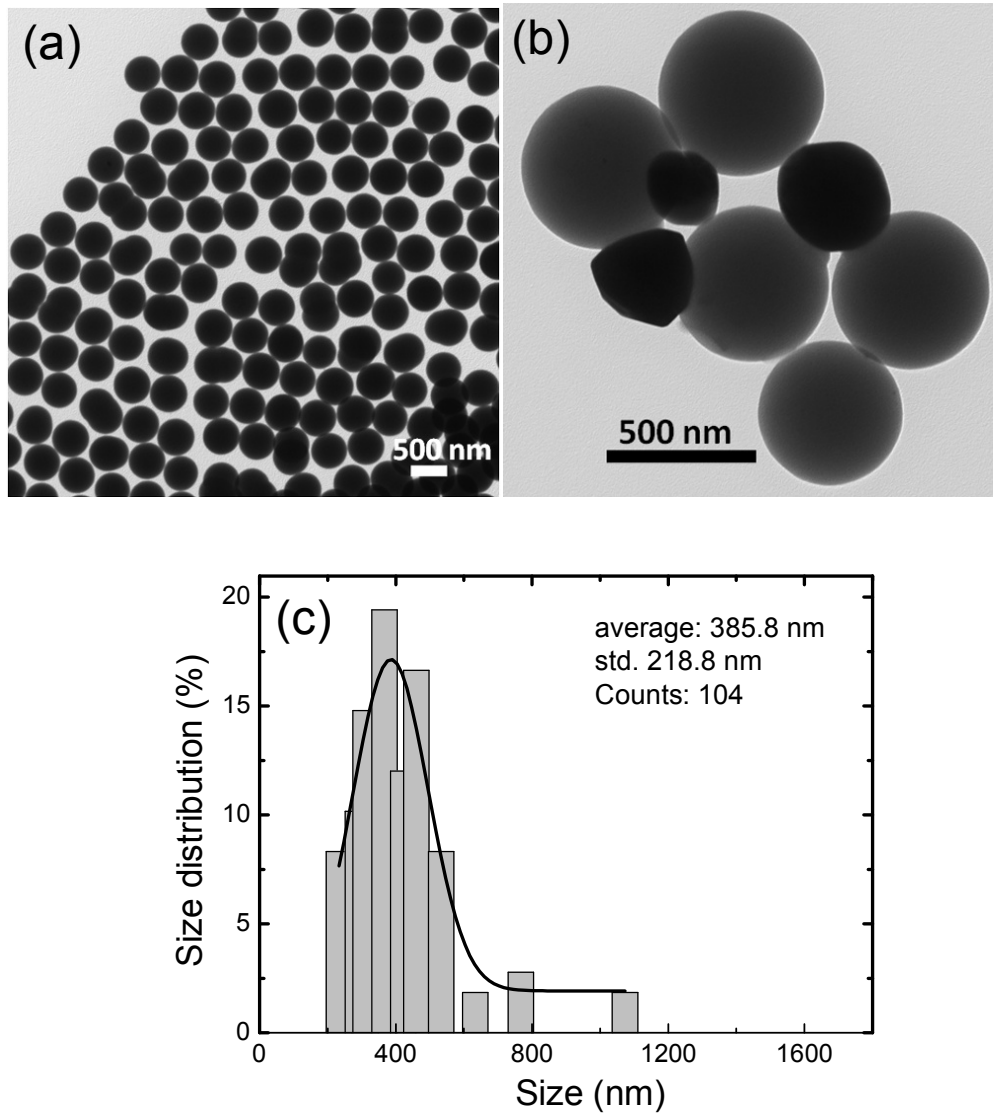
Figure 3.12 TEM micrographs of silica spheres (a) with an average particle size of 460 nm and sample S05 (b) using the silica spheres. The particle size distribution of the nanoparticles is shown in (c). The histogram is fitted with a Gaussian curve.

3.4.2   Scanning electron microscopy

Scanning electron microscopy (SEM) was used to reveal the surface morphology and pore structure of the silica aggregates after loading the metal salts. For the 20 nm silica aggregate, a nanoporous structure is observed in Figure 3.13 (a). The minimum size of the pores is comparable to that of individual silica sphere. In the case of 460 nm silica spheres (see Figure 3.13 (b)), primary silica aggregates with a dimension of tens of micrometers are formed by the closely packing of silica particles. Figure 3.13 (c) shows an enlarged view of a part of one silica aggregate in Figure 3.13 (b). It is observed that pore structures are also formed within the silica aggregates. An imaginary pore structure configured by a few closely located silica spheres is indicated by the dotted circle in Figure 3.13 (c). The brighter spots indicated by arrows might be due to the metal salts deposited on the silica surfaces and located within the inter-particle spaces.

3.4.3   Transmission X-ray microscopy

Figure 3.14 shows the transmission X-ray microscopy (TXM) micrographs of the 460 nm silica spheres loaded with metal precursors before and after annealing. As a nondestructive probing tool, transmission X-ray microscope (TXM), with a resolution at nanometer scale, is capable to resolve the three-dimension morphology of nano- and micro-structures [81]. The advantages of TXM technique include minimal sample preparation, a wide applicability to objects of various length scales (nano-to-micro meter) and the capability to observe in situ and in real time [82]. Thus, TXM is valuable to provide complementary morphological information of the silica supported Co$_2$FeGa nanoparticles. As described in Figure 3.14 (a), the silica spheres formed aggregates with a dimension of tens of micrometers, which is consistent with the SEM image shown in Figure 3.13 (b). After high temperature annealing under H$_2$, the metal precursors accommodated in the pore space are converted to metal nanoparticles. As shown in Figure 3.14 (b) for sample S05, the formed Co$_2$FeGa nanoparticles (black dots) are dispersed within the silica matrices. By performing X-ray tomography, the three dimensional morphology of the aggregates of Co$_2$FeGa@silica nanoparticles could be resolved. Representative slices from a re-constructed tomography movie are shown in Figures 3.14 (c) to (e). It is observed that Co$_2$FeGa nanoparticles are formed within the silica aggregates.
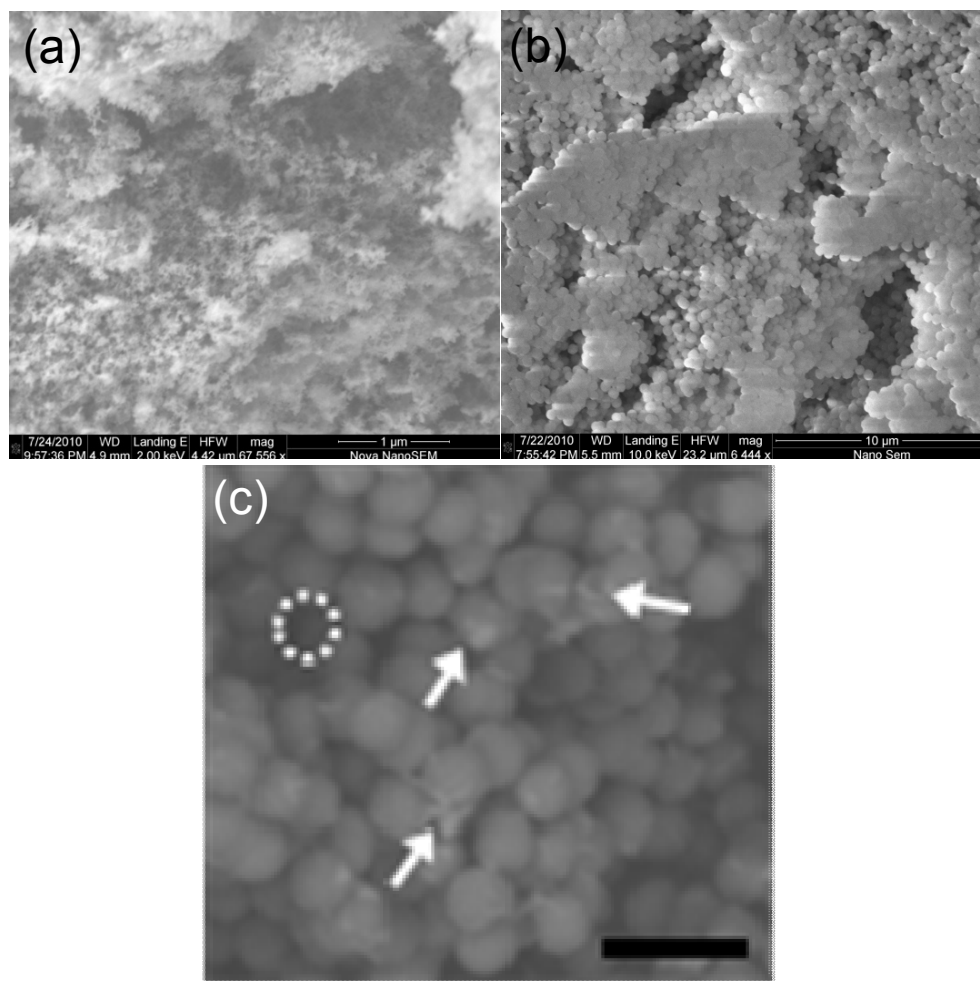
Figure 3.13 SEM micrographs of silica aggregates composed of silica spheres of various sizes after loading metal salts and drying: (a) 20 nm; (b) 460 nm. An enlarged view of the 460 nm silica aggregates is shown in (c). The white arrows in (c) indicate the locations of deposited metal salts. The dotted circle denotes an imaginary pore structure configured by a few closely located silica spheres. The scale bar in (c) is 1 μm.
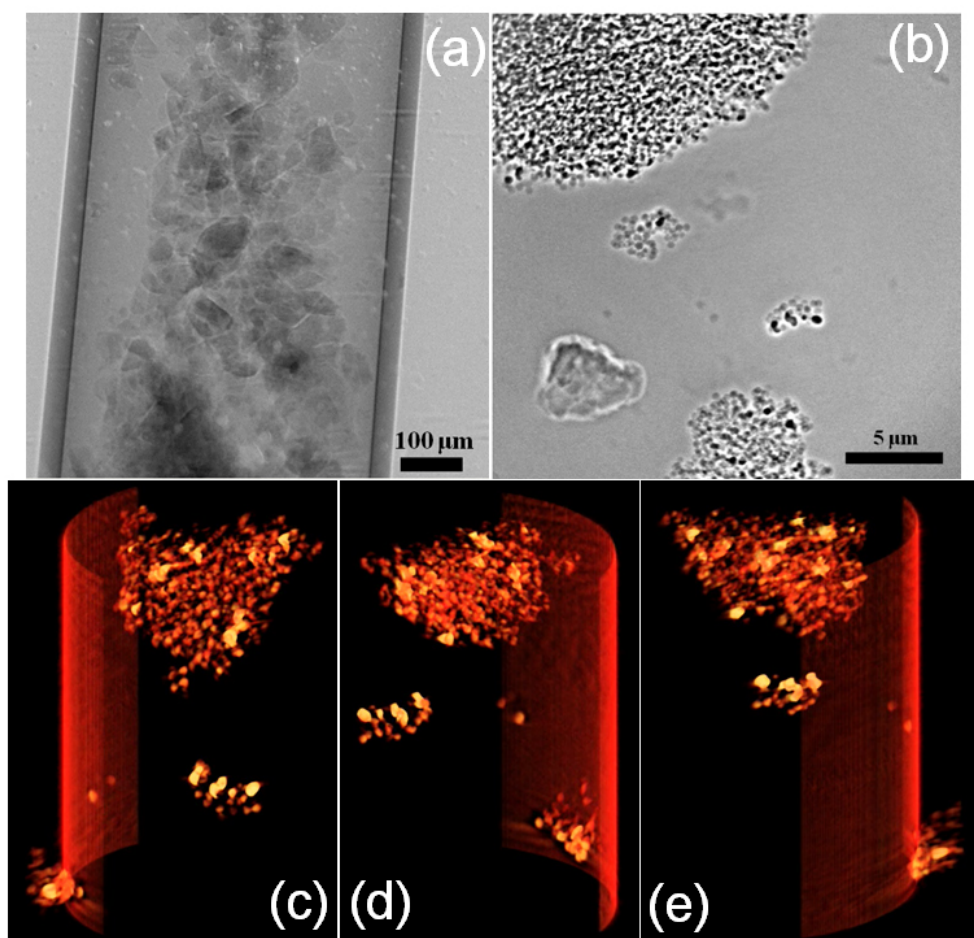
Figure 3.14 TXM micrographs of Co$_2$FeGa@silica nanoparticles using 460 nm silica spheres (sample S05): (a) before annealing; (b) after annealing. Representative slices at three rotation angles from a reconstructued tomography movie are shown in (c) to (e).

3.5   Formation mechanism of Co$_2$FeGa nanoparticles

The formation of carbon coated Co$_2$FeGa nanoparticles might involve several steps including loading the metal precursors within silica matrices, high temperature reduction and subsequent carbon coating. After solvent removal, the metal loaded silica opals are condensed and the silica particles formed pores of specific dimension and morphology. The metal precursors accommodated in such inter-particle voids are treated by high temperature annealing under H$_2$ atmosphere to form nanoparticles. The graphite layers are deposited onto the particle surfaces by a chemical vapor deposition process using methane. Free-standing Co$_2$FeGa nanoparticles can be obtained by removing the silica supports using HF acid etching. A schematic illustration of the chemical synthesis of carbon coated Co$_2$FeGa nanoparticles using silica supports is shown in Figure 3.15.
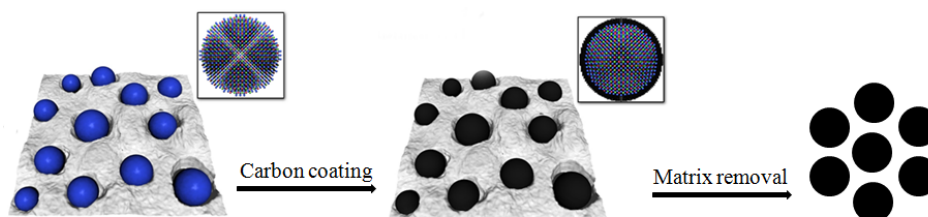
Figure 3.15 A schematic illustration of the chemical synthesis of free-standing carbon coated Co$_2$FeGa nanoparticles using silica supports.

Little experimental work has been carried out to understand the role of silica size in tuning the particle size and morphology of the formed nanoparticles. In this work, silica spheres of various sizes (20 nm and 460 nm) were employed to prepare Co$_2$FeGa nanoparticles. It is speculated that increasing the amount of silica nanospheres might decrease the concentration of the precursors. As reported by Seo et al. [70], the average particle size decreased from 7 nm to 4 nm with a four-fold decrease in the precursor concentration for Fe-Co alloy nanoparticles. Larger Co$_2$FeGa nanoparticles, however, were obtained in this study and a bimodal dispersion pattern developed at a higher silica load. In conventional wet impregnation methods, nanoporous templates are utilized and particle size is controlled by the pore size and porous structure. The pore size might set an upper size limit and the size of the obtained nanoparticles might be smaller than the dimension of the pores. Instead of the hard pore structures in silica gels, an assembly of packed silica spheres also extrinsically generates pore-like structures which host reaction events such as nucleation and growth of nanoparticles. Therefore, the size and morphology of the pore structures formed by sphere packing might be important in affecting the size of the formed Co$_2$FeGa nanoparticles. Adjusting the size of silica spheres might change the interparticle voids, which in turn facilitates the formation of Co$_2$FeGa nanoparticles of various sizes. This speculated model, however, is difficult to testify since the morphology of the voids is difficult to evaluate in situ by microscopic investigations. Typical sample preparation procedures in TEM and SEM involving dispersion and complete dryness might destroy the pristine pore structure. Even though minimal sample preparation is required for TXM, the suitable length scale of the particles for TXM studies is normally larger than 100 nm for the state-of-the-art TXM instrumentations. This claims for further TXM investigations using silica spheres with a variety of size in a range of 100 ~ 500 nm.

It is also noted that the size of Co$_2$FeGa nanoparticles prepared by this approach might be also affected by other variables such as precursor concentration. The formation of pores with specific size alone is necessary but insufficient to obtain nanoparticles with a desired size distribution. For Co$_2$FeGa nanoparticles prepared using nanoporous silica gels, the formation of metal nanoparticles with a size much larger than the pore size (6 nm in diameter) might be attributed to higher precursor concentrations in the present approach, which is around 1.8 times of that used for Fe-Co nanoparticles in the literature [70]. As also shown in Figure 3.13 (c), the unevenly deposited metal salts within the pores might eventually result in metal nanoparticles with an abnormal size distribution. Further efforts are underway to optimize the processing parameters and to clarify the role of silica spheres in controlling particle size and to improve size distribution.

3.6 Summary

In summary, silica supported, carbon coated, Co$_2$FeGa nanoparticles of various compositions are prepared by a chemical method. The dependences of Co$_2$FeGa phase structure on precursor composition are investigated. It is found that fcc impurities normally coexist with the main Co$_2$FeGa phase under conditions of excess Co and Fe. The formation of $L2_1$ ordered Co$_2$FeGa phase is verified by analyzing the XRD and EXAFS spectra at the K-edges of Fe, Co, and Ga. The Mössbauer data exclude the presence of DO_3 disorder which is difficult to reveal by X-ray methods. The morphologies and dimensions of the silica materials are found to affect the morphology and particle size of the formed Co$_2$FeGa nanoparticles. Microscopic investigations reveal that the size of the formed Co$_2$FeGa nanoparticles might be tuned by using silica spheres of various sizes. The pores formed by closely packing silica spheres are important to control the size of the formed Co$_2$FeGa nanoparticles.

4 Size Effects in Co$_2$FeGa Nanoparticles

Particle size plays an important role in determining the structure, biological, physical, and chemical properties of technologically oriented nanoparticles [83–87]. For Heusler compounds particle size is an added degree of freedom to tailor the structure and properties besides the conventional avenues such as composition, chemical doping, and applying pressure. In this chapter, Co$_2$FeGa nanoparticles with a variety of sizes are prepared and the size dependent crystal structure and magnetic properties are investigated. Furthermore, the superparamagnetic size limit of Co$_2$FeGa Heusler nanoparticles is determined by correlating the TEM derived particle size to the Mössbauer spectroscopy data.

4.1 Transmission electron microscopy

The composition and structure of Co$_2$FeGa nanoparticles are summarized in Table 4.1. Particle morphology and size distribution of Co$_2$FeGa nanoparticles were analyzed by a transmission electron microscope (TEM). Without HF etching, the phase contrast between Co$_2$FeGa and SiO$_2$ supports is poor. Therefore HF etching is necessary to evaluate the particle size distribution of Co$_2$FeGa nanoparticles using TEM. As shown in Figures 4.1 to 4.3, the particle size depends on the amount of silica supports in sample preparation, i.e. the more silica added, the smaller particle size obtained. For sample **a**, a very broad particle distribution appears with sizes ranging from 40 ~ 120 nm. Increasing the silica weight to 1g (sample **b**), the Co$_2$FeGa nanoparticles are smaller with improved size dispersion (17.8 nm ± 9.3 nm). For sample **c**, however, a bimodal size distribution develops and both larger and smaller particles coexist. The dependence of the particle size on the amount of silica supports is shown in Figure 4.4.

Table 4.1 Sample composition and crystal structure of Co$_2$FeGa particles.

ID	Composition	a* (Å)	Particle size (nm)	Crystal structure
a	Co$_{0.52}$Fe$_{0.29}$Ga$_{0.19}$	5.723	66.4 ± 45.8	L2$_1$
b	Co$_{0.53}$Fe$_{0.29}$Ga$_{0.18}$	5.722	17.8 ± 9.3	L2$_1$
c	Co$_{0.55}$Fe$_{0.28}$Ga$_{0.17}$	5.717	Bimodal (34.7 ± 15.9 and 6.6 ± 1.8)	—

* calculated by applying Scherrer equation on the (220) reflections.
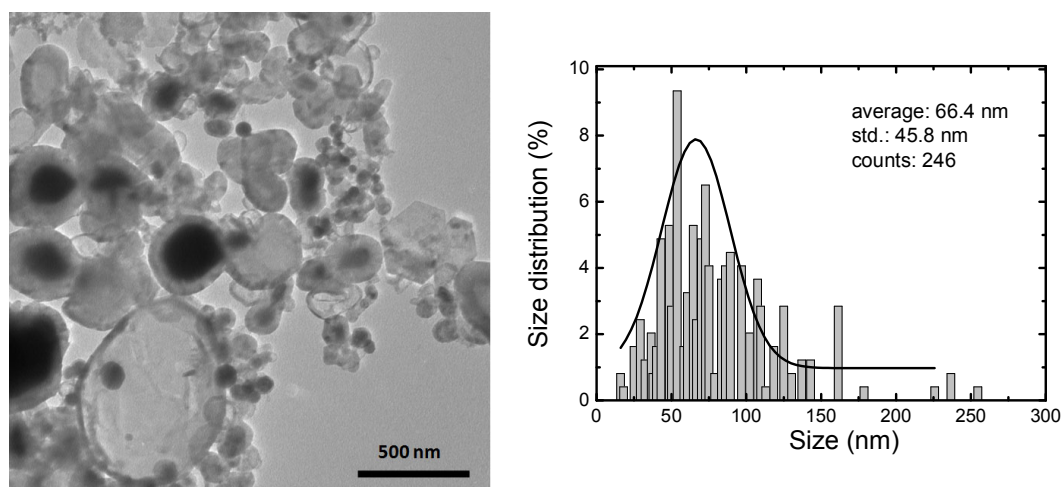
Figure 4.1 TEM micrograph and particle size distribution of sample **a**. The histogram is fitted with a Gaussian curve.
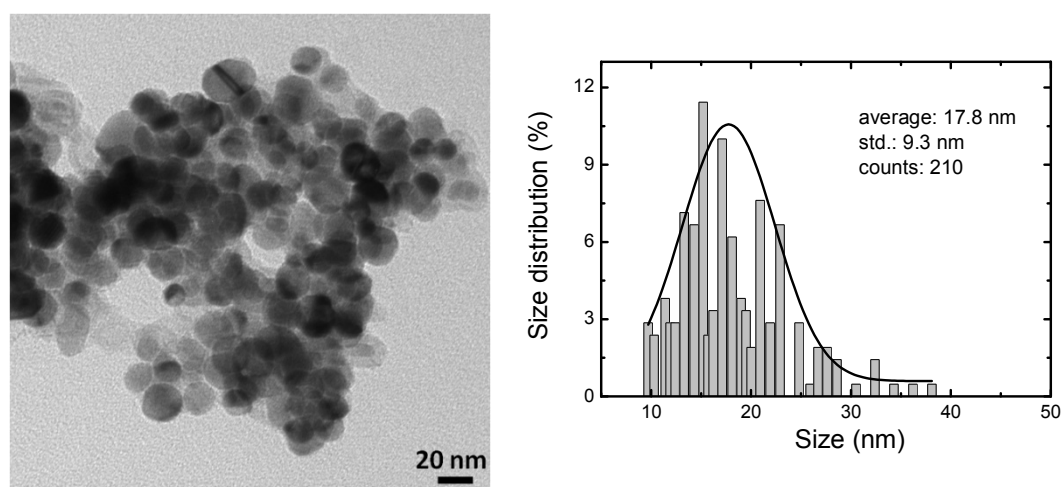
Figure 4.2 TEM micrograph and particle size distribution of sample **b**. The histogram is fitted with a Gaussian curve.
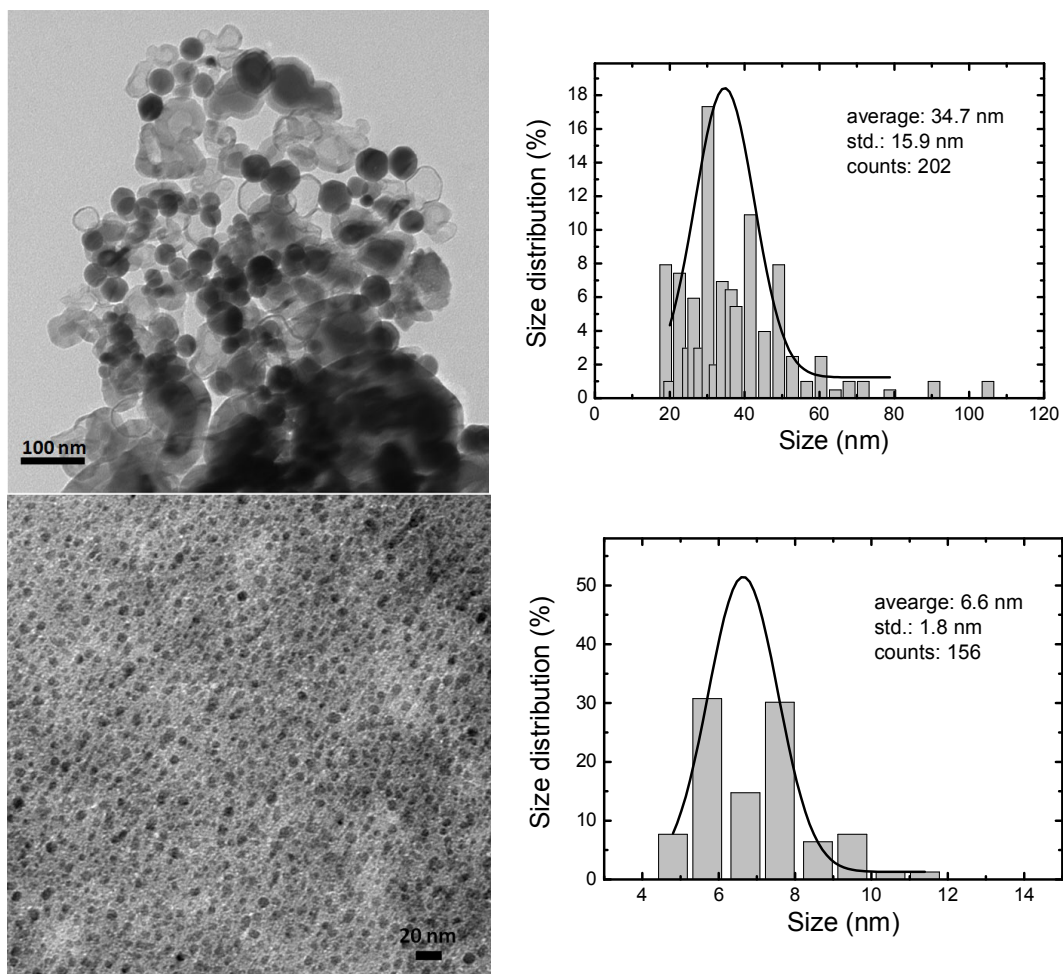
Figure 4.3 TEM micrographs and particle size distributions of sample **c**. The histograms are fitted with the Gaussian curves.
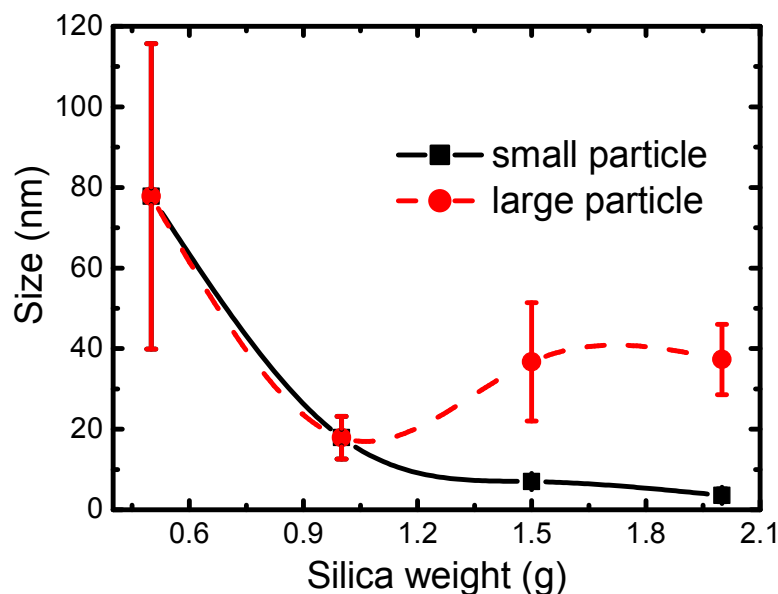
Figure 4.4 Size dependence of Co$_2$FeGa nanoparticles on the silica amount.

As shown in Figure 4.5 (a), a high resolution transmission electron microscope (HRTEM) probe on sample **c** reveals a single crystalline domain with a planar spacing of 0.203 nm that corresponds to the (220) planes. This confirms the high crystallinity of the particles. Carbon shells encapsulating the Co$_2$FeGa nanoparticles are observed in Figure 4.5 (b) that consist of 2 ~ 3 layers. The spacing of the carbon lattice fringes is 0.33 nm, which is close to the reported 0.341 nm of graphite (0001) planes [88–90]. Selected area energy-dispersive X-ray (EDX) data indicate a slight fluctuation of Co/Fe ratios centering at 2:1 and deficient Ga in the examined Co$_2$FeGa nanoparticles. This composition is comparable with that determined by the X-ray absorption spectra as described in Table 4.1. Scanning transmission electron microscope (STEM) and EDX were used to resolve the compositions of the individual nanoparticles by line scans through two adjacent nanoparticles, as shown in Figures 4.5 (c) and (d). It is noted that the iron content of the two probed particles varies drastically. The deviation of EDX-probed iron compositions of individual particles from the average composition might be attributed to the uneven distribution of metals within the particles at the nanoscale and/or the presence of metal impurities as revealed by XRD and discussed below.
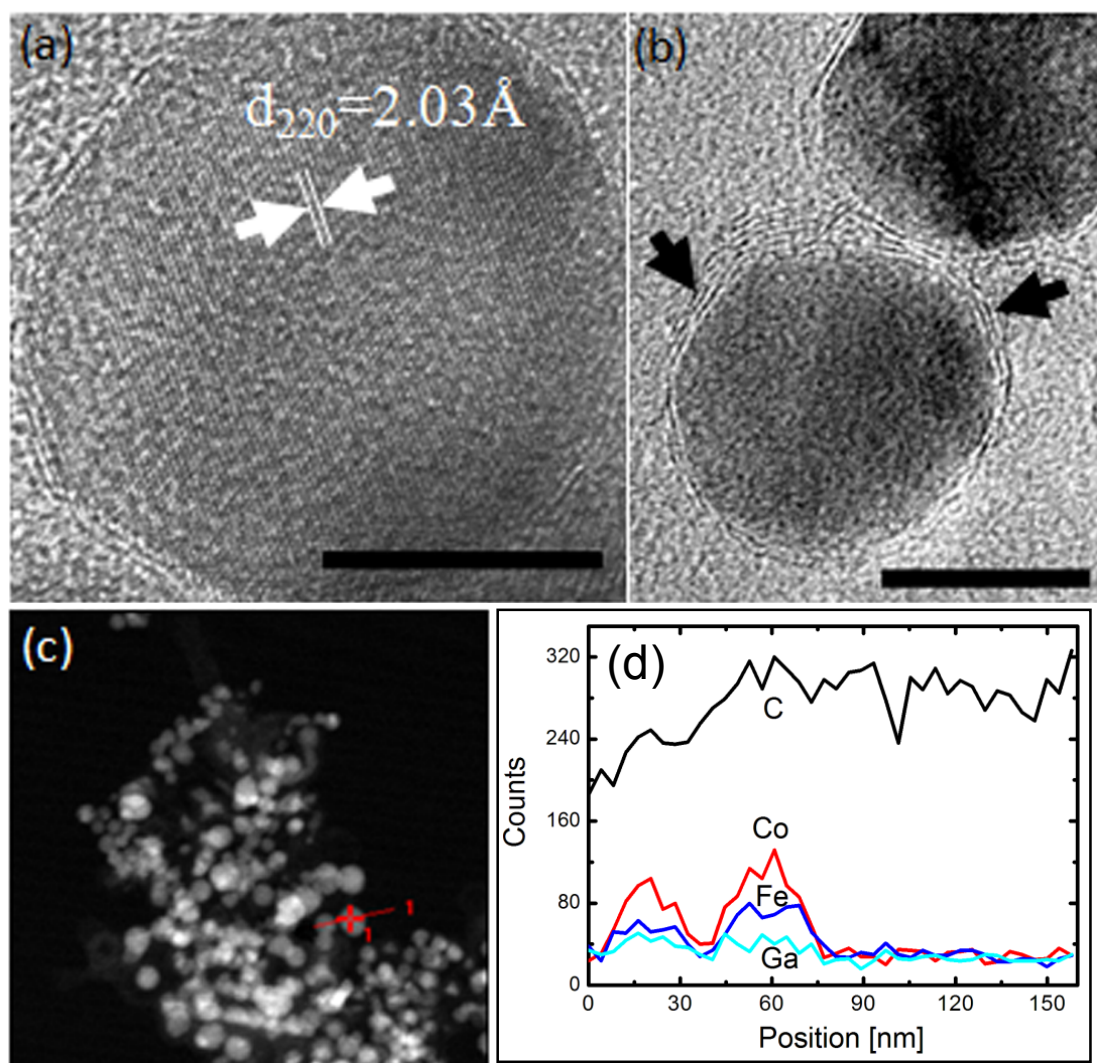
Figure 4.5 HRTEM (a-b), STEM micrographs (c) and EDX line profile (d) of Co₂FeGa nanoparticles (sample **c**). The arrows in (b) indicate the graphite layers at the particle surface. Scale bars are 10 nm.

4.2   Long range order structure

First, the crystal structure of the Co₂FeGa nanoparticle samples is examined by XRD using Mo K_α excitation. For samples **a** and **b**, the most intense (220) reflections belonging to $L2_1$ Co₂FeGa phase are resolved and the intensities of the (400), (422) and (440) reflections progressively decrease with decreasing particle size. The (111) and (200) reflections for $L2_1$ ordered Co₂FeGa are not detected. No resolvable diffraction reflection is observed for samples **c.** Figure 4.6 (a) shows the XRD patterns of Co₂FeGa nanoparticles of various particle sizes using synchrotron X-rays with a photon energy of 7.12 keV. By comparing the appearance and relative intensities of (111) and (200) reflections, various order types in Heusler compounds can be identified. Among the superlattice fingerprint (111) and (200)

reflections, only the (111) peaks are observed for samples **a** and **b** (see the inserts in Figure 4.6 (a)). Neither (111) nor (200) reflection is observed for sample **c** that might be due to the size-induced broadening.
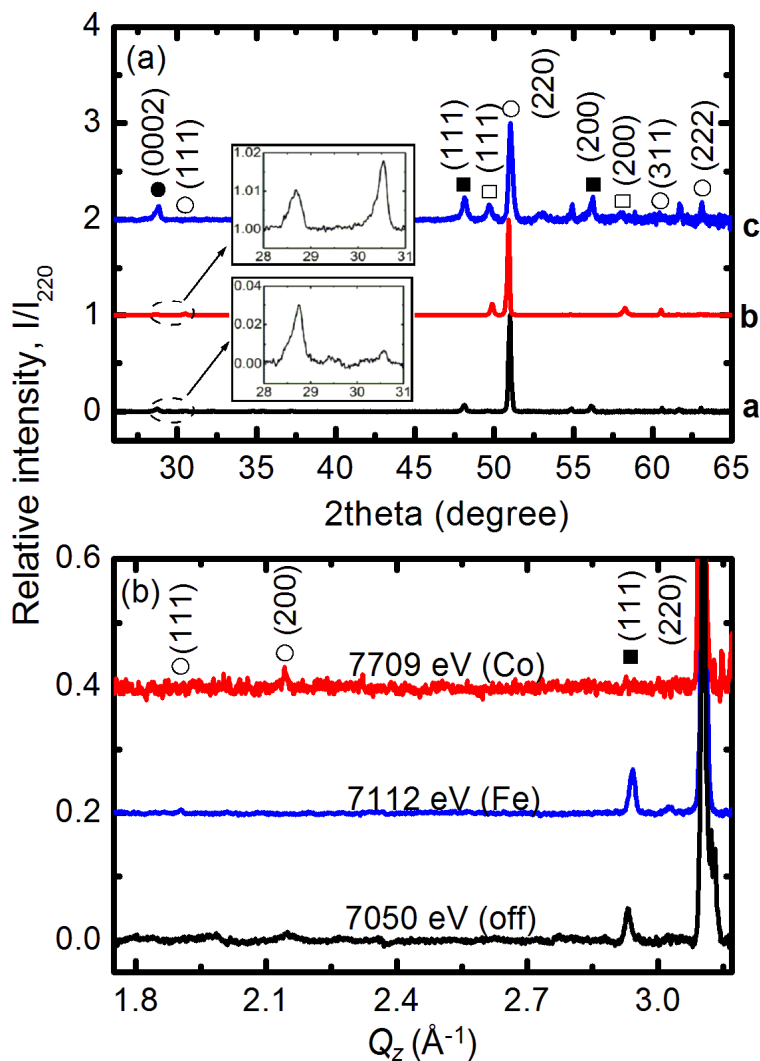
Figure 4.6 XRD patterns of Co$_2$FeGa nanoparticle samples **a** – **c**: (a) synchrotron radiation XRD patterns using a X-ray photon energy of 7.12 keV. Inserts in (a) show the zoom-in of 2theta range of 28 ~ 31°; (b) anomalous XRD patterns of sample **a** at photon energies close to Co and Fe K-edges and off-resonant energy of 7.05 keV (Off). Q$_z$ is the momentum transfer and is defined by Q$_z$ = 2π/d. d is the interplanar spacing. Symbols in (a): filled circle – graphite; circle – Co$_2$FeGa; filled square – Fe; square – Co.

To unambiguously identify the *L2₁* ordered structure, anomalous XRD and EXAFS are valuable tools as reported in previous work [27–29]. Anomalous XRD measurements were performed on sample **a** to verify the *L2₁* Heusler structure. Both (111) and (200) reflections were examined in terms of their energy dependences. This approach is slightly different from the reported approach for Co₂MnGe Heusler thin films where only the (111) reflection was examined [27]. In *L2₁* ordered Co₂FeGa, the structural scattering magnitude of the first three permitted Bragg reflections are: $F_{(111)} = 4|f_{Ga} - f_{Fe}|$, $F_{(200)} = 4|f_{Ga} + f_{Fe} - 2f_{Co}|$, and $F_{(220)} = 4|f_{Ga} + f_{Fe} + 2f_{Co}|$, where f_{Co}, f_{Fe}, and f_{Ga} are the atomic scattering factors of the constituent atoms. The magnitude of the atomic scattering factors is affected by the incident photon energy and it becomes small under the "resonant condition" when the photon energy approaches the absorption edges of the specific atoms. This enhances either the (111) or the (200) reflection when the X-ray energy comes close to the K edges of Fe or Co. As shown in Figure 4.6 (b), the intensity of (111) or (200) reflection is enhanced depending on the X-ray energy approaching to iron or cobalt K-edge. Under the off-resonant condition with a photon energy of 7.05 keV, neither reflection is enhanced. The lattice constants are calculated using (220) reflections (shown in Table 4.1) and were smaller than the reported value for bulk Co₂FeGa [64]. The (0002) reflections of hexagonal graphite are observed in all samples confirming the carbon coating. No diffraction peak belonging to either metallic carbide or silicate is observed. This is attributed to the protection from the graphite layers and the inertness of silica supports. Furthermore, fcc Fe and fcc Co impurities are observed in all samples.

4.3   Short range order structure

4.3.1 X-ray absorption near edge spectroscopy (XANES)

The XANES spectra of the metal foil, bulk Co₂FeGa, and Co₂FeGa nanoparticles at the Fe and Co K edges are shown in Figure 4.7. The edge positions are determined from the first maximum of the first derivative spectra. Compared to edge positions of the standard metal foil, the absorption edges of the bulk and nano-sized Co₂FeGa exhibit some positive energy shifts. The Fe K-edge shifts for the bulk Co₂FeGa and samples **a** – **c** are 0.548 eV, 0.548 eV, and 0.893 eV, respectively. For Co K-edge, the corresponding edge shifts are 0.890 eV, 0.890 eV, and 0.594 eV, respectively. For the K edges of transition metals, typical amplitude of the energy shift for each increase in the oxidation by one valence unit is approximately 2 ~ 3 eV. This indicates that all iron and cobalt species exist in zero-valence state within experimental error and the formation of iron or cobalt oxides is excluded.

As described in Figure 4.7 (a), the local atomic environment of iron in the bulk Co₂FeGa distinguishes itself with the "white line" at 7131.1 eV (A), followed by a platform ranging from 7135.6 eV to 7142.3 eV and a broadened hump centering at 7151.4 eV (C). The XANES spectra of the samples exhibit similar peak patterns within the first 40 eV above the edge, which is evidence for the formation of intermetallic compound in the Co₂FeGa nanoparticles. Furthermore, the characteristic resonances of metallic iron at 7142.1 eV (B) and 7154.4 eV (D) are not observed for all samples. This further supports the above argument. The scenario is similar at Co K-edge as displayed in Figure 4.7 (b). The spectroscopic feature of Co in bulk Co₂FeGa can be described by the "white line" at 7728.0 eV (E), and two resonance peaks at 7737.9 eV (G) and 7749.2 eV (H). Samples **a** - **c** display similar characteristics with those of bulk Co₂FeGa even though the G and H resonances damp in intensity and also shift to higher photon energy. Again, the absence of characteristic resonances associating with metallic cobalt at 7735.4 eV (F) and 7759.7 eV (I) confirms the formation of intermetallic compound.
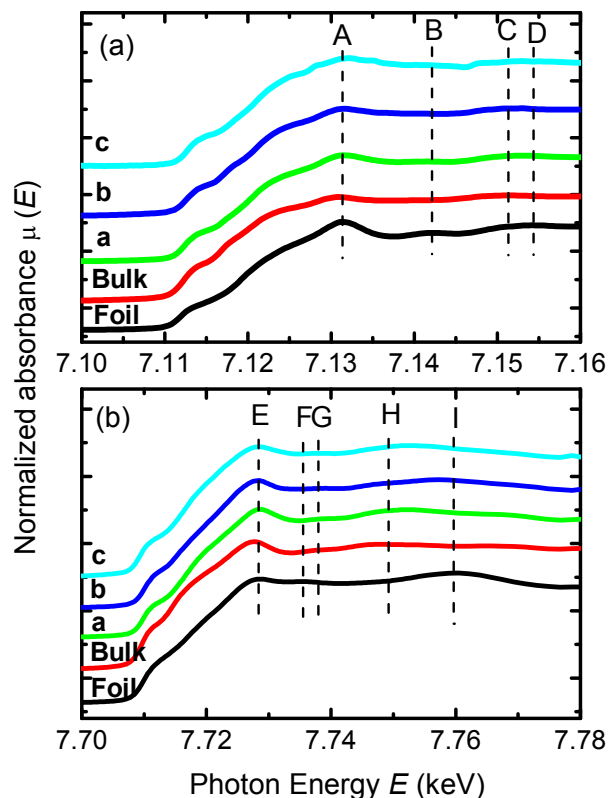
Figure 4.7 XANES spectra of the metal foil, bulk Co$_2$FeGa and Co$_2$FeGa nanoparticles **a – c** at the absorption K edges of Fe (a) and Co (b). The vertical lines are guides to the eye.

4.3.2 Extended X-ray absorption fine structure (EXAFS)

The EXAFS fits were first performed assuming that Co$_2$FeGa phases were ordered in the perfect $L2_1$ structure. An experimentally derived a = 5.737 Å was used for calculating the scattering paths. Only the single scattering (SS) paths with significant contributions in the R-range of 1.0 ~ 5.0 Å were considered in the fits. As displayed in Figures 4.8, for all the samples, at both edges, the oscillation frequencies resemble that for bcc Fe demonstrating characteristic cubic environments. The amplitude of the oscillations of the nanoparticles progressively reduces with decreasing particle size (in the order of **a** to **c**). Figures 4.9 show the Fourier transforms (FT) at Fe and Co edges of the bulk and Co$_2$FeGa nanoparticles. All spectra exhibit two well-defined peaks (uncorrected for the phase shift) at around 2.2 Å (denoted as "A") and 4.5 Å (denoted as "B"). Peak A reflects contributions from the first two coordination shells. As summarized in Table 4.2, compared to the bulk Co$_2$FeGa, a shortening (up to 5 %) of bond distances of the peak A is observed for all Co$_2$FeGa nanoparticles. The extent of negative shift in R space increases with decreasing particle size: 2.209 Å for **a,** 2.178 Å for **b**, and 2.148 Å for **c**, respectively. Weaker FT magnitudes in **c** signify increasing atomic disorder. At Co K-edge, the magnitude of the first peak also decreases with decreasing particle size, even though the particle size-induced changes are not as pronounced as for Fe K-edge.
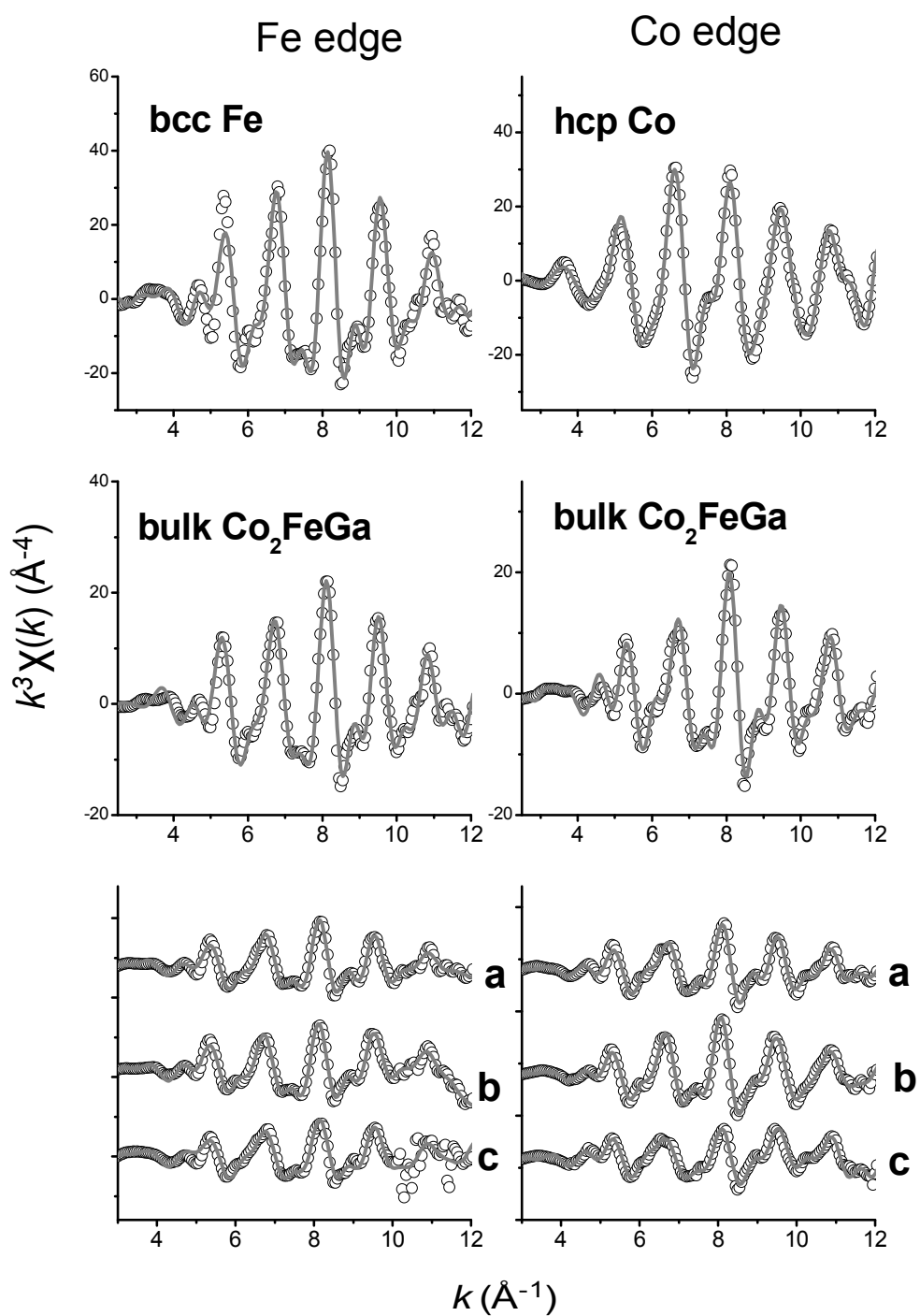
Figure 4.8 The k^3-weighted EXAFS $\chi(k)$ spectra of the metal foils, bulk Co₂FeGa, and Co₂FeGa nanoparticles at Fe and Co K-edges from experiments (symbol) and fits (—).
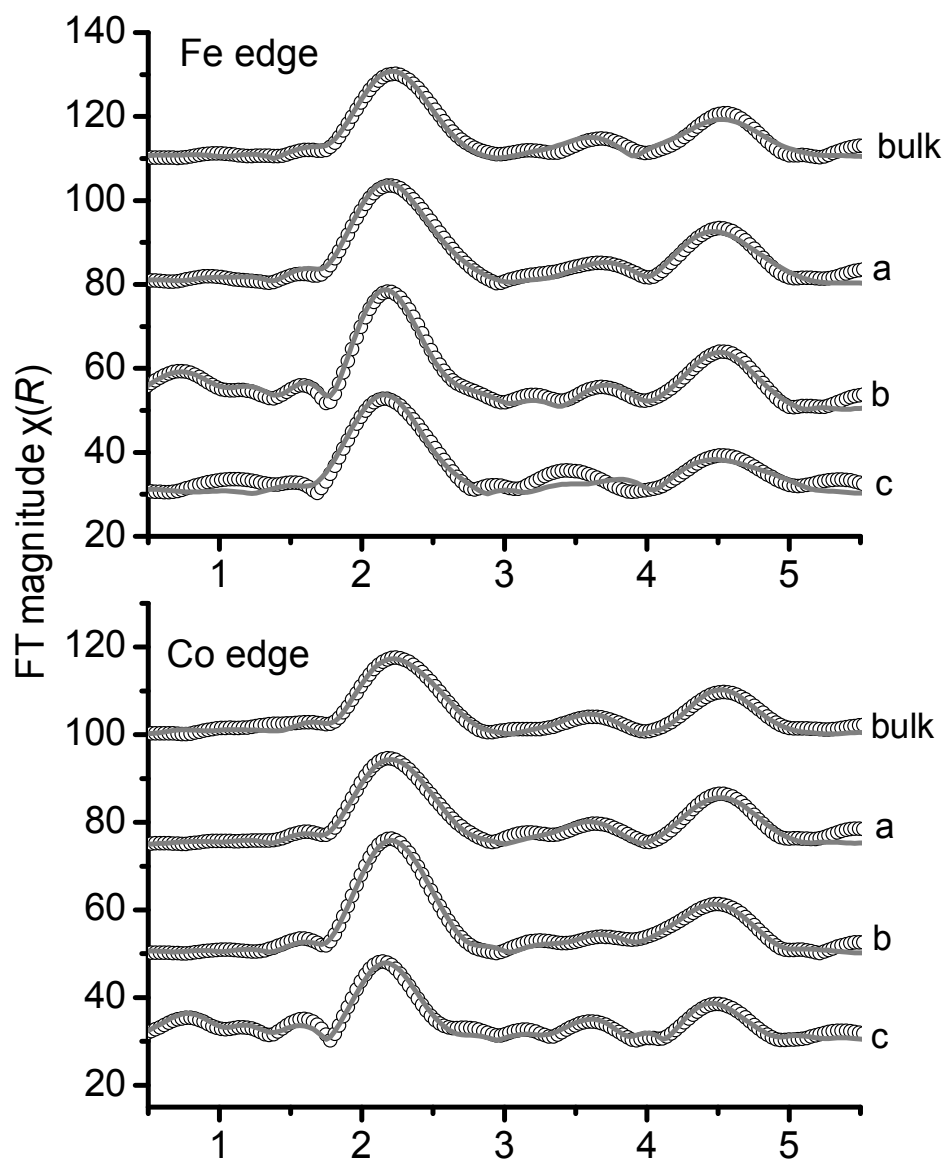
Figure 4.9 Magnitudes of Fourier transforms of $k^3\chi(k)$ spectra of bulk Co$_2$FeGa and Co$_2$FeGa nanoparticles at the K-edges of Fe and Co from experiments (symbol) and fits (—).

Table 4.2 Amplitudes and peak positions of the peak A for samples **a** − **c** and bulk Co$_2$FeGa from EXAFS data in R space.

ID	Amplitude		Position	
	Fe	**Co**	**Fe**	**Co**
a	23.2	19.1	2.2089	2.1783
b	28.1	25.7	2.1783	2.2089
c	22.7	16.8	2.1476	2.1476
Bulk	19.5	17.0	2.2396	2.2396

Compared to the FT magnitude of the samples at two edges, it is noted that larger FT magnitudes are consistently observed at Fe edge than at Co edge. This indicates that some cobalt might be involved in a phase which does not significantly contributes to the overall backscattering. This is consistent with the observed Co impurity phases as revealed by XRD in the samples. If all iron and cobalt were present in the $L2_1$ ordered Co$_2$FeGa phase, the FT magnitudes at both edges should be the same given the practically identical backscattering factors of Fe and Co.

At Fe and Co K-edges, the *R*-factors at both edges are 0.006 ~ 0.012 for samples **a** and **b** and 0.03 ~ 0.07 for samples **c** indicating that the short range order of samples **a** and **b** are better described by the $L2_1$ ordered model. The obtained values for the passive electron reduction factor (S_0^2) are between 0.9 and 1.1. For samples **a** and **b,** the Debye-Waller factor (σ^2) values for the different paths are also small (0.005 ~ 0.014). The shifts in E_0 are in the range of 0 ~ 9 eV. The fitting quality of samples **c** using the $L2_1$ ordered model is relatively poor.

To determine the order type of Heusler compounds is closely related to examine the short-range disorder, which is well probed by EXAFS technique [73]. Additional EXAFS fits were carried out on samples **a** and **c** using *B2* and *A2* disordered structure models. For sample **a**, the fitting quality are comparable at Fe edge using different structure models. However, there is a significant difference at Co edge and it seems that the $L2_1$ model fits better than the *B2* and *A2* models. In comparison, at both edges, the fits between sample **c** and the tested models are not satisfactory. As a result the structure type of sample **c** cannot be clarified. Increasing amount of the impurity phase in this sample might degrade the applicability of EXAFS analysis.

Besides the SS paths in the R-range of 1.0 ~ 5.0 Å, one collinear multiple (MS) path along the body diagonal of the primitive cubic cell is also important and should be included for EXAFS fits. The Fe K-edge EXAFS fits of sample **a** shown in Figure 4.10 reflects the improvement in fitting quality when the MS path is additionally included. From the first look the R factors of the two fits are comparable and there is only minor improvement in the second FT magnitude peak B. The imaginary component plots reveal, however, a significant improvement in the fitting quality. As such, the fitting strategy should be optimized by including important SS and the MS path in EXAFS fits.
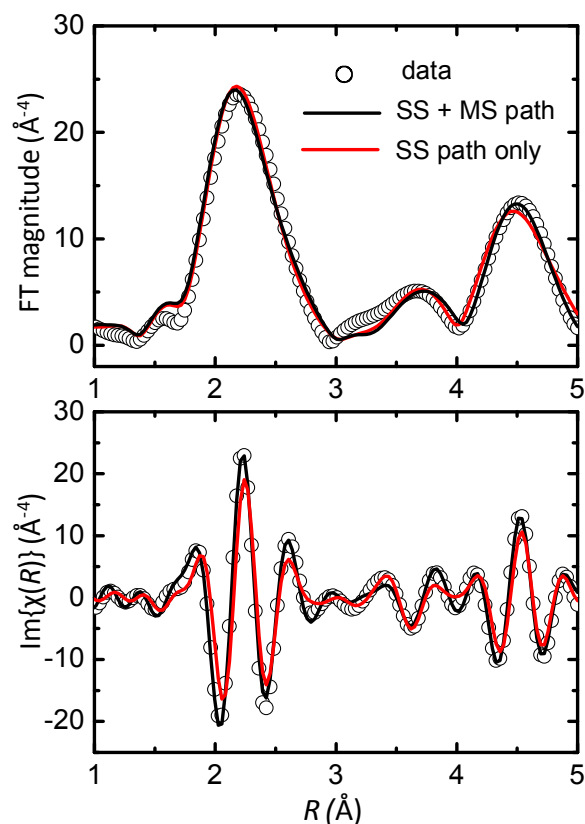
Figure 4.10 Magnitudes and imaginary components of Fourier transforms of Fe K-edge EXAFS spectra of sample **a** fitted by SS paths and SS plus MS path. The fits to the data are shown as solid lines.

Furthermore, in a perfect $L2_1$ structure, the first coordination shell surrounding the X (Co) site is composed of four Y (Fe) sites and four Z (Ga) sites at exactly equal distances from X atoms. The difference in the Co–Fe and Co–Ga bond lengths directly points to short range disorder in the $L2_1$ structure. The Co K-edge EXAFS fits were additionally carried out in the R-range of 1.0 ~ 3.0 Å and on the first coordination shell of Co₂FeGa nanoparticles. As shown in Figure 4.11, an excellent agreement between the data and $L2_1$ model is reached for sample **a** in the R-range of 1.0 ~ 3.0 Å. The R-factor is ~ 0.006. The derived Co–Fe and Co–Ga bond lengths from the first coordination shell are 2.43 Å and 2.46 Å, reflecting high degree of $L2_1$ ordering in this sample. It is noted that both bond lengths are slightly shorter than the theoretically predicted 2.484 Å. This observation might originate from the nonstoichiometry induced site disorder. Due to Ga deficiency, excess Co or Fe atoms might occupy the Ga sites (denoted as Z–Co or Z–Fe). The obtained Co-Fe bond is actually the weighted average distance of Co from the conventional Y–Fe and anomalous Z–Fe. This results in the discrepancy in the Co–Fe bond length. Similar explanations might be applicable for Co–Ga bond lengths as well.
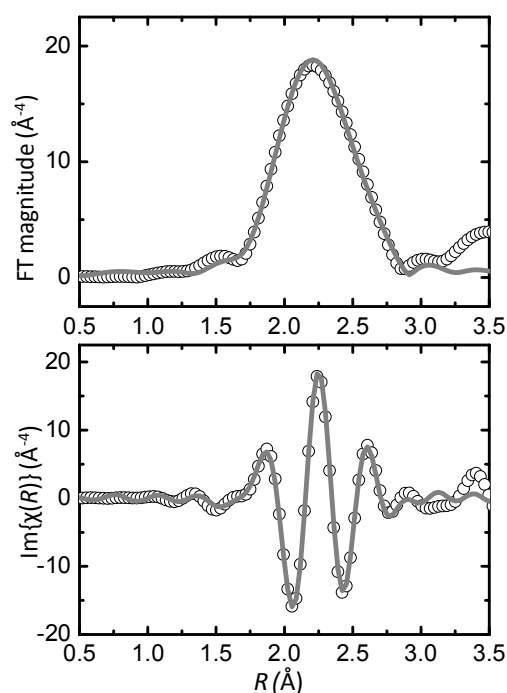
Figure 4.11 Magnitudes and imaginary components of Fourier transforms of Co K-edge EXAFS spectra of sample **a** in the R-range of 1.0 ~ 3.0 Å. The fits to the data are shown as solid lines.

4.4   Size dependent magnetic properties.

The size dependent magneto-structural correlations in Co$_2$FeGa nanoparticles were investigated by Mössbauer spectroscopy and SQUID magnetometer. The magnetic properties of Co$_2$FeGa nanoparticles are summarized in Table 4.3. The Mössbauer spectra of samples **a** ~ **c** were measured at room temperatures and the results are shown in Figure 4.12. For samples **a** and **c**, a distribution fit model is absolutely necessary which corresponds properly to the size distribution feature of these samples. Sample **b** exhibits a relatively narrow size distribution and even conventional Lorentzian profile model could be applied. All spectra were fitted by one magnetic sextet and one superparamagnetic doublet. The observed isomer shifts and hyperfine magnetic fields are close to those reported for bulk Co$_2$FeGa [80] confirming the formation of Heusler Co$_2$FeGa phase. The doublet/sextet ratio steadily increases from samples **a** to sample **c** spanning both the single and bimodal size domains.

Table 4.3 Magnetic properties of Co$_2$FeGa nanoparticles at room temperature.

ID	NP/silica ratio	Ms* (μ_B/f. u.)	H$_c$* (Oe)	Br* (emu/g)	H$_{hff}$ (kOe)	IS (mm/s)	Doublet (V.%)	Sextet (V.%)	K (J/m^3)
a	0.196	4.87	40	2.25	319.0	0.052	17.8	82.2	193
b	0.125	4.97	38.8	1.28	319.4	0.062	18.7	81.3	15900
c	0.072	4.82	302	14.6	318.9	0.055	27.7	72.3	4800

* measured at 5 K.
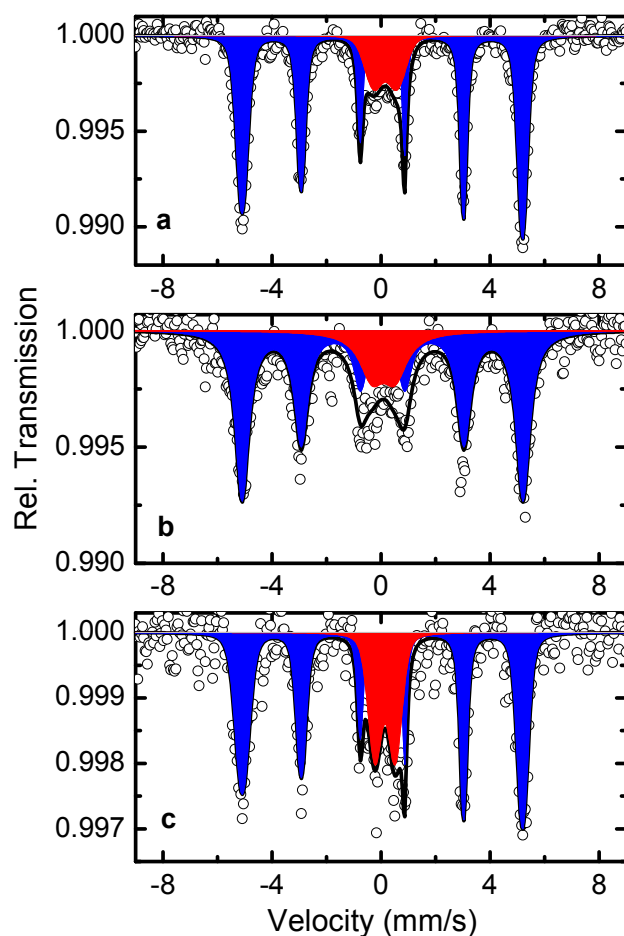
Figure 4.12 Mössbauer spectra of Co₂FeGa nanoparticles of various sizes at room temperature: (a) sample **a**; (b) sample **b**; (c) sample **c**. Superparamagnetic doublets and static magnetic sextets are shadowed by red and blue.

A straightforward way to estimate the superparamagnetic size limit is not available for magnetic nanoparticles with a relatively broad size distribution. In this work an alternative way is proposed to pinpoint the critical size by relating the TEM-derived particle size and the Mössbauer spectroscopy data. This is examplarily shown for sample **b** in Figure 4.13. First the normal particle size distribution data (see Figure 4.13 (a)) is converted to the volume percentage as a function of particle size. The size-volume fraction histogram is then fitted with a Gaussian model as shown in Figure 4.13 (b). The integrated area below the Gaussian curve corresponds to the summation of both the large and small nanoparticles. Taking into account of the fractions corresponding to the doublet (18.7%) and sextet (81.3%) subspectra, Zones D and S are identified in Figure 4.13 (c). They correspond to the abundance of particles under superparamagnetic and statically magnetic states, separately. The particle size determined by the boundary (identified by an arrow in Figure 4.13 (c)) between the two zones is the superparamagnetic critical size and is found to be ~ 17 nm. This value is reasonable compared to a reported critical size of ~ 20 nm for $Fe_{0.4}Co_{0.6}$ nanoparticles [73].
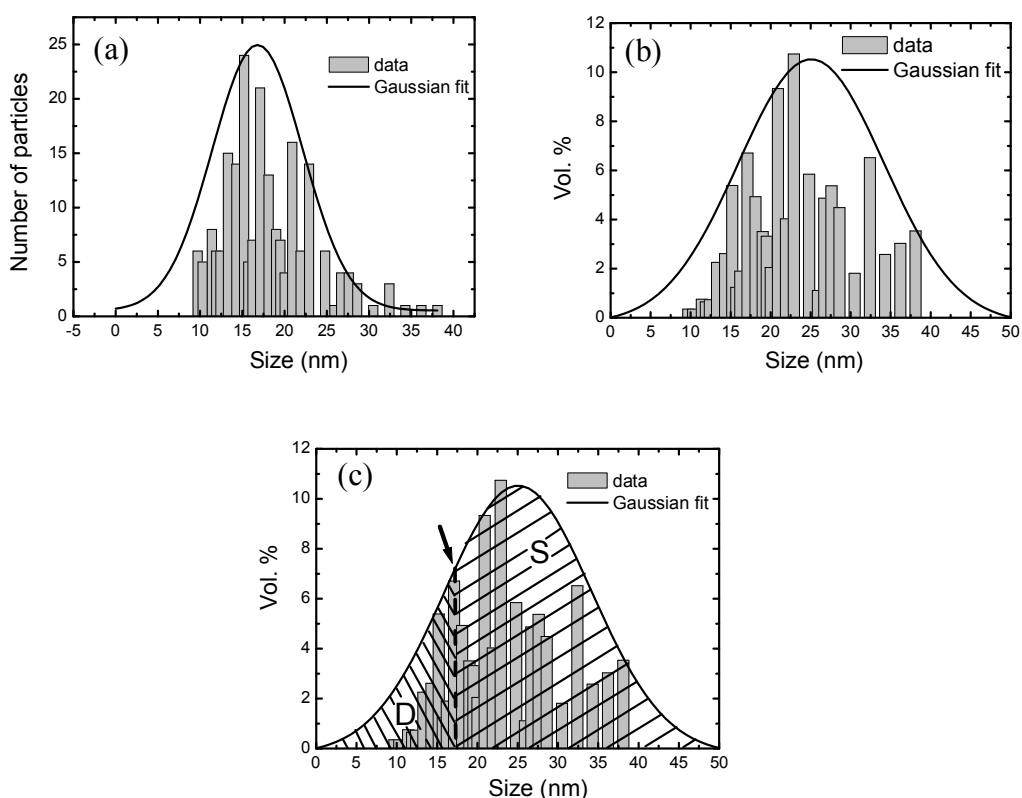
Figure 4.13 An illustration to determine the superparamagnetic critical size of Co$_2$FeGa nanoparticles: (a) particle size distribution; (b) volume fraction of the particles as a function of size; (c) determining the critical size by correlating to the volume fractions of the doublet and sextet. The arrow in (c) assigns the critical size of Co$_2$FeGa nanoparticles corresponding to the boundary between the doublet (D) and the sextet(S) zones.

The magnetic behavior of Co$_2$FeGa nanoparticles was investigated by field and temperature dependent magnetometry. The magnetization curve of sample **a** at 5 K and 300 K are shown in Figure 4.14 (a). As shown in Table 4.3, samples **a** and **b** demonstrate similar magnetization characteristics and are magnetically soft. The measured saturation magnetic moment at 5 K of the samples are in the range of 110 ~ 114 emu/g (4.87 ~ 4.97 μ_B), which are slightly lower than the reported value for bulk Co$_2$FeGa (117.7 emu/g or 5.13 μ_B) at 4.2 K [64]. For stoichiometric Co$_2$FeGa, according to the Slater–Pauling rule, the spin magnetic moment per unit cell value is 5 μ_B/f.u. Therefore, the measured saturation magnetizations of Co$_2$FeGa nanoparticles are slightly low compared to the Slater–Pauling value. As described in Table 4.1, all samples are nonstoichiometric with Ga deficiency.

Antisite disorders are present even in stoichiometric pure Heusler compounds such as Co$_2$MnSi [28]. The nonstoichiometry induced antisite disorders in Co$_2$YZ (e.g. Y = Mn; Z = Si, Ge) have been investigated both theoretically [91,92] and experimentally [18]. Due to the lack of theoretical data on the antisite disorder in Co-Fe-Ga system, the formula unit model proposed by Yamamoto et al. [18] for Co$_2$MnSi(Ge) system were adapted for sample **b**. The obtained formula unit model is Co$_2$[Fe$_{0.867}$Co$_{0.133}$][Ga$_{0.705}$Fe$_{0.295}$]. The correctness of the formula antisite model was examined by comparing the experimental μ_s with that predicted by the Slater–Pauling rule. The measured μ_s of 4.97 μ_B /f.u., is much smaller than the

Slater–Pauling rule predicted 6.6 μ_B/f.u. This indicates the antisite disorder by the proposed model might be overestimated for sample **b** or the antisite model is incorrect.

For stoichiometric Co$_2$FeGa compounds, the smaller difference in atomic radii between Co (1.35 Å) and Fe (1.40 Å) might lead to a smaller energy change when atomic disorder takes place between X and Y sites and therefore site disorder (e.g. *DO$_3$*) occurs more easily. Theoretical calculations on Co$_2$YZ compounds predict that site interchange between the Y atom and Co atom does not strongly affect the measured magnetic moment since the major magnetic moment carriers are Y and Co atoms [91,92].

It is assumed that the discussed formula unit antisite model is only applicable for Heusler compounds of single phase. The presence of impurity phase renders uncertainty in determining the actual composition of the formed Co$_2$FeGa phase and undermines the accuracy of the proposed antisite disorder models. For Co$_2$FeGa nanoparticles investigated in this work, the presence of impurity phases has been revealed by XRD data. On the other hand, the closeness of the measured magnetizations with the Slater–Pauling value might provide a hint that stoichiometric Co$_2$FeGa phase was formed under non-stoichiometric conditions.

The correlations between the particle size and the magnetic moment of nanoparticles have been well established and the saturation magnetization normally decreases with decreasing particle size [93,94]. For Co$_2$FeGa nanoparticles, a bimodal particle distribution develops, the average particle size decreases and the population of superparamagnetic nanoparticles increases. In this regard, the magnetization data are inconsistent with the decreasing rule of magnetization. At 5 K, the coercivities for samples **a** and **b** are close to 40 Oe. Sample **c** are also magnetically soft but with a larger coercivity (302 Oe).

Temperature dependent SQUID measurements were utilized to verify the superparamagnetic behavior of the smaller Co$_2$FeGa nanoparticles. Field cooled (FC) and zero field cooled (ZFC) magnetization curves were measured for sample **a** in a temperature range of 5 ~ 300 K under a magnetic field of 0.01 T. As shown in Figure 4.14 (b), the blocking of sample **a** spread over a wide temperature range signifying a rather wide size distribution of particles. The magnetic susceptibility reaches maximum at around 35.4 K (the nominal blocking temperature) corresponding to the contribution from the smallest particles in the sample. Temperature dependent Mössbauer spectroscopy of sample **a** was measured in a temperature range of 80 ~ 275 K. All spectra are fitted with one doublet and one magnetic sextet and the fraction of the doublet decreases monotonously with decreasing temperature: 17.8% at 295 K, 13.4% at 275 K, 11.5% at 200 K, and 9.7% at 80 K, respectively. No sharp blocking temperature is observed and a "blocking" process overspreads a wide temperature range. This fact also corresponds to a broad size distribution of of this sample. The Mössbauer blocking temperature is defined as the temperature at which the fraction of the static component equals that of the superparamagnetic component. One can conclude that the Mössbauer blocking temperature of this sample should be well above room temperature. The blocking temperature determined from SQUID measurement is lower than that determined from Mössbauer measurement. It could be explained by the different characteristic observation times of Mössbauer experiment (~ 10^{-8} s) and static magnetization measurements (~ 100 s).
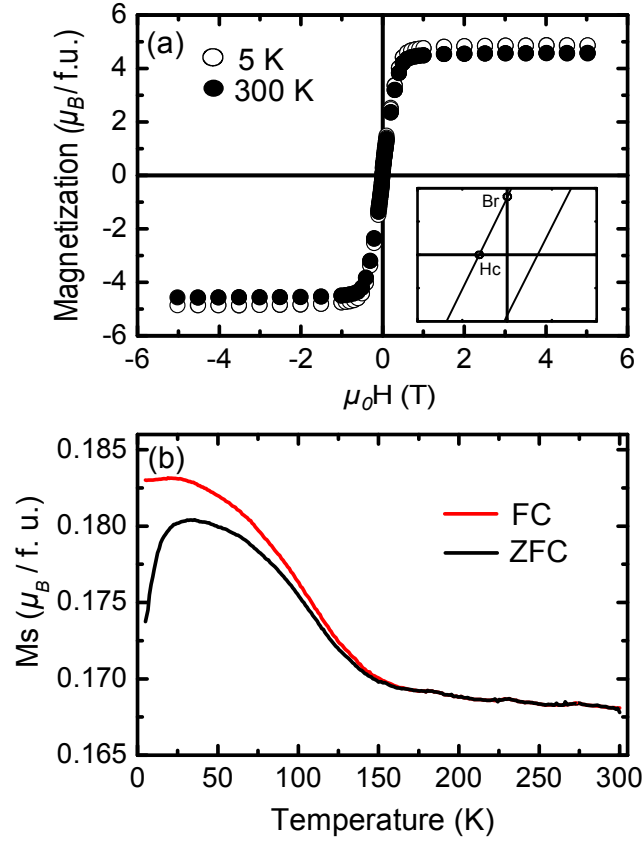
Figure 4.14 Magnetic properties of sample **a**: (a) magnetization curves at 5 K and 300 K; (b) temperature dependent FC-ZFC curves. The insert in (a) shows the hysteresis curves close to the origin at an enlarged scale.

The magnetic anisotropy of Co$_2$FeGa Heusler compound has not been extensively investigated. In this work, the effective anisotropy constant K for Co$_2$FeGa were calculated for the present samples. As predicted by the Néel-Arrhenius equation [95], under superparamagnetic state, anisotropy constant K can be calculated.

$$K = \frac{k_B T ln(\tau_m/\tau_0)}{V} \qquad (3)$$

Here, k_B is the Boltzmann constant, T is the blocking temperature, V is the particle volume. τ_m and τ_0 are the measured relaxation time and the relaxation constant taking the values of 10^{-8} s and 10^{-13} s, as reported in the literature [79]. In the calculations, the estimated blocking temperatures for samples **a** ~ **c** are taken as 300 K. The calculated effective anisotropy constants for samples **a** ~ **c** are listed in Table 9. The values for samples **b** and **c** are of same order in magnitude compared with the reported uniaxial anisotropy (K_u, 0.63 X 10^4 J/m^3) of Co$_2$FeSi Heusler thin films [43,96,97].

The role of carbon coating in the chemical synthesis of Co$_2$FeGa nanoparticles is found to prevent Co$_2$FeGa nanoparticles from oxidation. This is evidenced by the XRD data in Figure 4.6 (a) that indicates the absence of metal oxides in the final products. The surface

immobilized carbon layers, however, are considered to decrease the spin polarization at the Fermi level and suppress the magnetization properties of the encapsulated magnetic nanoparticles [98,99]. In a control experiment, the saturation magnetization of two samples (one with 5 min CH$_4$ CVD at 250 ml/min and the other one is non-coated, with other sampling conditions to be identical) were compared. As shown in Figure 4.15, the magnetic moment at 5 K decreases from 4.98 μ_B to 4.76 μ_B (a reduction of 4.4%) in the presence of carbon layers. This observation is consistent with the reports in the literature [98,99].
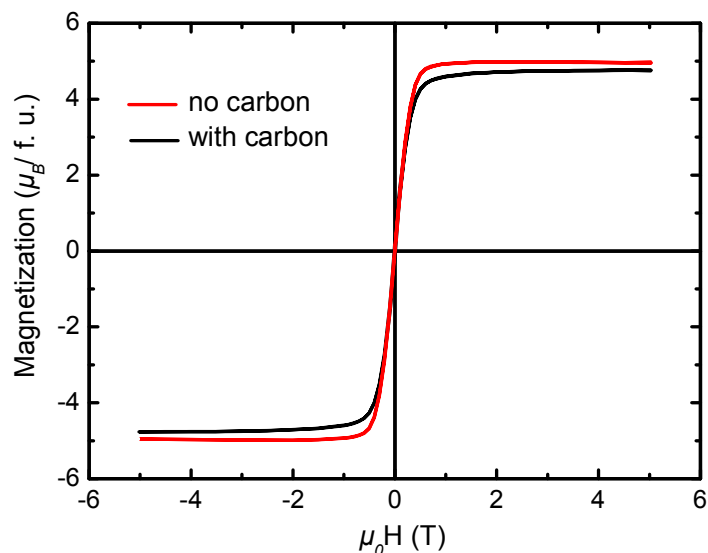
Figure 4.15 Magnetization curves of sample **b** under conditions with and without carbon coating at 5 K.

4.5 Summary

In summary, the size of Co$_2$FeGa nanoparticles can be tuned by adjusting the amount of silica supports. The formation of *L2$_1$* Co$_2$FeGa phase in the nanocomposite particles is confirmed by anomalous XRD, Mössbauer spectroscopy and magnetic measurements. EXAFS technique has been demonstrated to be a suitable method to identify the crystal structure of Co$_2$FeGa Heusler nanoparticles. It is found that the degrees of both long and short range order of Co$_2$FeGa Heusler nanoparticles decrease for smaller Co$_2$FeGa nanoparticles. The coupling of the TEM-derived particle size and Mössbauer spectroscopy specifies the critical size of Co$_2$FeGa nanoparticles bridging superparamagnetism and ferromagnetism.

5   Fe₂CoGa Heusler nanoparticles

By using the same chemical approach as for Co₂FeGa nanoparticles and only varying the precursor compositions, a series of silica supported Co₃₋ₓFeₓGa (x = 0 ~ 2) Heusler nanoparticles has been prepared and characterized. Among them, two end members at x = 1 and x = 2 are interesting. Co₂FeGa compounds are potential electrode materials for spintronics. The chemical preparation, structure, and magnetic properties of Co₂FeGa nanoparticles have been discussed in previous chapters. In comparison, Fe₂CoGa compounds appear as a new candidate for ferromagnetic shape memory alloys (FSMA). In this chapter, experimental results on the structure and magnetic properties of Fe₂CoGa Heusler nanoparticles are presented.

5.1   Introduction

Magnetic induced shape memory effects have been observed in selected Heusler compounds. Compared to the temperature-driven shape memory alloy such as TiNi, magnetic manipulation of martensitic phase transformation is fast and efficient. A typical example of magnetically controlled shape memory alloys (MSMA) is Ni₂MnZ (Z = Ga, Sn, In) [100]. Large magnetically induced strains have been reported in Ni₂MnZ Heusler compounds. The disadvantages such as low martensitic phase transition temperature, poor room temperature ductility, and high costs of elements justify searching of new candidates in an ever expanding Heusler compound family. In this light, new Heusler compounds might be attractive [101, 102] due to their similarity to the known Ni₂MnGa.

Theoretical calculations reveal a rather high magnetic moment (5.49 ~ 6.14 μ_B) for Fe₂CoGa [102]. Theoretical calculations predicted a Curie temperature higher than 1540 K and a martensitic phase transition temperature of 563 K for the tetragonal distortion of *L2₁* ordered Fe₂CoGa [103]. Jaggi et al. investigated the long and short range order of bulk Fe₂CoGa [80] and they found that Fe₂CoGa compounds are ordered in a CuHg₂Ti-type (*X*) structure and exhibit a Curie temperature as high as 1165 K. This observation is consistent with the work by Burch et al. [104] who stated that, in Fe₃₋ₓTₓSi (T = transition metals) system, *X*-type or inverse Heusler structures are frequently observed in Heusler compounds with T atoms are beneath or right to Fe in the periodic table. Since Co locates to the right of Fe in the periodic table, Co atoms in Fe₂CoGa compounds preferentially occupy half of the Fe sites (4c). As a result, Fe atoms go to 4a and 4d sites and Ga atoms at 4b sites. Gilleβen et al. carried out first-principles computations on 810 full Heusler compounds and found that inverse Heusler structure of Fe₂CoGa is thermodynamically more stable than the Heusler structure [105]. In parallel, Dannenberg et al. investigated the structural and electronic properties of the conventional (*L2₁*) and inverse Heusler (*X*) structure of Fe₂CoGa [106]. They found that *X*-type Fe₂CoGa compounds do not exhibit a martensitic transformation while those of *L2₁* structure might exhibit martensitic transformation at high temperature. The magnetic moments of *L2₁* and *X* ordered Fe₂CoGa were calculated as 6.15 μ_B and 5.36 μ_B, respectively. The expected high martensitic phase transition temperature coupled with high Curie temperature of *L2₁* ordered Fe₂CoGa compounds make them a promising candidate for ferromagnetic shape memory applications. They also proposed substitution of Ga by Zn in ternary Fe₂CoGa and expected that optimized magnetic and electronic properties are found in the quaternary Fe₂CoGaₓZn₁₋ₓ system. On the other hand, it has been theoretically argued that the calculated martensitic transformation temperature based on tetragonal distortion of *L2₁* ordered Fe₂CoGa is higher than the Curie temperature and is not suitable for MSMA applications [101]. Fe₂CoGa compounds deserve further theoretical and experimental investigations to understand the phase transition and magnetic properties.

5.2   Long range order structure

The sample M08 has a composition of Co$_{0.23}$Fe$_{0.53}$Ga$_{0.24}$ with excess Fe. The lattice constant is 5.7678(1) Å. The XRD patterns of sample M08 and theoretical $L2_1$ and X ordered Fe$_2$CoGa are shown in Figure 5.1. Besides the typical cubic reflections of (220), (400), (422), (440), (620), (444), and (642) for Fe$_2$CoGa, the (311) reflection is also observed in M08. The (111) and (200) reflections, however, are not observed (see inserts in Figure 5.1). The absence of the characteristic (111) and (200) reflections might be due to high X-ray energy, low intensity of the reflections, and close approximation and even overlapping with the graphite (0002) reflection. Therefore, XRD measurement using X-rays of a wavelength of 1.7414 Å was carried out. As summarized in Table 5.1, the presence of the (111) reflection is resolved and the (200) reflection is still not observed. As shown in Figure 5.1, $L2_1$ and X ordered Fe$_2$CoGa could be differentiated by comparing the relative intensity of the (111)/(200) and (311)/(222) reflections. The $I_{(111)}/I_{(200)}$ ratios are 3:4 and 3:1 for $L2_1$ and X structures, respectively. In comparison, the $I_{(311)}/I_{(222)}$ ratios are 3:2 and 5:1. As such, the presence of the (111) and (311) peaks and the absence of the (200) and (222) peaks provide evidence of formation of X-type Fe$_2$CoGa. For bulk Heusler alloys, the X-type structure is normally found in Heusler compounds if the nuclear charge of the Y element is larger than that of the X element from the same period such as Fe$_2$CoGa [80,106] and Mn$_2$NiGa [107]. The same trend is also found in Fe$_2$CoGa nanoparticles.
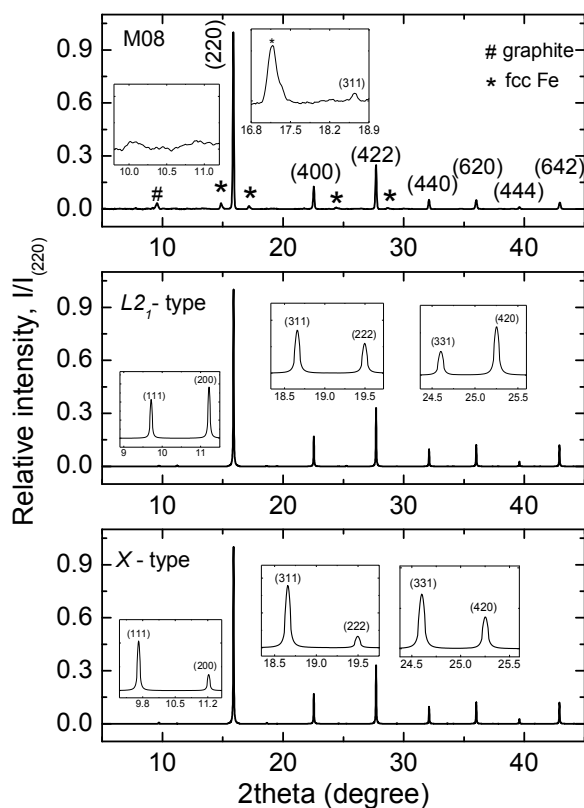
Figure 5.1 XRD patterns of sample M08 and theoretically calculated $L2_1$ and X types of structure (a = 5.767 Å). The indices of the Bragg reflections correspond to $L2_1$ ordered Fe$_2$CoGa phase. X-ray photon energy: 22 keV. The inserts are the enlarged views of selected 2theta regions.

Table 5.1 Relative intensities of the reflections for Fe$_2$CoGa compounds of various structure types and sample M08.

	Relative intensity						
	(111)	**(200)**	**(220)**	**(311)**	**(222)**	**(331)**	**(420)**
L2$_1$	0.43	0.57	100	0.32	0.22	0.17	0.34
L2$_{1B}$	0.35	0.24	100	0.26	0.05	0.13	0.16
X	0.36	0.24	100	0.27	0.05	0.13	0.16
M08	—	—	100	0.23	—	—	—

*X-ray energy: 22 keV.

It is also probable that Fe$_2$CoGa phases are ordered in a *L2$_{1B}$* structure as reported in the literature [108]. In *L2$_{1B}$* ordered Fe$_2$CoGa, Co atoms not only occupy half of the nominal Fe sites and Fe and Co atoms have equal probability to enter the 8c sites. As described in Table 5.1, the close similarity of the relative intensities of characteristic reflections in Fe$_2$CoGa of *X* and *L2$_{1B}$* structures render difficulty to distinguish in-between. In this sense, additional anomalous XRD or neutron diffraction measurements are required to unambiguously identify the correct structure of Fe$_2$CoGa phase. In a recent report, Brown et al. employed neutron diffraction to conclude the crystal structure of Mn$_2$NiGa as *L2$_{1B}$* instead of the commonly assumed *X* structure [109].

As similar to the case for Fe-excess Co$_2$FeGa nanoparticles, the main Fe$_2$CoGa phase is found to coexist with a small amount of fcc Fe impurities. The reflections for the impurity phase are at 14.86°, 17.19°, 24.39°, and 28.68°. Calculations based on integration areas of the impurity (111) and Fe$_2$CoGa (220) reflections reveal a phase composition of 5.3% fcc Fe and 94.7% Fe$_2$CoGa in sample M08.

5.3   Short range order structure

Even though the structure of Fe$_2$CoGa nanoparticles is found as *X*-type, the coexistence of *A2* or *B2* disorder, however, cannot be completely excluded. Therefore, EXAFS was utilized to provide additional short range order information which helps to distinguish among different structure type of Fe$_2$CoGa phase. First, the EXAFS fits were carried out assuming a *L2$_1$* ordered structure. The Fourier transforms of the spectra and the fits at K-edges of Co, Fe, and Ga of sample M08 assuming a *L2$_1$* ordered structure model are shown in Figure 5.2. The FT spectra at all edges are similar to those for sample M05 due to the similarities in the backscattering amplitude and phase shift of Fe and Co. Best fitting quality is found at the *X*-site. It is also found that the fits assuming a bcc Fe structure are also reasonably good. As discussed in *Chapter 3*, this might point to the presence of bcc Fe impurities, which are not resolved by XRD. This is possible since sample M08 is with excess iron. Again the EXAFS evidence for a *L2$_1$* or *X*-type Co$_2$FeGa structure derived from the Fe K edge is not conclusive.

The structural matching at the Co and Ga edges is comparable with a somewhat poor fitting quality (R$_f$= 0.032 ~ 0.038). This provides a hint that the *L2$_1$* model might not be optimal for sample M08. EXAFS fits were additionally carried out assuming a *X*-type structure model in the R-range of 1.0 ~ 3.0 Å at Fe K-edge and 1.0 ~ 5.0 Å at the K-edges of Co and Ga. There is no significant improvement in the fitting at Fe edge. In comparison, the fitting qualities are significantly improved at Co and Ga edges. This verifies that *X*-type ordered structure might be dominant in Fe$_2$CoGa phase of sample M08. EXAFS analysis might be a valuable approach to distinguish the *L2$_1$* and *X* ordered structures. By performing first shell fits of sample M08 at Fe edge, the obtained bond lengths are 2.46 Å and 2.48 Å for

Fe–Co and Fe–Ga bonds, respectively. This verifies the highly ordered *X* structure in the sample. EXAFS fits are also carried out at the K-edges of Co, Fe, and Ga assuming *A2* or *B2* structure. Poor fitting qualities are obtained compared to those for *L2$_1$* and *X* structure. In short, EXAFS analysis on sample M08 provides evidence of *X*-type Fe$_2$CoGa in sample M08.
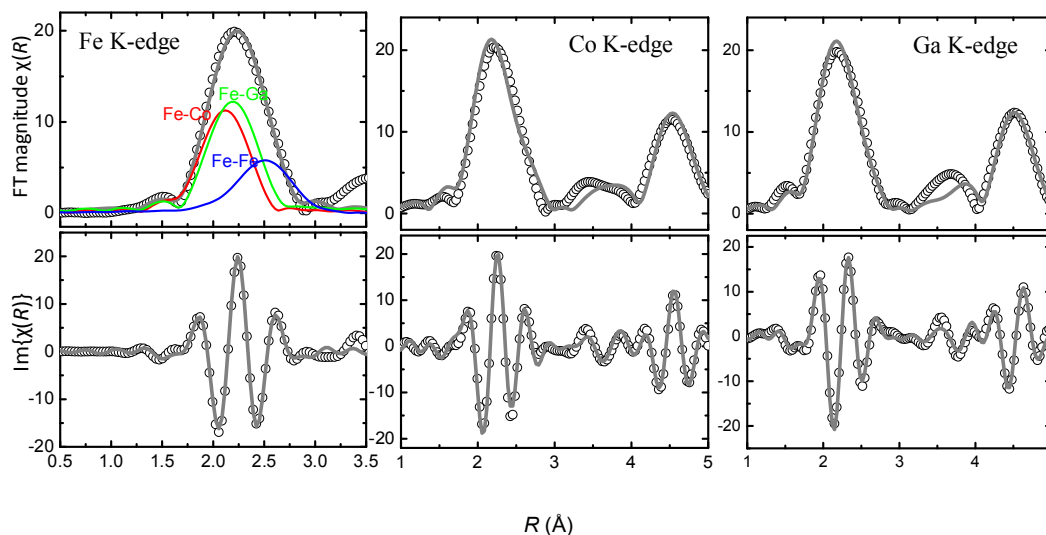
Figure 5.2 Magnitude and imaginary component of Fourier transforms of EXAFS spectra of sample M08 at the K-edges of Fe, Co, and Ga assuming a *L2$_1$* ordered structure. The fits to the data are shown as solid lines. At Fe K edge, the paths included into EXAFS fits are also plotted.

5.4   Magnetic properties

The room temperature Mössbauer spectrum of sample M08 is shown in Figure 5.3 and the fitted Mössbauer parameters are given in Table 5.2. The Mössbauer spectrum of sample M08 was fitted by one superparamagnetic doublet and two magnetic sextets. According to Jaggi et al. [80], two sextets have been observed for bulk Fe$_2$CoGa with an inverse Heusler structure. The derived hyperfine magnetic fields are 310 kOe and 235 kOe and the isomer shifts are 0.09 ± 0.03 mm/s and 0.28 ± 0.05 mm/s, respectively. Therefore, the hyperfine magnetic fields of the sextets are close to the reported H_{hff} value for bulk Fe$_2$CoGa phase confirming the formation of *X*-type ordered Fe$_2$CoGa phase. The doublet is assigned to the nanoparticles with the particle size smaller than the critical superparamagnetic size limit of Fe$_2$CoGa

As shown in Fig. 5.4 (a), the saturation magnetic moment at 300 K and 5 K are 3.59 μ_B and 3.89 μ_B, respectively. A higher saturation magnetization value of 5.09 μ_B has been reported for bulk Fe$_2$CoGa Heusler compound in the literature [64]. According to the left side of the Slater–Pauling curve, however, the spin magnetic moment per unit cell value is predicted to be 4.0 μ_B for perfect *L2$_1$* ordered Fe$_2$CoGa compounds. Theoretical calculations, however, reveal that the magnetic moment of Fe$_2$CoGa depends strongly on the structure: 6.17 μ_B/f.u. for *L2$_1$* ordered Fe$_2$CoGa and 5.27 μ_B/f.u. for *X* ordered Fe$_2$CoGa [102,106]. Therefore the measured magnetic moment of Fe$_2$CoGa nanoparticles is significantly lower than the theoretically predicted values.

As discussed above, XRD and EXAFS verify the *X*-type Fe$_2$CoGa phase in the nanoparticles. The possibility that Fe$_2$CoGa phase crystallize in *L2$_{1B}$* structure, however, cannot be completely excluded. Further investigations using anomalous XRD or neutron diffraction are required to unambiguously determine the structure type of the Fe$_2$CoGa nanoparticles.

Temperature dependent SQUID measurements were utilized to verify the superparamagnetic behavior of the small particles in sample M08. Field cooled (FC) and zero field cooled (ZFC) magnetization curves were measured in a temperature range of 5 ~ 300 K under a magnetic field of 0.01 T. As shown in Figure 5.4 (b), characteristic FC/ZFC curves for superparamagnetic nanoparticles are observed. The blocking process spread over a wide temperature range signifying a rather wide size distribution of the nanoparticles. The magnetic susceptibility reaches maximum at around 30 K (the nominal blocking temperature) corresponding to the contribution from the smallest particles in the sample. This ZFC/FC behavior is consistent to the large fraction (up to 22.1%) of the nanoparticles in a superparamagnetic state as revealed by Mössbauer measurements.
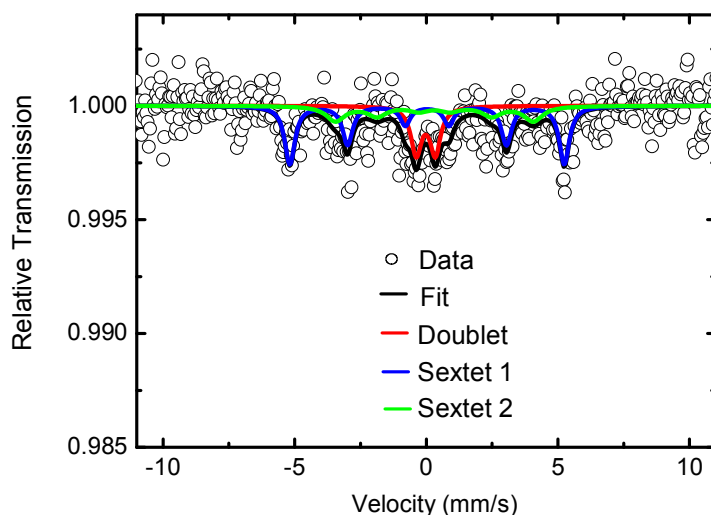
Figure 5.3 Mössbauer spectrum of M08 at room temperature. Superparamagnetic doublets and static magnetic sextets are shown by red, blue, and green lines.

Table 5.2 Fitted Mössbauer parameters (isomer shift δ, quadrupole splitting Δ, and hyperfine field H$_{hf}$) of sample M08.

ID	δ (mms^{-1})	Δ (mms^{-1})	H$_{hf}$ (kOe)	Area (%)
M08	-0.02	0.72	—	22.1
	0.03	0	323.3	53.1
	0.31	0	233.2	25.2
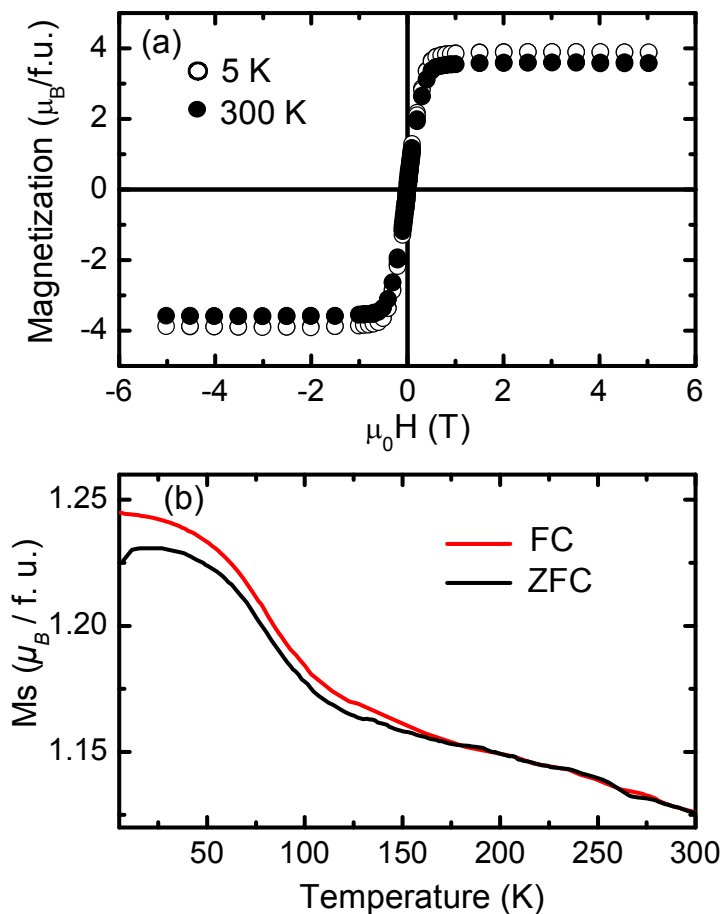
Figure 5.4 Magnetic properties of sample M08: (a) magnetization curves at 5 K and 300 K; (b) temperature dependent FC-ZFC curves.

5.5 Summary

In this chapter, the long and short range order structure, and magnetic properties of Fe$_2$CoGa nanoparticles are investigated. From synchrotron radiation based XRD, EXAFS and Mössbauer spectroscopy, the structure of the Fe-rich Fe$_2$CoGa nanoparticles could be better described by the *X*-type structure compared to the *L2$_1$* structure, even though the possibility of *L2$_{1B}$* ordered structure cannot be excluded. Further experimental and theoretical studies on both bulk and Fe$_2$CoGa nanoparticles are required to clarify the unresolved issues in this work.

6 Size control and synthetic transferability

One major task of this work is to develop feasible chemical synthesis approaches for ternary Heusler nanoparticles. It is found that the particle size of Heusler nanoparticles can be controlled by the amount, morphology, and size of the silica supports. Co_2FeGa and Fe_2CoGa nanoparticles described in precious chapters are prepared by the silica assisted solid state chemical route. The obtained nanoparticles generally exhibit a bimodal size distribution. To optimize this route, the strategies to obtain nanoparticles with narrow distributed particle size are explored. Efforts have also been made to apply the same chemical route of Co_2FeGa nanoparticles to similar Heusler compounds aiming to increase the synthetic coverage on a variety of Heusler nanoparticles. Other chemical approaches were also attempted with various degrees of success. The experimental results and related discussions are presented in this chapter.

6.1 Introduction

6.1.1 Size control

Particle size control is important in the chemical synthesis of intetmetallic nanoparticles, which facilities the investigations on size dependent properties of Heusler nanoparticles. For magnetic nanoparticles, magnetic separation might be an intrinsic choice for size selection as demonstrated for Fe-Co and other nanoparticles [110–112]. Alternatively the size of the nanoparticles could be sorted by high speed centrifugation methods including step-density-gradient centrifugation [113]

As revealed in previous chapters, using the silica spheres supported approach, the obtained nanoparticles generally develop a bimodal size pattern, which is not favorable for examining the particle size effect. In this work several strategies have been implemented for Co_2FeGa nanoparticles aiming to obtain nanoparticles with narrow size distribution: (1) size separation by post-synthesis centrifugation; (2) using other silica supports and annealing parameters; and (3) decreasing precursor concentration in the current route.

6.1.2 Synthetic transferability

Co_2FeGa is a type III half metal, which means that the electronic structure is not ideal for spintronic applications. Among the numerous Co-based Heusler compounds, Co_2FeZ (Z = Al, Si) and Co_2YGa (Y = Mn, Cr, V) have been extensively investigated due to their importance in spintronic devices. Co_2FeAl and Co_2FeSi Heusler compounds are presently used in TMR devices. Co_2MnSi and Co_2MnGa compounds have been extensively studied due to their robust HMF properties. Co_2CrGa Heusler compounds is also promising candidate for spintronics because both $L2_1$ and $B2$ phase exhibit stable HMF properties. Co_2CrGa compounds, however, are limited by low magnetic moment and low Curie temperature. Successful preparations of Heusler nanoparticles of the above compositions would be favorable from the viewpoint of applications and it also enables a direct comparison in structure and properties of the same compounds in bulk and nanoparticle forms. In this work, chemical preparations of the above Co-based Heusler nanoparticles are investigated based on the approach for Co_2FeGa nanoparticles .

6.1.3 Colloidal chemistry approaches

Other available chemical methods for binary and ternary intermetallic compounds are also attractive for the preparation of the Heusler nanoparticles. Colloidal chemical methods

are among the most established ways to prepare metallic nanoparticles of controlled size and morphology. Recently, Fe_3Si nanoparticles were prepared by a high temperature colloidal approach [39]. Up to date, no ternary Heusler nanoparticles have been synthesized using colloidal chemical routes. Pd_2Sn binary nanoparticles have been prepared by a high temperature colloidal approach in organic media [114]. In this work efforts are devoted to prepare ternary Pd_2MnSn nanoparticles using similar processing parameters.

Nanostructured solar cells have been extensively investigated [115–117]. Especially, ternary nanocrystals such as $CuInS_2$ are envisaged to possess higher energy conversion efficiency and are with less environmental impacts [118]. In terms of cell performance, cost, and environmental tolerance, theoretical calculations indicate that ternary I-III-VI nanoparticles such as Li-Cu-S are also promising materials. Therefore, the synthesis approaches for $CuInS_2$ or Cu_2S nanocrystals [119–120] are modified for the preparation of Li-Cu-S nanoparticles.

6.2 Particle size control

6.2.1 Post-synthesis size selection

Progress has been made in separating the smaller nanoparticles via a sequence centrifugation process. First, low speed centrifugation (6000 rpm for 20 min) was performed to separate the large particles. The supernatant obtained from the first step were treated by the followed high speed (18000 rpm for 20 min) centrifugation to obtain mall particles. As shown in Figure 6.1 (b), most obtained particles are uniformly dispersed with small size (6 ~ 8 nm). The XRD pattern of the separated small nanoparticles is shown in Figure 6.2. Due to size-induced peak broadening, only the intense (220), (400) and (422) reflections are observed. To verify the $L2_1$ ordered Co_2FeGa structure, EXAFS fits were carried out on the Co and Fe K-edges. The Fourier transforms and fits of the spectra at Co and Fe edges of the small Co_2FeGa nanoparticles are shown in Figure 6.3. The fits were performed assuming $L2_1$ ordered Co_2FeGa with a lattice constant of 5.737Å and only SS paths were included in the fits. At both edges, reasonably good fitting qualities are realized in the R-range of 1.0 ~ 5.0 Å with R-factors of 0.02 ~ 0.03. The fitted values of E_0 and R are physically reasonable. This indicates that the $L2_1$ ordered Co_2FeGa phase is preserved in the small Co_2FeGa nanoparticles. The amount of the obtained small Co_2FeGa nanoparticles, however, is very small making other characterizations including SQUID and Mössbauer spectroscopy impossible.
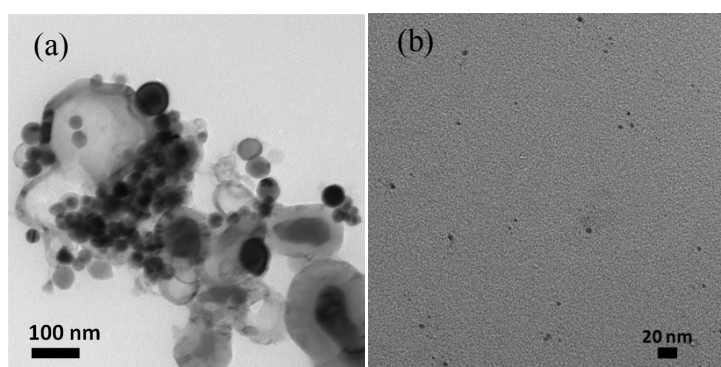
Figure 6.1 TEM micrographs showing particle size separation of Co_2FeGa nanoparticles by two-step centrifugation procedures: (a) the large nanoparticles; (b) the separated small nanoparticles.
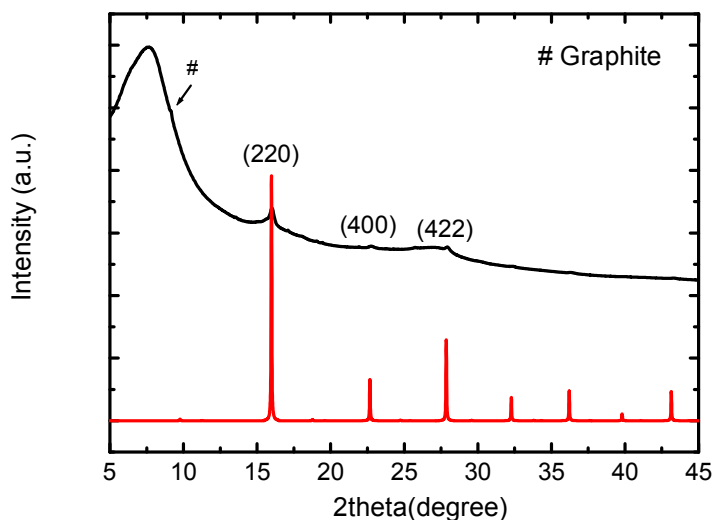
Figure 6.2 XRD pattern of the separated small Co$_2$FeGa nanoparticles. The indices of the Bragg reflections corresponding to *L2$_1$* ordered Co$_2$FeGa phase are displayed together with the theoretically calculated XRD pattern (a = 5.737 Å). X-ray photon energy: 22 keV.
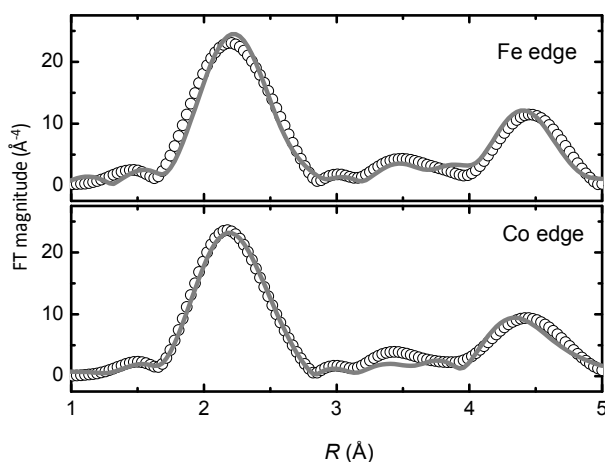
Figure 6.3 Magnitudes of Fourier transforms of EXAFS spectra of the small Co$_2$FeGa nanoparticles at the K edges of Fe and Co. The fits to the data are shown as solid lines.

6.2.2 Optimizing processing parameters

An alternative approach for size control is to optimize the processing parameters in the chemical synthesis to directly prepare Co$_2$FeGa nanoparticles of desired size. In the silica assisted approach for Co$_2$FeGa nanoparticles, the assemblies of silica spheres with an average particle size of around 20 nm are used as the "templates" to host the formation of the

Co$_2$FeGa nanoparticles. The dimension and distribution of the metal species are closely related to the packing of the silica spheres, which are not easily controlled. In this sense, nanoporous silica gels with an average pore size of 6 nm might be advantageous since a size confinement is imposed and the minimum particle size might be less than or equal to that of the pore size of the gels. In addition the annealing parameters are fixed as 850 °C for 5 h in previous experiments. For nanostructured materials, due to the small size, the diffusion time of metal atoms required for new phase formation might be several orders shorter than bulk materials. Therefore, the annealing time can be significantly decreased. A short annealing time might also improve the particle size distribution by reducing the extent of Ostwald ripen effect when larger particles grow in the cost of the contraction of smaller particles. The relevant sample conditions are described in Table 3.2 (see page 15 in *Chapter 3*). Figures 6.4 (a) to (c) shows the TEM micrographs of samples S03 and S04. As shown in Figures 6.4 (a) and (b), Co$_2$FeGa nanoparticles of a bimodal size distribution are observed. The small particles are around 5 ~ 8 nm, which match to the pore size of the gels. The size of the large particles are in the range of 15 ~ 30 nm. When increasing the annealing time to 5 h, the size distributions of both the large and the small particles become wider and the size of the large particles increases to around 20 ~ 40 nm. From the viewpoint to obtain Co$_2$FeGa nanoparticles of smaller size, a short annealing time might be favorable.

For Co$_2$FeGa nanoparticles prepared using nanoporous silica gels, the formation of metal nanoparticles with a size much larger than the pore size might be attributed to the higher concentration of Fe and Co precursors in our approach, which is around 1.8 times of that used for Fe-Co nanoparticles reported in the literature [70]. Unevenly deposited metal salts within the pores might eventually result in metal nanoparticles with an irregular morphology and an abnormal size distribution pattern. The heterogeneous distribution of metal salts within the pores might be alleviated by decreasing the concentration of metal load. As reported by Seo et al. [70], the average particle size decreased from 7 nm to 4 nm with a four-fold decrease in the precursor concentration for Fe-Co alloy nanoparticles. A TEM micrograph of sample S02 is shown in Figure 6.4 (d). It is found that larger Co$_2$FeGa nanoparticles still coexist with small particles. Similar phenomenon is also found for the Co$_2$FeGa nanoparticles prepared using 20 nm silica spheres. It is assumed that the bimodal size distribution is an intrinsic feature of this chemical approach.

6.3   Synthetic transferability

6.3.1 Co$_2$FeZ (Z = Al, Si)

The precursors for the main group elements Al and Si are aluminum chloride (AlCl$_3$) and tetraethyl orthosilicate (TEOS, Si(OC$_2$H$_5$)$_4$). The XRD patterns for Co$_2$FeAl and Co$_2$FeSi nanoparticles prepared using the same approach as for Co$_2$FeGa are shown in Figures 6.5. For both Co$_2$FeAl and Co$_2$FeSi nanoparticles, the main phase can be tentatively assigned to the relevant Heusler phases. As similar to the case for Co$_2$FeGa nanoparticles, the impurity phases might be attributed to fcc Co due to excess Co in the samples. The compositions derived from XAFS analyses indicate compositions of Co$_{2.0}$Fe$_{0.74}$Al$_x$ and Co$_{2.0}$Fe$_{0.72}$Si$_x$. EXAFS fits were carried out at Co K-edge on both samples in the R-range of 1.0 ~ 3.0 Å assuming $L2_1$ ordered Heusler compounds with the reported lattice constants in the literature. The Fourier transforms and fits of the spectra at Co edges of the Co$_2$FeAl and Co$_2$FeSi nanoparticles are shown in Figure 6.6. The R-factors are 0.026 and 0.008 for Co$_2$FeAl and Co$_2$FeSi, respectively. In short, XRD and EXAFS analyses indicate the successful synthesis of Co$_2$FeAl and Co$_2$FeSi even though the processing parameters are to be optimized in future work.
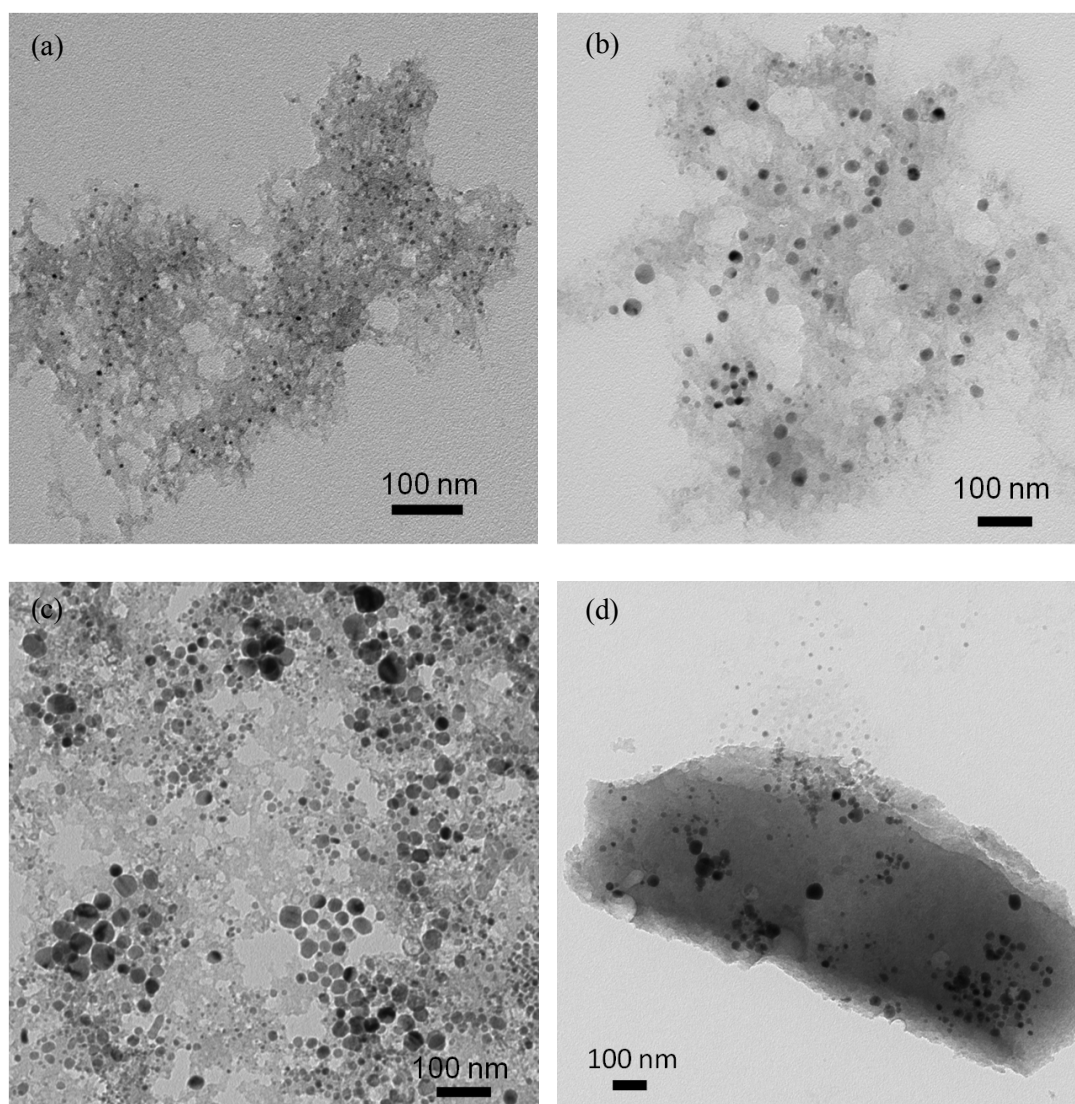
Figure 6.4 TEM micrographs showing the particle size and morphology of Co₂FeGa nanoparticles: (a) – (b) sample S03; (c) sample S04; and (d) sample S02.
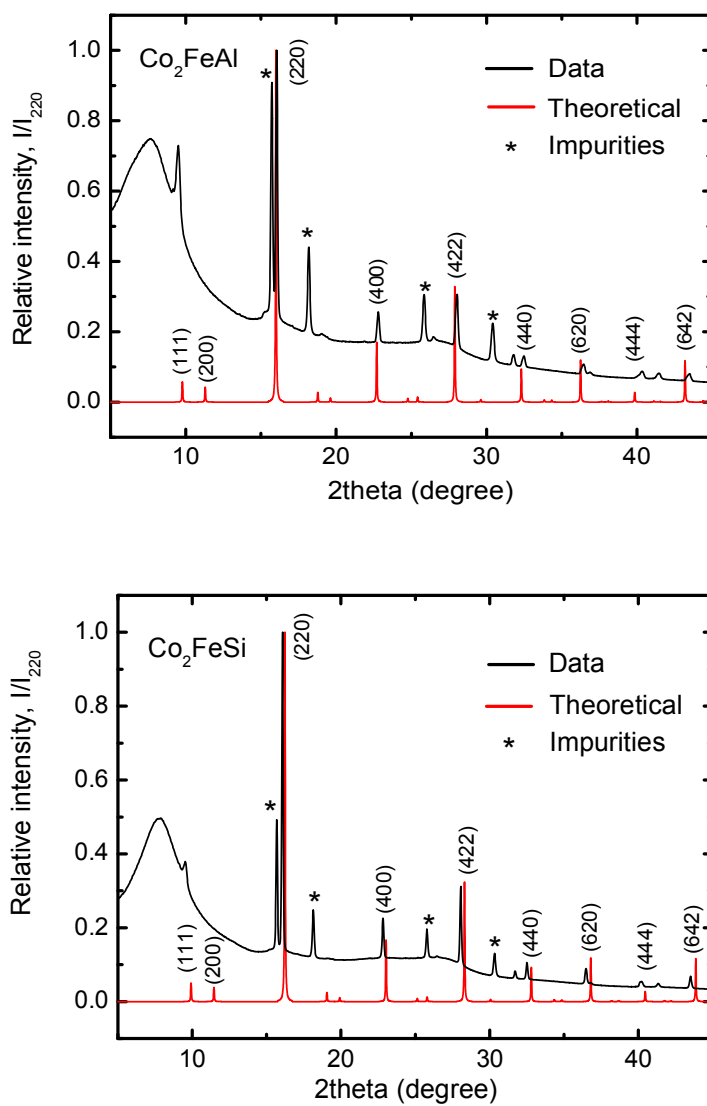
Figure 6.5 XRD patterns for Co₂FeAl and Co₂FeSi nanoparticles prepared using the same approach as for Co₂FeGa nanoparticles.
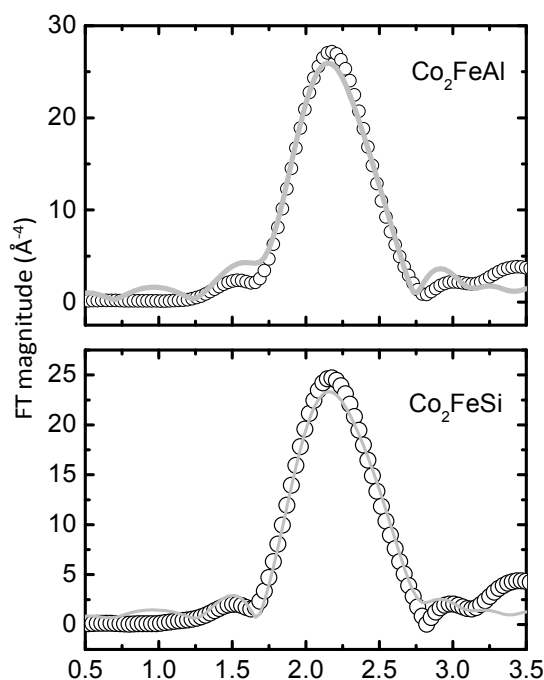
Figure 6.6 Magnitudes of Fourier transforms of EXAFS spectra of Co_2FeAl and Co_2FeSi nanoparticles at Co K-edge. The fits to the data are shown as solid lines.

6.3.2 Co_2YGa (Y = Mn, Cr, V)

The precursors for the transition metals are metallic chlorides and nitrate (chrome). The XRD pattern and TEM micrograph for Co_2MnGa nanoparticles prepared using the same approach as for Co_2FeGa are shown in Figures 6.7.
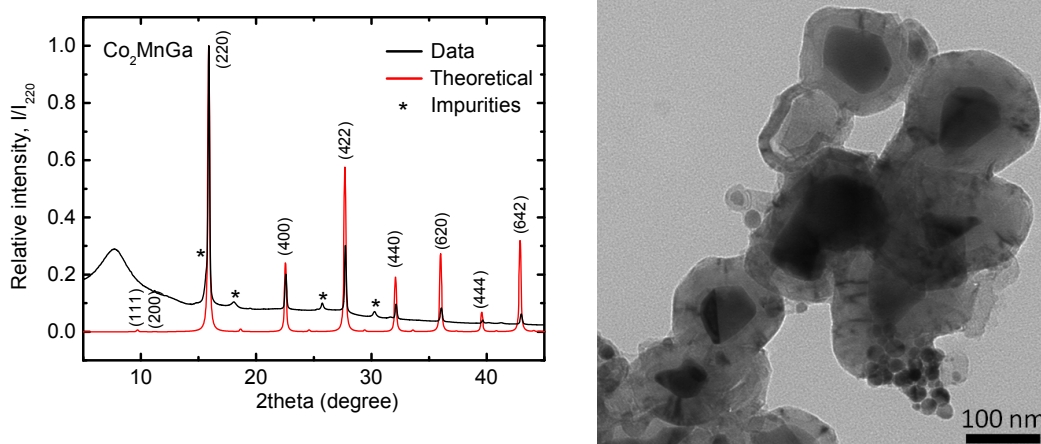
Figure 6.7 XRD pattern and TEM micrograph for Co_2MnGa nanoparticles prepared using the same approach as for Co_2FeGa nanoparticles.

From XRD, the main phase of Co$_2$MnGa nanoparticles can be tentatively assigned to Co$_2$MnGa Heusler phase. Unknown impurity phases are also observed, which are also revealed by XANES analysis. TEM micrograph of Co$_2$MnGa nanoparticles show typical bimodal particle size distribution with large particles (50 ~ 80 nm) and small particles (10 ~ 20 nm), as observed for Co$_2$FeGa nanoparticles. For the cases of Co$_2$CrGa and Co$_2$VGa nanoparticles, the syntheses seem unsuccessful since the observed principal reflections don't match with the intense (220), (400), and (422) peaks of the Heusler compounds.

6.4 Colloidal chemistry approaches

6.4.1 Pd-Mn-Sn

Pd$_2$Sn binary nanoparticles have been prepared by a high temperature colloidal approach in organic media [114]. This approach was adapted by adding manganese chloride aiming to prepare ternary Pd$_2$MnSn Heusler nanoparticles. The XRD pattern of the as dried Pd-Mn-Sn nanoparticles is shown in Figure 6.8. XRD analysis indicates that Pd and Pd$_2$MnSn phases might coexist with unknown impurity phases. Figures 6.9 show the TEM micrographs of the obtained as-prepared colloidal. Both large (50 ~ 80 nm) and small (5 ~ 8 nm) nanoparticles are observed. The distinctive electron phase contrast of various nanoparticles indicates the nanoparticles might be of different phases, which is consistent with the results from XRD. It seems that the colloidal chemistry approach is not easily adapted to ternary Heusler alloy systems.
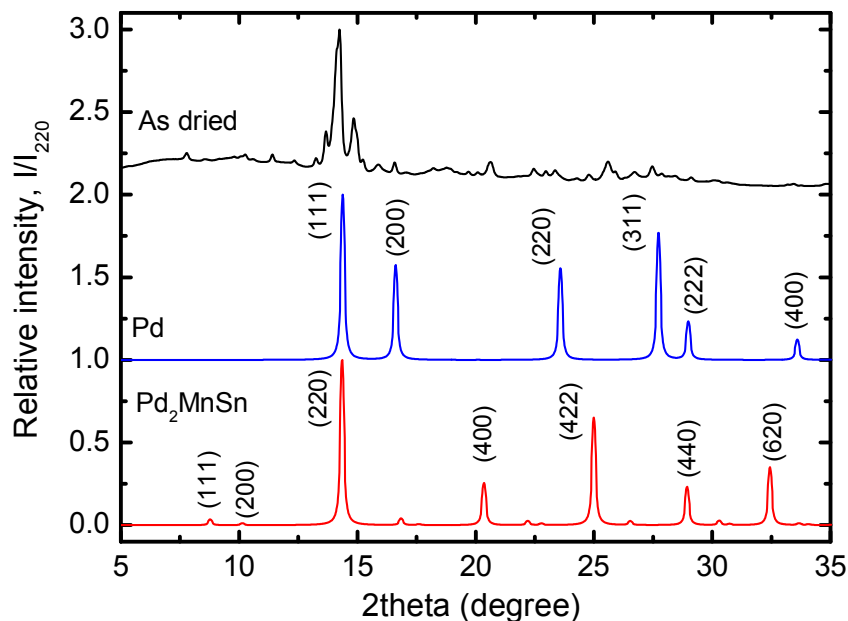
Figure 6.8 XRD pattern of Pd-Mn-Sn nanoparticles prepared from the adapted colloidal chemistry approach. The calculated diffraction pattern of Pd and Pd$_2$MnSn are co-plotted for comparison.
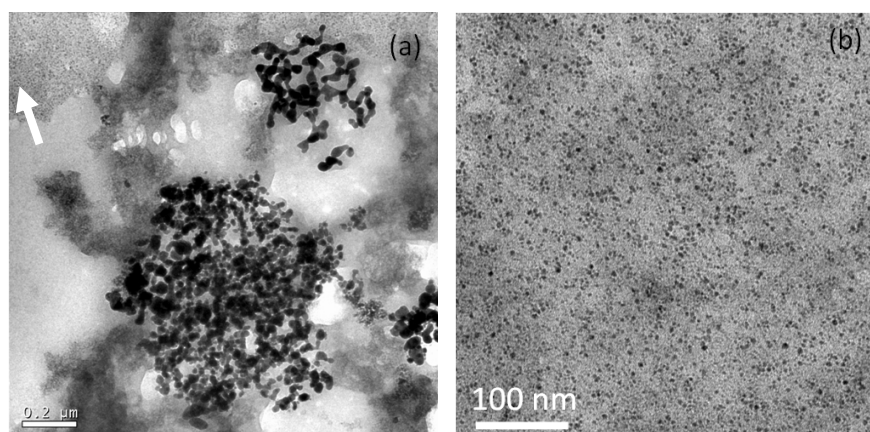
Figure 6.9 TEM micrographs showing the particle size and morphology of Pd-Mn-Sn nanoparticles prepared from colloidal chemistry approach. Both large and small (indicated by a white arrow) nanoparticles are observed in (a). An enlarged view of the small nanoparticles marked with an white arrow in (a) is shown in (b).

6.4.2 Li-Cu-S

A colloidal chemistry approach to prepare Li-Cu-S colloidal was investigated. The original route was for Cu$_2$S nanoparticles by the reactions between metal acetates and dodecanethiol in 1-octadecene with a high boiling point. The interest lies at whether it can be adapted to ternary Li-Cu-S nanoparticles by adding lithium acetate. Figures 6.10 show the TEM micrograph and size distribution of Li-Cu-S nanoparticles. Narrow distributed nanoparticles are obtained. XRD and HRTEM analyses, however, reveal the absence of ternary Li-Cu-S phase. Also chemical analysis indicates the absence of lithium species in the samples. The obtained nanoparticles might consist of only Cu$_2$S nanocrystals.
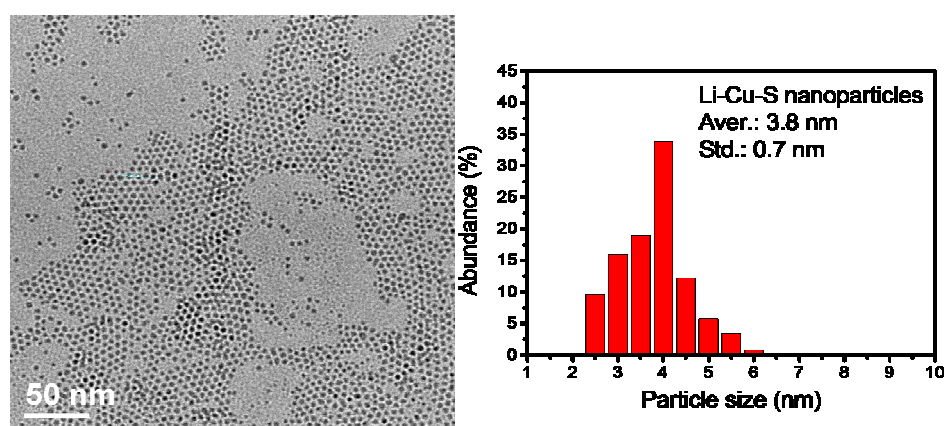
Figure 6.10 TEM micrographs and particle size distribution of Li-Cu-S nanoparticles from colloidal chemistry approach.

6.5   Summary

Structure and size control are of critical importance in a chemical synthesis of Heusler nanoparticles. In this chapter, strategies of size control on silica supported Co_2FeGa nanoparticles are examined. It is demonstrated that a two-step sequence centrifugation is capable to separate the small nanoparticles from the large ones. The size separation efficiency would be enhanced if Co_2FeGa nanoparticles possess a favorable bimodal size distribution which facilitates subsequent size separation. As an example, a coupling of using silica gel with pore size of 6 nm and shorter annealing time might be appealing to obtain Co_2FeGa nanoparticles with separable size ranges. Excellent synthetic transferability is found in Fe_2CoGa, Co_2FeZ (Z = Al, Si), and Co_2MnGa nanoparticles. Synthetic approaches employing colloidal chemistry are also attempted but with few success. One of the major issues confronted in this approach for Heusler nanoparticles is the unwanted phase separation, which is to be resolved in future investigations.

7 Chemical synthesis based on synchrotron X-rays

Recently, progress has been made in radiation synthesis of metallic nanoparticles utilizing synchrotron X-rays [121–124]. This approach is suitable for preparing monometallic and alloy nanoparticles utilizing the intrinsic advantages of ultrahigh dose rate and photon flux of synchrotron X-rays. This new synthesis method is simple, highly productive, and the obtained nanoparticles are biocompatible. The obtained metal nanoparticles have been successfully applied in wide application fields including nanobiotechnology and nanomedicine. In this chapter, experimental results on radiation synthesis of a variety of metallic nanoparticles are described. This approach has also been extended to prepare ternary nanoparticles in aqueous solutions and the results are also discussed.

7.1 Introduction

Nanotechnology is playing an increasingly important role in the fight against cancer. In particular, gold nanoparticles are promising candidates as carriers for targeted drug delivery, contrast agents and radiotherapy enhancers. To achieve maximum effectiveness in enhancing radiotherapy, gold nanoparticles must have optimal size and surface properties.

A one-solution synthesis approach using X-ray irradiation was developed to prepare polymer modified gold nanoparticles that might meet the requirements of suitable size, high concentration, colloidal stability, and biocompatibility. The method consists of bombarding a precursor solution containing gold ions and the polymeric stabilizers (e.g. polyethelne glycol) with intense X-rays produced by a synchrotron source. The irradiation was found to stimulate the formation of gold nanoparticles protected by the biocompatible polymer chains. Compared to other synthetic methods, this approach has several advantages: (1) cleanliness, since the system is free of pre-added reducing agents and surfactants; (2) high reproducibility and capability to scale up for mass production; (3) pristine biocompatible polymers are used; (4) easy to increase the concentration with excellent stability.

7.2 Monometallic nanoparticles

7.2.1 Au and Ag nanoparticles [122,123]

Figure 7.1 shows the TEM micrographs of polyethelne glycol (PEG) modified gold nanoparticles (PEG-Au) formed by various exposure times. After a X-ray exposure of 30 sec, the formed gold clusters interconnect/fuse together leading to an overall size above 100 nm in the network structure. After further exposure for 5 min, well-dispersed gold nanoparticles with size < 7 nm are obtained. During an additional exposure for up to 15 min (Figure 4(c)), the size and particle morphology remain unchanged. For PEG 20000, the exposure time effects are similar to PEG 6000 but with some noteworthy differences. For example, after an exposure of 30 sec large gold nanoparticle (15 ~ 20 nm) are formed instead of the inter-connected structure. Additional x-ray irradiation leads to a decrease in the particle size to approximately 8 nm.

The dependences of gold particle size and morphology on exposure time (3 ~ 900 sec) are linked to the evolution of optical absorption spectra as shown in Figure 7.2. For PEG-Au nanoparticles formed after a 10 sec exposure, only a very broad absorption peak centering at approximately 542 nm is observed indicating the larger cluster size and small yield of colloidal gold. These colloidal are not stable and serious flocculation occurs and precipitates formed. At exposure time longer than 1 min, the characteristic surface plasmon resonance (SPR) peak of colloidal gold appears at 509 nm. Using the intensity of the SPR peak as an

indicator of the colloidal gold concentration, it is found that almost all gold precursor ions has been reduced to colloidal gold after 2 ~ 3 min of exposure. This fast reducing speed and ~ 100% reduction efficiency adds to the advantages of the X-ray irradiation approach.
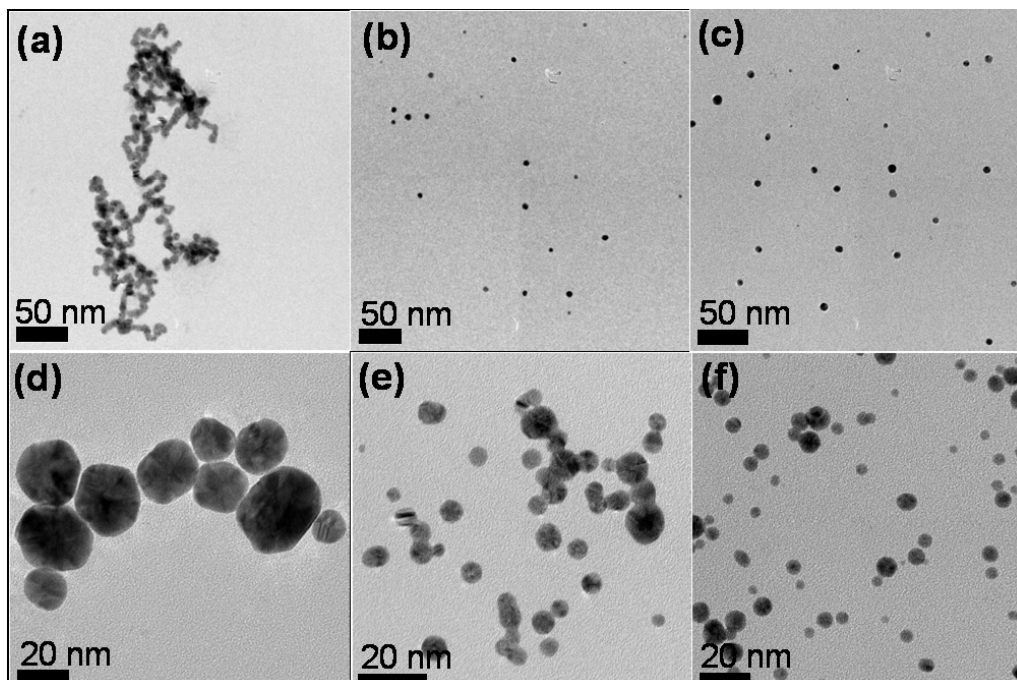
Figure 7.1 TEM micrographs showing the effects of X-ray dosage and PEG molecular weight on gold particle size, distribution and morphology. PEG6000: (a) 30 sec (b) 5 min (c) 15 min; PEG20000: (d) 30 sec; (e) 1.5 min; (f) 5 min.
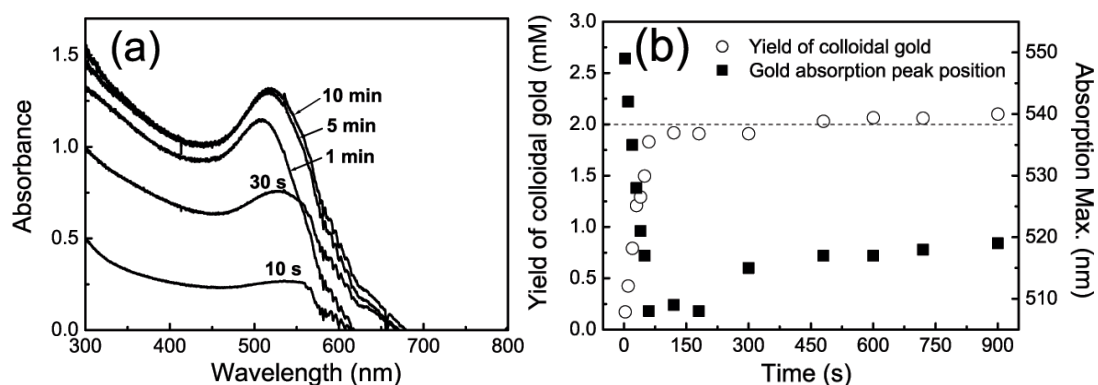
Figure 7.2 Visible optical absorption of PEG-Au nanoparticles prepared by various exposure time: (a) absorption spectra; (b) the variation of colloidal yield and gold SPR peak position.

The same approach is adapted for the preparation of silver nanoparticles in solutions. Figures 7.3 (a) and (c) show TEM results for PEG-Ag for 30 sec and 5 min exposure; Figures 7.3 (b) and (d) show the corresponding size histograms. The measured particle size is 7.2 ± 2 nm for 30 sec exposure and the size distribution is broad. After 5 min exposure, the measured size is 5.2 ± 0.9 nm and the distribution is narrow. Equivalent results are obtained under similar experimental conditions for polyvinyl pyrrolidone (PVP) modified silver (PVP-Ag) nanoparticles (Fig. 7.3 (e) to (h)): the measured sizes are 6.2 ± 2.9 nm and 3.8 ± 1.1 nm.
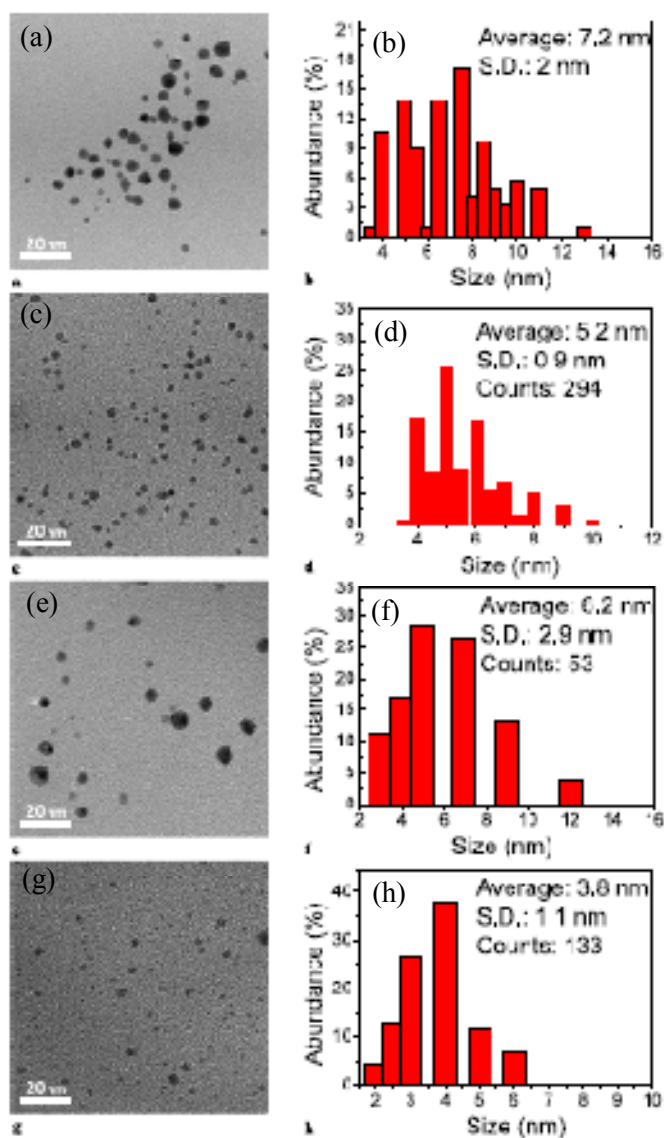
Figure 7.3 Typical TEM micrographs and histograms showing the size and distribution of silver nanoparticles with PEG and PVP stabilization. For all images and histograms, [AgNO3] =1 mM. (a) and (b): PEG added, [PEG] = 0.3 mM, 30 sec exposure; (c) and (d): [PEG] = 0.3 mM, 5min exposure; (e) and (f): PVP added, [PVP] = 0.12 mM, 30 sec exposure; (g) and (h): [PVP] = 0.12 mM, 5 min exposure. Scale bar 20 nm.

7.2.2 Application of gold nanoparticles [124,125]

A new approach for the synthesis of gold nanoparticles was developed. The synthesis is activated by irradiation with intense synchrotron X-rays (photon energy of 8 ~ 15 keV) yielding highly concentrated, stable colloids with no reducing agents. Gold nanoparticles could be useful for a number of therapeutical and diagnostic applications. Specifically, the nanoparticles could improve the selectivity of cancer treatment (chemotherapy and radiotherapy) in the targeted tumor areas. Here two examples are described in terms of *in vitro* and *in vivo* applications of the gold nanoparticles prepared by synchrotron X-ray irradiation.

TEM micrographs in Figure 7.4 illustrate the interaction between gold particles and EMT-6 cells. Unmodified gold nanoparticles are found as large clusters and are located within the intercellular matrix. Individual gold particles can also been differentiated with original size. Occasionally gold clusters immobilized within cytoplasm are observed. As described in Figure 7.4 (c), some gold clusters are internalized while other clusters (arrow marked) are experiencing cellular uptake. The pathway track of internalized gold nanoparticles towards perinuclear region is shown in Figure 7.4 (d). The TEM data indicate that unmodified gold nanoparticles penetrate into the EMT-6 cells, even though the amount of the cellular uptake is small.
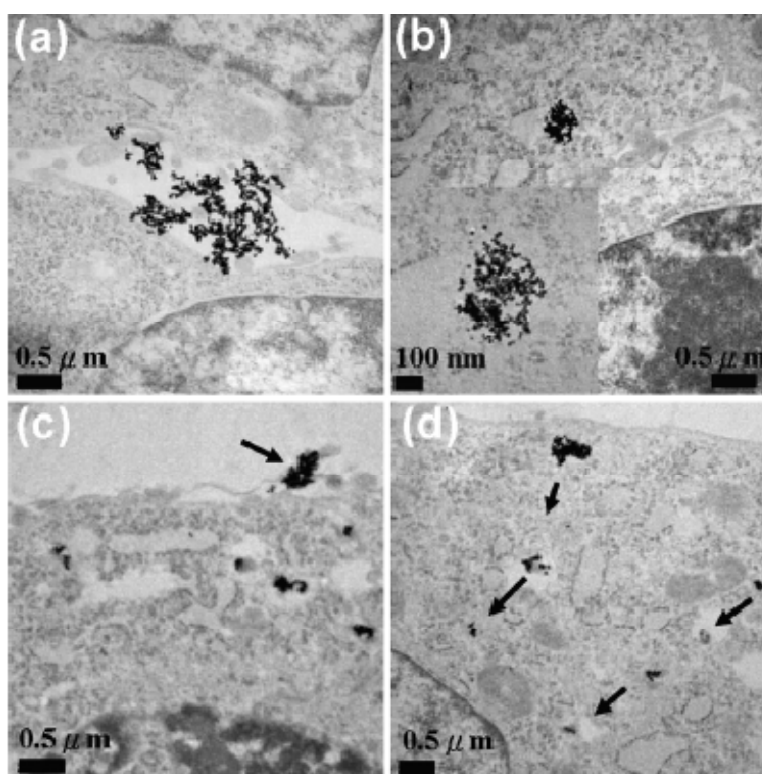
Figure 7.4 TEM micrographs depicting the distribution of unmodified gold nanoparticles within cellular environments: (a) inter-cellular distribution, (b) cluster of gold nanoparticles, (c) gold nanoparticles attached and uptaken by EMT-6 cell and (d) pathway track of internalized gold nanoparticles towards perinuclear region.

The spatial distribution of X-ray synthesized, PEG-Au nanoparticles in tumor-bearing mice and their time dependent accumulation were investigated. As shown in Figure 7.5, gold particles strongly accumulate in tumor regions up to ~ 25 times more than in normal muscle tissue. This accumulation increases with the time after injection for up to 12 h. This result has important implications for enhancing radiation tumor therapy using gold nanoparticles.
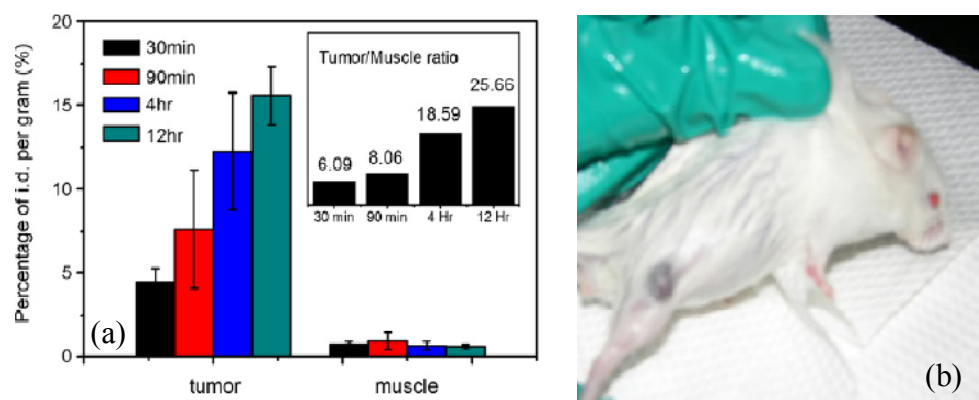
Figure 7.5 Biodistribution of PEG-Au nanoparticles in tumor bearing mice for different times after injection. The ratios of gold concentration in tumor and non-tumor regions as a function of time are shown in (a). The inset highlights the dramatic increase. The image (b) shows the strong accumulation of gold nanoparticles in tumor sites 24 h after the tail vein injection.

7.3   Binary and ternary alloy nanoparticles

Binary Au-Ag alloyed nanoparticles, due to their tunability in the composition and structure, demonstrate unique physical properties and play an increasingly important role in versatile application fields. Numerous methods have been developed for the synthesis of alloyed Au-Ag nanoparticles in aqueous solutions. The co-reduction of mixed metallic precursors in the presence of suitable stabilizers accounts for the most common chemical method. However, only very dilute (~ 5 μM) Au-Ag colloidals are obtained due to the unfavorable formation of halide (AgCl) precipitates in the precursors at a higher Ag^+ concentration. A one-pot, scalable approach for Au-Ag alloyed colloidals with higher concentration in aqueous solution would be desirable for the technical application of nanoparticles. An alternative approach to prepare metallic nanoparticles in aqueous solution employs irradiation to co-reduce the metal precursors. Up to date, Au-Ag nanoparticles have only been attempted using gamma-rays. In this work, intense X-rays delivered from synchrotron radiation facilities are utilized to prepare a series of binary Au-Ag colloidal with different compositions.

Au-Ag can be regarded as the chemical subunit of Heusler compounds with a general formula of Au-Ag-R_2 where R denotes a transition metal such as Zn or Cd. Heusler compounds compose a family of magnetic materials that are promising candidates for spintronics. In this work, efforts were made to prepare ternary alloyed nanoparticle with ternary components in the systems of Au-Ag-Cd and Au-Ag-Zn by introducing additional Cd- and Zn- containing salts into the precursor solutions.

TEM images together with the particle size distribution of Au-Ag alloy nanoparticles are shown in Figure 7.6. The size of Au-Ag particles (Au: Ag = 1:1) without PEG modification is about 16.2 ± 2.8 nm. After adding the poly ethylene glycol (PEG) molecules, the size of the PEG modified Au-Ag particles decrease to less than 5 nm with a narrow size

distribution. A lattice with cubic (111) orientation can be clearly identified from the inserted HRTEM image in Figure 7.6 (c). The inter-planar spacing is approximately 0.235 nm. Both TEM and HRTEM examinations indicate the formation of alloy nanoparticles. The elemental distribution in Au-Ag nanoparticles was probed by a line-scanning EDX analysis. As shown in Figure 7.6 (e), Au and Ag atoms were homogeneously distributed within the particles indicating that the formation of alloy nanoparticles.
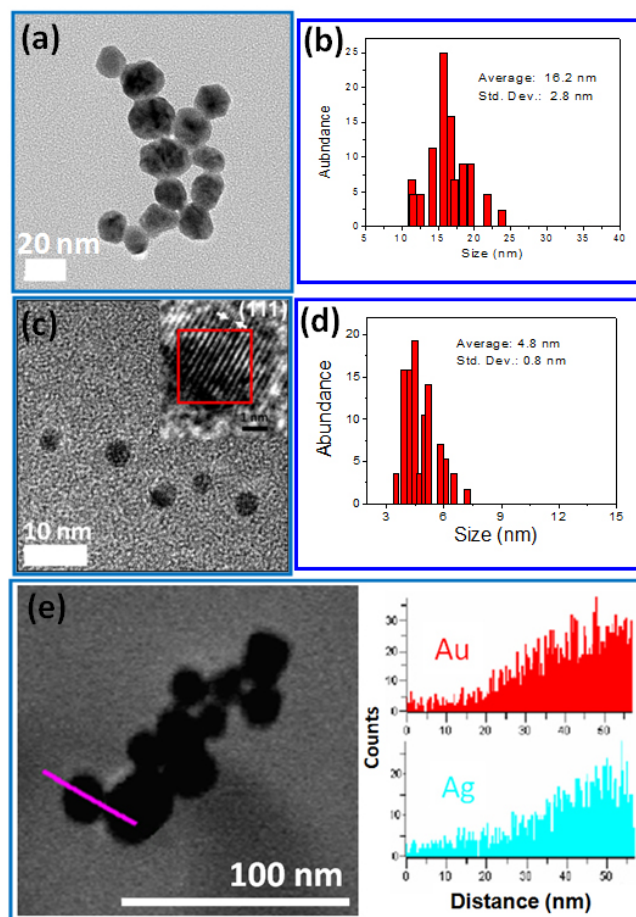
Figure 7.6 TEM micrographs and size distribution of Au-Ag alloy nanoparticles (a) to (b) and Au-Ag nanoparticles (c) to (d) with the elemental line profile of Au-Ag nanoparticles by EDX analysis (e).

Even thought the lattice parameters of Au and Ag are very close, the lattices of Au, Ag, and Au-Ag can be differentiated by performing synchrotron radiation based XRD measurements. This might be partly attributed to the high photon energy (22.5 keV) and to the ultrahigh photon flux. As shown in Figure 7.7, the lattice constants of the Au-Ag nanoparticles are calculated based on (111) and (311) diffraction peaks. The observed lattice parameter of the Au-Ag sample closely resembles (within the accuracy of the calculations) that of simulated $Au_{0.5}Ag_{0.5}$ indicating an inclusion of Ag into the Au lattice. From this method, the composition of the sample is evaluated by a linear interpolation between the lattice parameters of pure Au and Ag (the Vegard's law). The obtained composition is

consistent with the molar ratio of the feed precursors in the solutions indicating the preserved stoichiometry in the alloy nanoparticles.

As shown by the XRD spectra in Figure 7.7 (a), the diffraction patterns of Au-Ag-Cd and Au-Ag-Zn nanoparticles do not match with the corresponding Heusler phases but resemble well with that of the binary Au-Ag alloyed nanoparticles. This indicates that a ternary phase is not formed. When examining the lattice parameters of the Au-Ag-Cd$_2$ and Au-Ag-Zn$_2$ samples, it is observed that they are similar to phases of the pure Au and Ag. The phase compositions of the Au-Ag-Cd$_2$ and Au-Ag-Zn$_2$ samples are expected to be a mixture of Au+Au-Ag and Ag+Au-Ag, respectively. Compared to Au and Ag, which have positive standard reduction potential of similar values, both Cd and Zn have negative redox potentials. This discrepancy in the reactive potentials between Au(Ag) and Cd(Zn) might pose a challenge since the Cd and/or Zn atoms might not be incorporated into the Au-Ag unit cells.
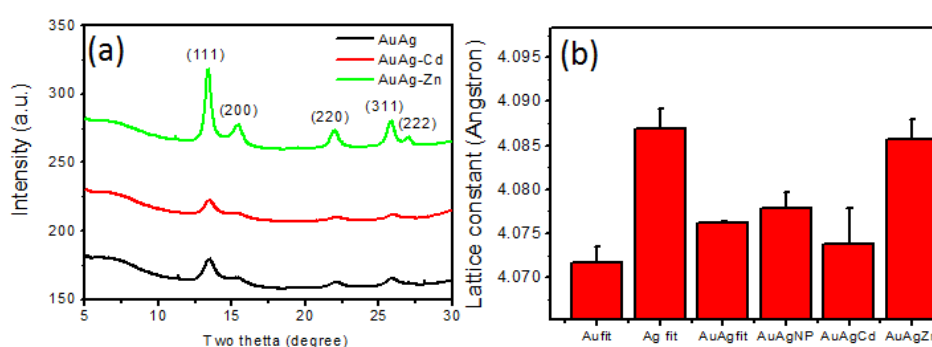
Figure 7.7 XRD spectra of PEG-AuAg, PEG-Au-Ag-Cd$_2$ and PEG-Au-Ag-Zn$_2$ and lattice constant comparison between simulated and measured values based on the (111) and (311) diffraction peaks.

The formation of Au-Ag nanoalloy is further verified by optical absorption spectra of the Au-Ag samples with different Au/Ag compositions. As shown in Figure 7.8, for metallic nanosols composed of single components such as Au or Ag, The SPR peaks are observed at around 410 nm for Ag or 520 nm for Au nanoparticles. For Au-Ag alloyed nanoparticles, however, only one absorption peak located between 410 nm and 520 nm was observed and the location of the peak depends on the alloy composition (Au molar fraction). This is a typical feature for the alloyed nanoparticles rather than either a core-shell-structure or a mixture of individual components. When plotting the peak position of the Au-Ag nanoalloy as function of the Au molar fractions, a quasi-linear pattern is observed and the SPR peak exhibits a red-shift with increasing Au incorporation. The linearly shifted profile could be traced back to the composition-induced variation of lattice parameters and therefore dielectric properties of the nanoparticles.
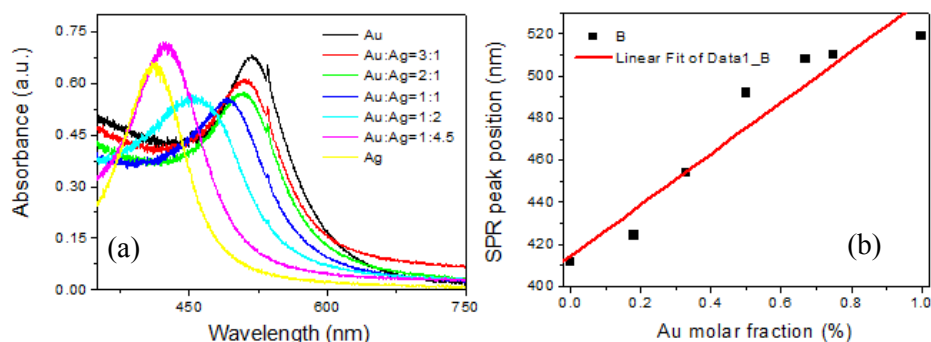
Figure 7.8 Optical absorption properties of colloidal Au, Ag, and Au-Ag alloy with different Au fractions: (a) spectra; (b) correlation of SPR peak position and alloy composition. The line in (b) is a linear fit to experimental data.

7.4   Summary

Synchrotron X-rays are utilized to prepare a variety of metallic colloidals in aqueous solutions. The advantages of this new chemical method include fast, easy to scale up, and that the obtained nanoparticles are biocompatible. The obtained metal nanoparticles show potentials in wide application fields including nanobiotechnology and nanomedicine. To fully exploit the advantages of the new radiation synthetic route, a fundamental knowledge of the initial states of the radiation reactions and the involved free radical chemistry is required. Due to the ultrahigh photon flux and dose rate of synchrotron X-rays, the underlined mechanisms of creating colloidal gold using X-rays could be significantly different from those derived for conventional radiochemistry processes. Further efforts are needed to explore the potential of this newly developed chemical approach for nanoparticles.

8 Summary and outlook

Studies on Heusler compounds have been intensively focused on bulk and thin film samples due to their technical importance. This work reports the experimental investigations on the chemical synthesis, structure, and magnetic properties of ternary Heusler nanoparticles. The fundamental aspects in physics, chemistry and materials science underlining Heusler nanoparticles are investigated, which could serve as a basis for future studies of structure-property correlations in Heusler nanoparticles. The important conclusions drawn from the present work are summarized herein. As a new multidiscipline research field, many scientifically and technically important issues on Heusler nanoparticles are to be explored. These perspectives are discussed in the outlook section.

8.1 Summary

In this work, carbon coated, silica supported ternary intermetallic Co_2FeGa nanoparticles with various compositions and particle sizes are prepared by a newly developed chemical method. The dependences of the phase and size of Co_2FeGa nanoparticles on the precursor composition and silica supports are investigated. From XRD analyses, Co_2FeGa phases are observed in Co_2FeGa nanoparticles under nonstoichiometric conditions. The appearance and the amount of impurity phases are closely associated with the richness of Co and Fe. The formation of the $L2_1$ ordered Co_2FeGa phase is also supported by analyzing the XAFS spectra at the K-edges of Fe, Co and Ga. The morphology and dimension of the silica materials are important to affect the particle size of the formed nanoparticles. The pores formed by the closely packed silica spheres are found to play an important role in determining the size of the formed Co_2FeGa nanoparticles.

Structure and size control are of critical importance in a chemical synthesis of Heusler nanoparticles. The size of Co_2FeGa nanoparticles can be tuned by adjusting the silica supports. The formation of $L2_1$ Co_2FeGa phase is confirmed by anomalous XRD, Mössbauer spectroscopy and magnetic measurements. EXAFS technique has been demonstrated to be a suitable method to identify the crystal structure of Co_2FeGa Heusler nanoparticles. It is found that the degree of both long and short range order of Co_2FeGa Heusler nanoparticles decrease for smaller Co_2FeGa nanoparticles. The coupling of TEM-derived particle size and Mössbauer spectroscopy specifies the critical size of Co_2FeGa nanoparticles bridging superparamagnetism and ferromagnetism.

The long and short range order structures, and magnetic properties of Fe-rich Co_2FeGa and Fe_2CoGa nanoparticles are investigated. For Fe-rich Co_2FeGa nanoparticles, the presence of $L2_1$ ordered Heusler phase are verified by XRD and EXAFS analyses. Specifically, the $L2_1$ ordered structure is supported by the short range order structure matching at the absorption K edges of Fe, Co, and Ga. Due to the similarities in backscattering amplitude and phase shift of Fe and Co, $L2_1$ and DO_3 structure in Co_2FeGa phase cannot be differentiated by EXAFS technique. EXAFS fits on the first shells of the X-sites on both samples reveal high degree of structure ordering by comparing the bond lengths in the first coordination shells. EXAFS fits indicate that the ordered structure of Fe_2CoGa nanoparticles could be better described by the X-type ordering. The presence of impurities in the nanoparticles makes it difficult to directly compare the measured magnetizations to the reported experimental values and theoretical predictions.

Strategies of size control on silica supported Co_2FeGa nanoparticles are examined. It is demonstrated that a two-step sequence centrifugation process is capable to separate the small nanoparticles from the large ones. The size separation efficiency would be enhanced if the as-prepared Co_2FeGa nanoparticles possess a favorable bimodal size distribution which is easy to separate. As an example, a coupling of using silica gel with a pore size of 6 nm and

shorter annealing time is optimal to obtain Co_2FeGa nanoparticles with well separated size ranges. The chemical synthesis approach for silica supported Co_2FeGa nanoparticles exhibits great potential as a general method for Heusler nanoparticles of a wider range of compositions. Excellent synthetic transferability is demonstrated for Fe_2CoGa, Co_2FeZ (Z = Al, Si, Ga), and Co_2MnGa nanoparticles. In comparison, synthetic approaches employing colloidal chemistry are also attempted but with few success. A summary of successful chemical synthesis of ternary Heusler nanoparticles is described in Figure 8.1.

Figure 8.1 Periodic table of the elements showing the Heusler nanoparticles that can be successfully by the silica-assisted method investigated in this work.

7.2   Outlook

Elemental site swapping has been proved a fundamental limitation to realize HMF in Heusler compounds and nanoparticles. In this work, a combination of AXRD, EXAFS, and ^{56}Fe Mössbauer spectroscopy are found valuable to distinguish between different structure types in Heusler Co_2FeZ nanoparticles. It would be more convincing if the results from different characterizations point to the same conclusion. It has been experimentally shown that atomic disorder in Heusler alloys can be examined by measuring low temperature resistivity. Therefore, low temperature electronic transport measurement should be carried out for Co_2FeGa Heusler nanoparticles as well. What's more, theoretical work appropriately targeting Co_2FeGa and Fe_2CoGa Heusler compounds are required to provide theoretical basis for further investigations.

For Heusler compounds designed for practical spintronics applications, at least several requirements have to be met:

(1)   An electronic structure favorable for stable HMF behavior (requiring the Fermi energy located in the middle of and away from the band edges of the minority states);

(2)   A high order-disorder phase transition temperature;

(3)   A measured integer magnetic moment as predicted by the generalized
      Salter-Pauling rule;

(4)   A high spin polarization in TMJs that can be verified by high resolution hard
      X-ray photoemmision spectroscopy;

(5)   A high Curie temperature.

Co_2FeGa is a type III half-metal. In comparison, Co_2MnZ (z = Si, Ga) and Co_2FeGe shows the properties of the Type I half-metals where Fermi energy is located inside of the gap of the minority band. As a direct consequence, the minority density at the Fermi energy vanishes and the spin polarization is 100%. Taken into account of the demonstrated synthetic transferability, the chemical synthesis, structural, electric and magnetic properties of Co_2MnGa and Co_2FeGe nanoparticles might be more attractive with respect to the technical applications.

Fe_2CoGa Heusler compounds might be attractive for ferromagnetic shape memory alloy (FSMA) applications. Fe_2CoGa Heusler nanoparticles have been prepared and characterized in this work. The martensitic transformation of Fe_2CoGa, however, has not been experimentally investigated. The MSMA effect stems from martensitic phase transition. The decreased length scale to nanometer regime increases structural disorder. Structural disorder thus introduced is expected to modify the martensite phase transition. It is assumed that a critical size exists at which the martensitic transformation is suppressed. Clearly further experimental and theoretical studies on both bulk and nano-sized Fe_2CoGa compounds are required to clarify the unresolved issues in this work.

The research on Heusler nanoparticles is just on the way. Some more challenging tasks are:

(1) To measure the electronic transport properties, TMR ratio, and spin polarization of Co_2FeGa and other Heusler nanoparticles;

(2) To correlate the antisite disorders in Heusler nanoparticles to their spin-related properties;

(3) To clarify whether and, if yes, why nonstoichiometric Heusler compounds as electrodes for TMJs exhibit better performance (higher TMR ratio etc.) than their stoichiometric counterparts in the cases of Heusler nanoparticles;

(4) Films, instead of supported or isolated nanopowders, are of more technical relevance. To prepare ternary Heusler nanostructured films, physical (sputtering, cluster machine, pulsed laser deposition etc.) and chemical (sol-gel spin coating, chemical vapor deposition etc.) methods are well-established techniques and may be used for preparing thin films composed of Heusler nanoparticles.

Bibliography

[1] F. Heusler, *Verh. Dtsch. Phys. Ges.* **5**, 219 (1903).

[2] J. Kübler, A. R. Williams, and C. B. Sommers, *Phys. Rev. B* **28**, 1745 (1983).

[3] R. A. de Groot, F. M. Müller, P. G. van Engen, and K. H. J. Buschow, *Phys. Rev. Lett.* **50**, 2024 (1983).

[4] C. Felser, G. H. Fecher, and B. Balke, *Angew. Chem. Int. Edn.* **46**, 668 (2007).

[5] M.N. Baibich, J.M. Broto, A. Fert, F. Nguyen van Dau, F. Petroff, P. Eitenne, G. Creuzet, A. Friederich, and J. Chazelas, *Phys. Rev. Lett.* **61**, 2472 (1988).

[6] G. Binasch, P. Grünberg, F. Saurenbach, and W. Zinn, *Phys. Rev. B* **39**, 4828 (1989).

[7] R. Kainuma, Y. Imano, W. Ito, Y. Sutou, H. Morito, S. Okamoto, O. Kitakami, K. Oikawa, A. Fujita, T. Kanomata, and K. Ishida, *Nature* **439**, 957 (2006).

[8] R. Kainuma, K. Oikawa, W. Ito, Y. Sutou, T. Kanomata, and K. Ishida, *J. Mater. Chem.* **18**, 1837 (2008).

[9] J. Barth, G. H. Fecher, B. Balke, T. Graf, C. Felser, A. Shkabko, and A. Weidenkaff, *Phys. Rev. B* **81**, 064404 (2010).

[10] S. Bhattacharya, A. L. Pope, R. T. Littleton IV, and T. M. Tritt, V. Ponnambalam, Y. Xia, and S. J. Poon, *Appl. Phys. Lett.* **77**, 2476 (2000).

[11] D. Kieven, R. Klenk, S. Naghavi, C. Felser, and T. Gruhn, *Phys. Rev. B* **81**, 075208 (2010).

[12] S. Chadov, X. L. Qi, J. Kübler, G. H. Fecher, C. Felser, and S. C. Zhang, *Nat. Mater.* **9**, 541 (2010).

[13] X. L. Qi, R. Li, J. Zang, and S. C. Zhang, *Science* **323**, 1184 (2009).

[14] H. Lin, L. A. Wray, Y. Q. Xia, S. Y. Xu, S. Jia, R. J. Cava, A. Bansil, and M. Z. Hasan, *Nat. Mater.* **9**, 546 (2010).

[15] Y. Sakuraba, M. Hattori, M. Oogane, Y. Ando, H. Kato, A. Sakuma, T. Miyazaki, and H. Kubota, *Appl. Phys. Lett.* **88**, 192508 (2006).

[16] T. Ishikawa, T. Marukame, H. Kijima, K-I. Matsuda, T. Uemura, and M. Yamamoto, *Appl. Phys. Lett.* **89**, 192505 (2006).

[17] N. Tezuka, N. Ikeda, S. Sugimoto, and K. Inomata, *Jpn. J. Appl. Phys.* **46**, L454 (2007).

[18] M. Yamamoto, T. Ishikawa, T. Taira, G. F. Li, K. I. Matsuda, and T. Uemura, *J. Phys.: Condens. Matter* **22**, 164212 (2010).

[19] I. Galanakis, and P. Mavropoulos, *J. Phys.: Condens. Matter* **19**, 315213 (2007).

[20] C. M. Fang, G. A. de Wijs, and R. A. de Groot, *J. Appl. Phys.* **91**, 8340 (2002).

[21] M. I. Katsnelson, V. Yu. Irkhin, L. Chioncel, A. I. Lichtenstein, and R. A. de Groot, *Rev. Mod. Phys.* **80**, 315 (2008).

[22] G. Bunker, *Nuclear Instrum. Methods* **207**, 437 (1983).

[23] J. C. Slater, *Phys. Rev.* **49**, 931 (1936).

[24] L. Pauling, *Phys. Rev.* **54**, 899 (1938).

[25] I. Galanakis, P. H. Dederichs, and N. Papanikolaou, *Phys.Rev. B* **66**, 174429 (2002).

[26] G. H. Fecher, H. C. Kandpal, S. Wurmehl, C. Felser, and G. Schönhense, *J. Appl. Lett.* **99***, 08J106 (2006).

[27] B. Ravel, J. O. Cross, M. P. Raphael, V. G. Harris, R. Ramesh, and V. Saraf, *Appl. Phys. Lett.* **81**, 2812 (2002).

[28] B. Ravel, M. P. Raphael, V. G. Harris, and Q. Huang, *Phys. Rev. B* **65**, 184431 (2002).

[29] B. Balke, S. Wurmehl, G. H. Fecher, C. Felser, M. C. M. Alves, F. Bernardi, and J. Morais, *Appl. Phys. Lett.* **90***, 172501 (2007).

[30] S. Wurmehl, G. H. Fecher, K. Kroth, F. Kronast, H. A. Dürr, Y. Takeda, Y. Saitoh, K. Kobayashi, H.-J. Lin, G. Schönhense, and C. Felser, *J. Phys. D: Appl. Phys.* **39**, 803 (2006).

[31] S. Wurmehl, M. C. M. Alves, J. Morais, V. Ksenofontov, S. R. Teixeira, G. Machado, G. H. Fecher, and C. Felser, *J. Phys. D: Appl. Phys.* **40**, 1524 (2007).

[32] S. Wurmehl, G. H. Fecher, H. C. Kandpal, V. Ksenofontov, C. Felser, H-J. Lin, J. Morais, *Phys. Rev. B* **72**, 184434 (2005).

[33] http://nobelprize.org/nobel_prizes/physics/laureates/2007/sci.html.

[34] A. T. Zayak, P. Entel, and J. R. Chelikowsky, *Phys. Rev. B* **77**, 212401 (2008).

[35] A. T. Zayak, S. P. Beckman, M. L. Tiago, P. Entel, and J. R. Chelikowsky, *J. Appl. Phys.* **104**, 074307 (2008).

[36] V. O. Golub, A. Ya. Vovk, L. Malkinski, C. J. O'Connor, Z. Wang, and J. Tang, *J. Appl. Phys.* **96***, 3865 (2004).

[37] A. Hirohata, S. Ladak, N. P. Aley, and G. B. Hix, *Appl. Phys. Lett.* **95**, 252506 (2009).

[38] Y. Jing, Y. H. Xu, and J. P. Wang, *J. Appl. Phys.* **105**, 07B520 (2009).

[39] N. Dahal, and V. Chikan, *Chem. Mater.* **22**, 2892 (2010).

[40] Y. D. Wang, Y. Ren, H. Z. Nie, D. M. Liu, L. Choo, H. Zuo, H. Li,   P. K. Liaw, J. Q.

Yan, R. J. Mcqueeney, J. W. Richardson, and A. Huq, *J. Appl. Phys.* **101***, 063530 (2007).

[41] V. Sebastian, N. Lakshmi, and K. Venugopalan, *Hyperfine Interact.* **183**, 61 (2008).

[42] B. Balke, S. Wurmehl, G. H. Fecher, C. Felser, and J. Kübler, *Sci. Technol. Adv. Mater.* **9**, 014102 (2008).

[43] S. Trudel, O. Gaier, J. Hamrle, and B. Hillebrands, *J. Phys. D: Appl. Phys.* **43**, 193001 (2010).

[44] Z. Gercsi, A. Rajanikanth, Y. K. Takahashi, K. Hono, M. Kikuchi, N. Tezuka, and K. Inomata, *Appl. Phys. Lett.* **89**, 082512 (2006).

[45] D. Ebke, J. Schmalhorst, N.-N. Liu, A. Thomas, G. Reiss, and A. Hütten, *Appl. Phys. Lett.* **89**, 162506 (2006).

[46] N.Tezuka, S. Okamura, A. Miyazaki, M. Kikuchi, and K. Inomata, *J. Appl. Phys.* **99***, 03T314 (2006).

[47] B. Balke, G. H. Fecher, H. C. Kandpal, and C. Felser, *Phys. Rev. B* **74**, 104405 (2006).

[48] N. Tezuka, N. Ikeda, A. Miyazaki, S. Sugimoto, M. Kikuchi, and K. Inomata, *Appl. Phys. Lett.* **89**, 112514 (2006).

[49] W. S. Jung, *Bull. Korean Chem. Soc.* **25**, 51 (2004).

[50] W. Stöber, A. Fink, and E. Bohn, *J. Colloid Interface Sci.* **26**, 62 (1968).

[51] M. Newville, P. Livins, Y. Yacoby, J. J. Rehr, and E. A. Stern, *Phys. Rev. B* **47**, 14126 (1993).

[52] B. Ravel, *J. Synchrotron Radiat.* **8**, 314 (2001).

[53] S. I. Zabinsky, J. J. Rehr, A. Ankudinov, R. C. Albers, and M. J. Eller, *Phys. Rev. B* **52**, 2995 (1995).

[54] M. Newville, *J. Synchrotron Radiat.* **8**, 322 (2001).

[55] M. Newville, B. Ravel, B. D. Haskel, J. J. Rehr, E. A. Stern, and Y. Yacoby, *Physica B* **208***, 154 (1995).

[56] H.-Y. Lee, T.-B. Wu, and J.-F. Lee, *J. Appl. Phys.* **80**, 2176 (1996).

[57] http://www.xradia.com.

[58] Y.-T. Chen, T.-N. Lo, Y. S. Chu, J. Yi, C.-J. Liu, J.-Y. Wang, C.-L. Wang, C.-W. Chiu, T.-E. Hua, Y. Hwu, Q. Shen, G.-C. Yin, K. S. Liang, H.-M. Lin, J. H. Je, and G. Margaritondo, *Nanotechnology* **19**, 395302 (2008).

[59] T.-N. Lo, Y.-T. Chen, C.-W. Chiu, C.-J. Liu, S.-R. Wu, I.-K. Lin, C.-I Su, W.-D. Chang, Y. Hwu, B.-Y. Shew, C.-C. Chiang, J. H. Je, and G. Margaritondo, *J. Phys. D: Appl.*

Phys. **40**, 3172 (2007).

[60] K. Lagarec and D. G. Rancourt, *Nucl. Instrum. Meth. Phys. Res. B* **129**, 266 (1997).

[61] R. Ducher, R. Kainuma, I. Ohnuma, and K. Ishida, *J. Alloy. Compd.* **437**, 93 (2007).

[62] R. Y. Umetsu, K. Kobayashi, A. Fujita, K. Oikawa, R. Kainuma, and K. Ishida, N. Endo, K. Fukamichi, and A. Sakuma, *Phys. Rev. B* **72**, 214412 (2005).

[63] A. Okubo, R. Y. Umetsu, M. Nagasako, A. Fujita, R. Kainuma, and K. Ishida, *Scripta Materialia* **59**, 830 (2008).

[64] K. H. J. Buschow, P. G. Van Engen, and R. Jongebreur, *J. Magn. Magn. Mater.* **38**, 11 (1983).

[65] J. M. D. Coey, and S. Sanvito, *J. Phys. D: Appl. Phys.* **37**, 988 (2004).

[66] M. Zhang, E. Brück, F. R de Boer, Z. Z. Li, and G. H. Wu, *J. Phys. D: Appl. Phys.* **37**, 2049 (2004).

[67] K. V. Peruman, M. Mahendran, S. Seenithurai, R. Chokkalingam, R. K. Singh, and V. Chandrasekaran, *J. Phys. Chem. Solid* **71**, 1540 (2010).

[68] K. Seo, N. Bagkar, S.-I. Kim, J. H. In, H. Yoon, Y. H. Jo, and B. S. Kim, *Nano Lett.* **10**, 3643 (2010).

[69] K. Özdogan, I. Galanakis, E. Sasıoglu, and B. Aktas, *Solid. State. Commun.* **142**, 492 (2007).

[70] W. S. Seo, J. H. Lee, X. M. Sun, Y. Suzuki, D. Mann, Z. Liu, M. Terashima, P. C. Yang, M. V. McConnell, D. G. Nishimura, and H. J. Dai, *Nat. Mater.* **5**, 971 (2006).

[71] W. S. Seo, S. M. Kim, Y. M. Kim, X. M. Sun, and H. J. Dai, *Small* **4**, 1968 (2008).

[72] L. Basit, C. H. Wang, C. A. Jenkins, B. Balke, V. Ksenofontov, G. H. Fecher, C. Felser, E. Mugnaioli, U. Kolb, S. A. Nepijko, G. Schönhense, and M. Klimenkov, *J. Phys. D: Appl. Phys.* **42**, 084018 (2009).

[73] C. H. Wang, Y. Z. Guo, F. Casper, B. Balke, G. H. Fecher, C. Felser, and Y. Hwu, *Appl. Phys. Lett.* **97**, 103106 (2010).

[74] C. H. Wang, L. Basit, Y. Khalavka, Y. Z. Guo, F. Casper, T. Gasi, V. Ksenofontov, B. Balke, G. H. Fecher, C. Sönnichsen, Y. Hwu, J. J. Lee, and C. Felser, *Chem. Mater.* **22**, 6575 (2010).

[75] T. Block, C. Felser, G. Jakob, J. Ensling, B. Muhling, P. Gutlich, V. Beaumont, F. Studer, and R. J. Cava, *J. Solid State Chem.* **176**, 646 (2003).

[76] H. J. Elmers, G. H. Fecher, D. Valdaitsev, S. A. Nepijko, A. Gloskovskii, G. Jakob, G. Schöenhense, S. Wurmehl, T. Block, C. Felser, P. C. Hsu, W. L. Tsai, and S. Cramm, *Phys. Rev. B* **67**, 104412 (2003).

[77] X. Y. Liu, A. Q. Wang, X. F. Yang, T. Zhang, C. Y. Mou, D. S. Su, and J. Li, *Chem. Mater*. **21**, 410 (2009).

[78] T. Graf, F. Casper, J. Winterlik, B. Balke, G. H. Fecher, and C. Felser, *Z. Anorg. Allg. Chem.* **635**, 976 (2009).

[79] D. Kodama, K. Shinoda, K. Sato, Y. Konno, R. J. Joseyphus, K. Motomiya, H. Takahashi, T. Matsumoto, Y. Sato, K. Tohji, and B. Jeyadevan, *Adv. Mater.* **18**, 3154 (2006).

[80] N. K. Jaggi, K. R. P. M. Rao, A. K. Grover, L. C. Gupta, R. Vijayaraghavan, and L. K. Dang, *Hyperfine Interact.* **4**, 402 (1978).

[81] Y. S. Chu, J. M. Yi, F. De Carlo, Q. Shen, W. K. Lee, H. J. Wu, C. L. Wang, J. Y. Wang, C. J. Liu, C. H. Wang, S. R. Wu, C. C. Chien, Y. Hwu, A. Tkachuk, W. Yun, M. Feser, K. S. Liang, C. S. Yang, J. H. Je, and G. Margaritondo, *Appl. Phys. Lett.* **92**, 103119 (2008).

[82] W. L. Tsai, P. C. Hsu, Y. Hwu, C. H. Chen, L. W. Chang, J. H. Je, H. M. Lin, A. Groso, and G. Margaritondo, *Nature* **417**, 139 (2002).

[83] B. R. Elliott, J. J. Host, V. P. Dravid, M. H. Teng, and J. H. Hwang, *J. Mater. Res.* **12**, 3328 (1997).

[84] F. Matthias and A. Marc, *Chem. Mater.* **21**, 5886 (2009).

[85] W. Jiang, B. Y. S. Kim, J. T. Rutka, and W. C. W. Chan, *Nat. Nanotech.* **3**, 145 (2008).

[86] C. T. Campbell, S. C. Parker, and D. E. Starr, *Science* **298**, 811 (2002).

[87] C. B. Rong, D. Li, V. Nandwana, Y. Poudyal, Y. Ding, Z. Lin, Z. L. Wang, , H. Zeng, and J. P. Liu, *Adv. Mater.* **18**, 2984 (2006).

[88] P. H. Gamlen and J. W. White, *J. Chem. Soc. Farad. T. 2.* **72**, 446 (1976).

[89] Y. Khalavka, C. Ohm, L. Sun, F. Banhart, and C. Sönnichsen, *J. Phys. Chem. C* **111**, 12886 (2007).

[90] Y.-G. Baek, S.-I. Honda, T. Ikuno, S. Ohkura, M. Katayama, T. Hirao, and K. Oura, *Japan. J. Appl. Phys.* **42**, 579 (2003).

[91] I. Galanakis, K. Özdogan, B. Aktas, and E. Sasıoglu, *Appl. Phys. Lett.* **89**, 042502 (2006).

[92] S. Picozzi, A. Continenza, and A. J. Freeman, *Phys. Rev. B* **69**, 094423 (2004).

[93] Z. X. Tang, C. M. Sorensen, K. J. Klabunde, and G. C. Hadjipanayis, *Phys. Rev. Lett.* **67**, 3602 (1991).

[94] D. H. Han, J. P. Wang, and H. L. Luo, *J. Magn. Magn. Mater.* **136**, 176 (1994).

[95] G. F. Goya, T. S. Berquo, F. C. Fonseca, and M. P. Morales, *J. Appl. Phys.* **94**, 3520

(2003).

[96] M. Hashimoto, J. Herfort, A. Trampert, and K. H. Ploog *J. Crystal. Growth* **301-302**, 592 (2007).

[97] M. Hashimoto, J. Herfort, H.-P. Schönherr, and K. H. Ploog, *Appl. Phys. Lett.* **87**, 102506 *(*2005).

[98] M. Weissmann, G. Garcia, M. Kiwi, and R. Ramirez, *Phys. Rev. B* **70**, 201401 (2004).

[99] K. H. Ang, I. Alexandrou, N. D. Mathur, G. A. J. Amaratunga, and S. Haq, *Nanotechnology* **15**, 520 (2004).

[100] A. Planes, L. Manosa, and M. Acet, *J. Phys. Condens. Matter* **21**, 233201 (2009).

[101] A. Ayuela, J. Enkovaara, K. Ullakko, and R. M. Nieminen J. *Phys.: Condens. Matter* **11**, 2017 (1999).

[102] S. E. Kulkova, S. V. Eremmev, and S. S. Kulkov, *Solid. State. Commun.* **130**, 793 (2004).

[103] A. Dannenberg, M. E. Gruner, M. Wuttig, and P. Entel, *ESOMAT 2009*, 04004 (2009).

[104] T. J. Burch, and T. Litrenta, *Phys. Rev. Lett.* **33**, 421 (1974).

[105] M. Gilleβen and R. Dronskowski, *J. Comput. Chem.* **31**, 612 (2010).

[106] Dannenberg, M. Siewert, M. E. Gruner, M. Wuttig, and P. Entel, *Phys. Rev. B* **82**, 214421 (2010).

[107] G. D. Liu, X. F. Dai, S. Y. Yu, Z. Y. Zhu, J. L. Chen, G. H. Wu, H. Zhu, and J. Q. Xiao, *Phys. Rev. B* **74**, 054435 (2006).

[108] G. E. Bacon and J. S. Plant, *J. Phys. F: Metal Phys.* **1**, 524 (1971).

[109] P. J. Brown, T. Kanomata, K. Neumann, K. U. Neumann, B. Ouladdiaf, A. Sheikh, and K. R. A. Ziebeck, *J. Phys.: Condens. Matter* **22**, 506001 (2010).

[110] X. M. Sun, S. M. Tabakman, W.-S. Seo, L. Zhang, G. Y. Zhang, S. Sherlock, L. Bai, and H. J. Dai, *Angew. Chem. Int. Ed.* **48**, 939 (2009).

[111] C. T. Yavuz, J. T. Mayo, W. W. Yu, A. Prakash, J. C. Falkner, S. J. Yean, L. L. Cong, H. J. Shipley, A. Kan, M. Tomson, D. Natelson, and V. L. Colvin, *Science* **314**, 964 (2006).

[112] R. N. Grass, E. K. Athanassiou, and W. J. Stark, *Angew. Chem. Int. Ed.* **46**, 4909 (2007).

[113] X. Sun, S. Zaric, D. Daranciang, K. Welsher, Y. Lu, X. Li, and H. Dai, *J. Am. Chem. Soc.* **130**, 6551 (2008).

[114] K. Page, C. S. Schade, J. P. Zhang, P. J. Chupas, K. W. Chapman, T. Proffen, A. K.

Cheetham, and R. Seshadri, *Materials Research Bulletin* **42**, 1969 (2007).

[115] W. U. Huynh, J. J. Dittmer, and A. P. Alivisatons, *Science* **295**, 2425 (2002).

[116] I. Gur, N. A. Fromer, C. P. Chen, A. G. Kanaras, and A. P. Alivisatons, *Nano Lett.* **7**, 409 (2007).

[117] P. W. Cyr, E. J. D. Klem, L. Levina, and E. H. Sargent, Nat. Mater. **4**, 138 (2005).

[118] H. Z. Zhong, Y. Zhou, M. F. Ye, Y. J. He, J. P. Ye, C. He, C. H. Yang, and Y. F. Li, *Chem. Mater.* **20**, 6434 (2008).

[119] S. L. Castro, S. G. Bailey, K. K. Banger, and A. F. Hepp, *Chem. Mater.* **15**, 3142 (2003).

[120] J. J. Nairn, P. J. Schapiro, B, Twamley, T. Pounds, R. V. Wandruszka, M. Williams, C. M. Wang, and M. G. Notton, *Nano Lett.* **6**, 1218 (2006).

[121] C. H. Wang, C.-C. Chien, Y.-L. Yu, C.-J. Liu, C.-F. Lee, C.-H. Chen, Y. Hwu, C.-S. Yang, J.-H. Je, and G. Margaritondo, *J. Synchrotron Radiation* **14**, 477 (2007).

[122] C.-H. Wang, C.-J. Liu, C.-L. Wang, T.-E. Hua, J. M. Obliosca, K. H. Lee, Y. Hwu, C.-S. Yang, R.-S. Liu, H.-M. Liu, J.-H. Je, and G. Margaritondo, *J. Phys. D.: Appl. Phys.* **41**, 195301 (2008).

[123] C. H. Wang, C.-J. Liu, C.-L. Wang, C.-C. Chien, Y. Hwu, R.-S. Liu, C.-S. Yang, J.-H. Je, H. −M. Lin, and G. Margaritondo, *Appl. Phys. A.* **97**, 295 (2009).

[124] C. H. Wang, T.-E. Hua, C.-C. Chien, Y.-L. Yu, T.-Y. Yang, C.-J. Liu, W.-H. Leng, Y. Hwu, Y.-C. Yang, C.-C. Kim, J. H. Je, C.-H. Chen, H.-M. Lin, and G. Margaritondo, *Mater. Chem. Phys.* **106**, 323 (2007).

[125] C. H. Wang, C.-J. Liu, C.-C. Chien, H.-T. Chen, T.-E. Hua, W.-H. Leng, H.-H. Chen, I. M. Kempson, Y. Hwu, M. Hsiao, T.-C. Lai, J.-L. Wang, C.-S. Yang, H.-M. Lin, Y.-J. Chen, and G. Margaritondo, *Mater. Chem. Phys.* **126**, 352 (2011).

List of Figures

92

List of Tables